Posted on 30 Nov 2022 — The copyright holder is the author/funder. All rights reserved. No reuse without permission. — https://doi.org/10.1002/essoar.10511204/v3 — This a preprint and has not been peer reviewed. Data may be preliminary.

Seismic and tsunamigenic characteristics of a sequence of rapid and slow ruptures: The example of the 2021-08-12 South Sandwich earthquake sequence

Malte Metz[1,1,1], Felipe Vera[2,2,2], Angela Carillo-Ponce[3], Simone Cesca[4,4,4], Andrey Babeyko[5,5,5], Torsten Dahm[4,4,4], Joachim Saul[4,4,4], Frederik Tilmann[6,6,6], and Angela Carrillo-Ponce[3,3]

[1]University of Potsdam
[2]German Research Centre for Geosciences GFZ
[3]GFZ German Research Centre for Geosciences Potsdam
[4]GFZ German Research Centre for Geosciences
[5]Helmholtz-Zentrum Potsdam Deutsches GeoForschungsZentrum GFZ, Heinrich-Mann-Allee 18/19, 14473 Potsdam
[6]Deutsches GeoForschungsZentrum GFZ

November 30, 2022

Abstract

On August 12, 2021 an earthquake sequence of several $M_w > 7.3$ earthquakes hit the central and southern South Sandwich trench. Due to its remote location and short interevent times, reported earthquake parameters varied significantly between different international agencies. We studied the complex rupture by combining different seismic source characterization techniques sensitive to different frequency ranges based on teleseismic broadband recordings from 0.001–2 Hz, including point and finite fault inversions and the back-projection of high-frequency signals. We also determined moment tensor solutions for 88 aftershocks. The rupture sequence initiated with an M_w 7.6 thrust earthquake in the deep part of the seismogenic zone in the central subduction interface. Simultaneously a second shallow megathrust rupture was initiated, which propagated unilaterally to the south with a very slow rupture velocity of 1.2 km/s and varying strike following the curvature of the trench. The slow rupture covered nearly two thirds of the entire subduction, and with a M_w 8.2 released the bulk of the total moment of the sequence. Tsunami modelling indicates the inferred shallow rupture can explain the tsunami records. The southern segment of the shallow rupture overlaps with another activation of the deeper part of the megathrust equivalent to a M_w 7.6. The aftershock distribution confirms the extent and curvature of the rupture. Some mechanisms are consistent with the mainshocks, but many indicate also activation of secondary faults. Rupture velocities and radiated frequencies varied strongly between different stages of the rupture, which might explain the variability of published source parameters.

Seismic and tsunamigenic characteristics of a multimodal rupture of rapid and slow stages: The example of the complex 2021-08-12 South Sandwich earthquake

M. Metz[1,2], F. Vera[1,3], A. CarrilloPonce[1,2], S. Cesca[1], A. Babeyko[1], T. Dahm[1,2], J. Saul[1], F. Tilmann[1,3]

[1]GFZ German Research Centre for Geosciences, Potsdam, Germany
[2]Institute of Geosciences, University of Potsdam, Potsdam, Germany
[3]Institute of Geological Sciences, Freie Universität Berlin, Berlin, Germany

Key Points:

- A combination of multiple approaches, inversion setups and frequency ranges deciphered the complex earthquake of 2021 South Sandwich.
- The rupture consisted of 4 subevents with the largest occurring as a shallow slow rupture parallel to the South Sandwich trench.
- Forward modelling proves that the large, shallow thrust subevent caused the recorded tsunami.

Corresponding author: Malte Metz, `mmetz@uni-potsdam.de`

Abstract

On August 12, 2021 a > 220 s lasting complex earthquake with $M_w > 8.2$ hit the central and southern South Sandwich trench. Due to its remote location and short interevent times, reported earthquake parameters varied significantly between different international agencies. We studied the complex rupture by combining different seismic source characterization techniques sensitive to different frequency ranges based on teleseismic broadband recordings from 0.001–2 Hz, including point and finite fault inversions and the back-projection of high-frequency signals. We also determined moment tensor solutions for 88 aftershocks. The rupture initiated simultaneously with a M_w 7.6 thrust earthquake in the deep part of the seismogenic zone in the central subduction interface and a shallow megathrust rupture, which propagated unilaterally to the south with a very slow rupture velocity of 1.2 km/s and varying strike following the curvature of the trench. The slow rupture covered nearly two thirds of the entire subduction zone length, and with M_w 8.2 released the bulk of the total moment of the whole earthquake. Tsunami modelling indicates the inferred shallow rupture can explain the tsunami records. The southern segment of the shallow rupture overlaps with another activation of the deeper part of the megathrust equivalent to a M_w 7.6. The aftershock distribution confirms the extent and curvature of the rupture. Some mechanisms are consistent with the mainshocks, but many indicate also activation of secondary faults. Rupture velocities and radiated frequencies varied strongly between different stages of the rupture, which might explain the variability of published source parameters.

Plain Language Summary

The earthquake of August 12, 2021 along the deep-sea trench of the South Sandwich Islands in the South Atlantic reached a magnitude of 8.2 and triggered a tsunami. The automatic earthquake parameter determination of different agencies showed very different results shortly after the earthquake and partially underestimated the tsunami potential of the earthquake. A possible reason was the complex rupture process and that the tsunami was generated by a long and shallow slow slip rupture sandwiched between more conven-

tional fast slip subevents at its northern and southern ends. In addition, the fault surface, which extended over 450 km, was highly curved striking 150–220°. We investigated the different components of the seismic wavefields in different frequency ranges and with different methods. The analysis shows how even complex earthquakes can be deciphered by combining analysing methods. The comparison with aftershocks and the triggered tsunami waves confirms our model that explains the South Sandwich rupture by 4 subevents in the plate boundary along the curved deep-sea trench. Here, the depth, rupture velocities and slip on each segment of the rupture vary considerably. The method can also be applied to other megathrust earthquakes and help to further improve tsunami warnings in the future.

Introduction

The Sandwich plate (SW) is located in the Scotia Sea in the southern Atlantic at the junction of the Antarctic (AN), Scotia (SC) and South America (SA) plates (Fig. 1). It is confined by the East Scotia spreading ridge (ESR) to the west, strike slip segments to the north and the south, and the westward subduction of the SA plate with a rate of 62 - 72 mm/yr at the South Sandwich Trench (SST) to the east (e.g. Larter et al., 2003; Beniest & Schellart, 2020; Thomas et al., 2003).

Effects of mantle inflow, the adjacent strike slip systems and the slab bending result in a complex stress field, which causes a change in dominant focal mechanisms from trench-perpendicular compressive in the central segment of the SST to oblique strike-slip and reverse mechanisms with variable strikes within 100-200 km of the northern and southern edges of the SST (e.g. Giner-Robles et al., 2009; Leat et al., 2004; Abe, 1972, 1981, 1982; Forsyth, 1975; Purcaru & Berckhemer, 1982).

Only few large earthquakes with $M_w \geq 7.5$ have been reported for the region before 1975: the shallow extensional M_w 8.1 1929 event close to the northern tip of the SST, the large shallow M_w 7.4–7.5 1933 earthquake of unknown mechanism type and the deep extensional M_w7.8 1964 earthquake in the subducted slab (e.g. Abe, 1972, 1981; Forsyth, 1975; Wilson, 1940; Okal & Hartnady, 2009; Bondár et al., 2015). In addition to these, Global CMT (further GCMT) reports an M_W 7.5 thrust event at the northern edge of the SST in 2016 (Fig. 1).

After over 90 years since the last great South Sandwich earthquake with $M_W \geq 8$ a complex earthquake hit the eastern margin of the Sandwich plate on August 12, 2021 (Fig. 1) with short interevent times between reported subevents. The seismic records were complex and indicate a complex rupture process. For instance, the teleseismic body and Rayleigh waves at the broadband station BFO have a very different appearance at high and low frequencies in comparison to an aftershock with similar mechanism and location (Fig. 2). Strong low frequency waves appear much more extended and with different patterns, suggesting that different subevents possibly ruptured after the first earthquake generating more complex coda waves, causing major difficulties in the semi-automatic earthquake analysis (Hubbard, 2021). This may explain the unusual variety of focal mechanism solutions and magnitude estimates between different agencies as USGS, GEOFON and GCMT (Tab. 1). GCMT first reported the doublet as two separate earthquakes with M_w 8.3 and 7.9 for the first and second event, respectively (see e.g., Jia et al. (2022) for the originally distributed GCMT estimates), but later switched to a single long duration (300 s) earthquake with M_w 8.3. The solutions of USGS and GEOFON assume an earthquake doublet with magnitudes of M_w 7.5–7.7 for the first and M_w 8.0–8.2 for the second subevent. Global catalog depths range from very shallow (i.e., ≤20 km for GEOFON and GCMT) to depths of 35-50 km (USGS CMT). Proposed focal mechanisms agree on a thrust mechanism with one very shallow dipping plane (average dip 17°), as expected for plate interface events. The strike direction varies significantly both between the two subevents and for the same subevent between different agencies though. The earthquake caused a tsunami with amplitudes ranging from 10 to 64 cm, e.g. recorded at tide gauges at King Edward Point on South Georgia Island, Stanley on the Falkland Islands and Antarctica Base Prat on the South Shetland Islands (Flanders Marine Institute (VLIZ), Intergovernmental Oceanographic Commission (IOC), 2021). Due to the absence of any tsunami early warning system for the Atlantic coasts of Africa and

South America, no tsunami information was released for these regions, and an information statement was issued only for the Caribbean and North American shore lines by PTWC (`https://tsunami.gov/events/PHEB/2021/08/12/21224001/2/WECA43/WECA43.txt`, last visited 2022/03/29).

A multiple event inversion combining centroid moment tensors and a simplified extended rupture model applied to the complex rupture (Jia et al., 2022) yielded a total of 5 subevents, where the dominant subevent indicated very shallow and very slow southward rupture propagation with a rupture velocity of $\approx$1 km/s. Their results thus indicate a typical tsunami earthquake behaviour (as explained by Bilek & Lay, 2018) with a tsunamigenic slow rupturing event in the shallow conditionally stable domain of a subduction megathrust.

The August 12, 2021 rupture represents the largest moment release along the SST in the instrumental period. The simultaneous occurrence of fast and slow rupture modes as stated by Jia et al. (2022) is rarely observed so clearly, but led to an increased complexity of the rupture process of the earthquake. This complexity makes it challenging to reconstruct the rupture processes and estimate its tsunamigenic potential from standard seismological analysis approaches, even more so as no near field GNSS observations are available.

With this study we aim to resolve the static properties and kinematic processes of both the fast and slow ruptures from seismic source inversion and back-projection. We use Bayesian inversion techniques for both moment tensors and extended seismic source inversion. That allows to quantify also the uncertainties of our solutions for both derived rupture mechanisms but also the location. Furthermore we explore the implications of the rupture model for tsunami excitation by forward modelling and comparing to the observed tide gauge records from several island stations and the coast of South America. The rupture characterization is complemented by an analysis of the locations and mechanisms of the largest aftershocks.

In the following we will refer to the different stages of the complex rupture as subevents of the earthquake.

Table 1. Selected standard centroid moment tensor and W-phase inversion results published from different agencies for August 12, 2021 South Sandwich earthquakes. Origin times reported by USGS are 18:32:52 and 18:35:17 for the first and second event, respectively. GEOFON does not report centroid times or locations, and origin times and location are reported in the table.

Agency	Method	Periods	Time	Lat, Lon	Depth	M_w	Dip	Duration
Single event								
GCMT	C+W	450–50 s	18:35:25	-59.48°, -24.34°	20 km	8.29	14°	300 s
Event 1								
GEOFON	E	600–40 s	18:32:50	-57.64°, -25.33°	13 km	7.70	11°	-
USGS	W	500–150 s	18:33:31	-57.70°, -25.19°	51 km	7.50	26°	29 s
Event 2								
GEOFON	E+W	600–40 s	18:35:22	-58.42°, -25.21°	11 km	7.98	12°	-
USGS	W	1000–200 s	18:36:56	-60.81°, -23.16°	36 km	8.13	11°	133 s

Inversion methods:

E - epicentral moment tensor inversion (body- and surface waves)

W - W-phase moment tensor inversion

C+W - joint body, surface and W-phase centroid moment tensor inversion

E+W - joint body, surface and W-phase moment tensor inversion at the epicentre

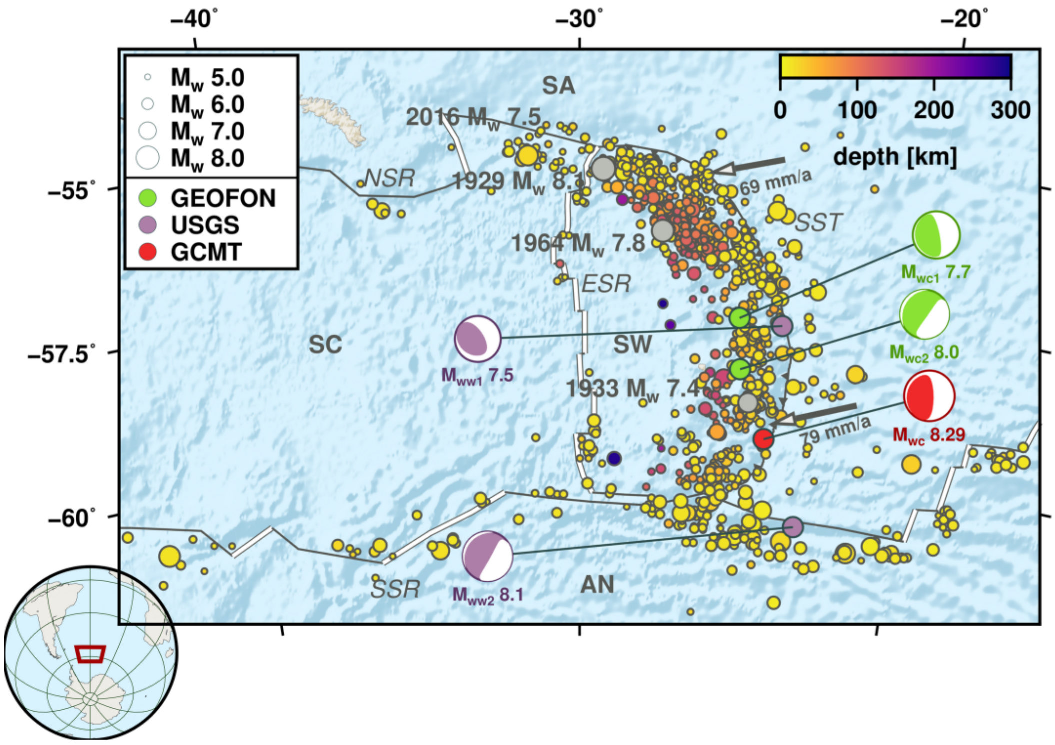

Figure 1. Seismicity and moment tensor solutions of the August 12, 2021 earthquakes are plotted together with bathymetry and outlines of the Sandwich plate (SW) in between the Scotia (SC), South America (SA) and Antarctic (AN) plates. Plate boundary labels indicate: NSR - North Scotia Ridge, SSR - South Scotia Ridge, SST - South Sandwich Trench, ESR - East Scotia Spreading Ridge (from Bird (2003); except that the SST was manually adjusted according to the location of the deformation front in bathymetry (minimum in EW profiles) between 58–60.6°S as its location is rather uncertain according to Thomas et al. (2003), and the SST in Bird's plate model did not match bathymetry). Pre-event seismicity is plotted by circles (1013 earthquakes, $M_w > 5.0$, 1976 - August 11, 2021, from GCMT; depth color-coded). Deviatoric moment tensor solutions from different agencies for two main shocks of the August 12 sequence are plotted in lower hemispherical projections (see legend for color coding and Tab. 1). Labels M_{wc} indicate Centroid moment tensors, M_{ww} the W-phase moment tensor, and numbers 1 and 2 the first or second event, respectively. Note, that the final GCMT solution is only a single long period moment tensor solution representing the whole rupture.

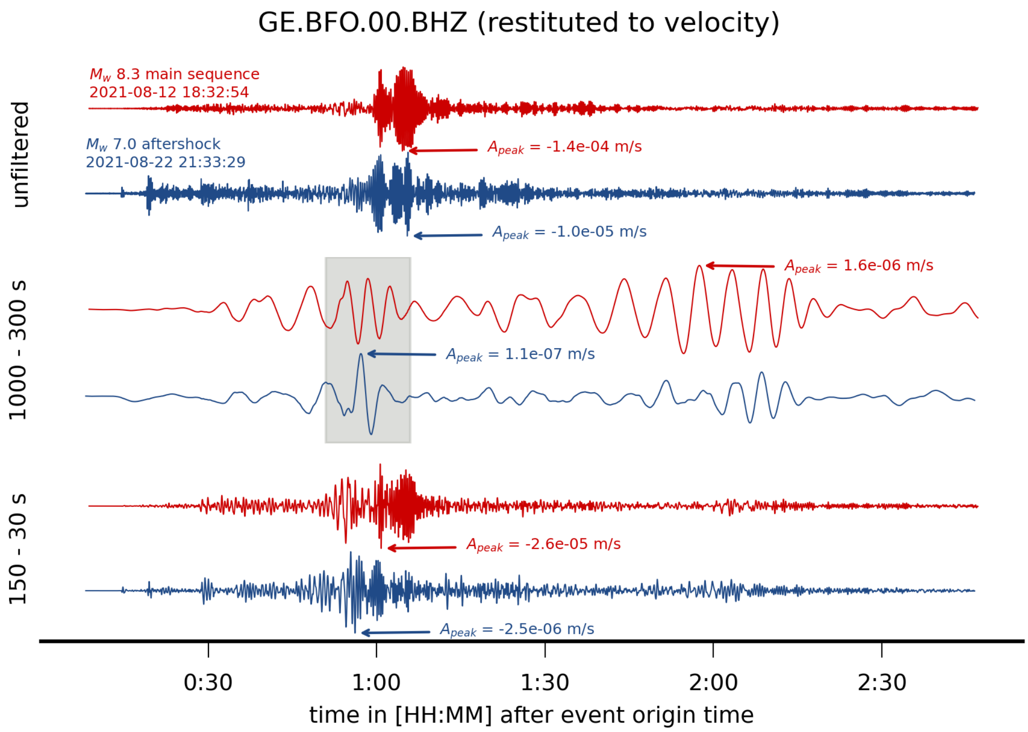

Figure 2. Comparison of vertical broad band waveforms of the main shock sequence (red) and an aftershock (blue) recorded at station GE.BFO.00 in 12,150 or 12,420 km epicentral distance from the main and the aftershock origin respectively. Velocity traces were restituted (top) and additionally filtered in very low (middle) and intermediate frequency range (bottom). Time is given relative to the epicentral time of the earthquakes given in the top left. The grey box highlights the Rg surface wave phase. Each trace is normalized to its maximum absolute amplitude (value and time indicated by A_{peak} for each trace).

Moment tensor inversions of the main shocks and the aftershocks

Individual centroid moment tensor (MT) inversions have been performed using the Grond software (Heimann et al., 2018) for the two main shocks (as indicated by GEOFON) and 88 aftershocks recorded until end of August 2021. In this appproach, the moment tensor components (full for the main shocks and deviatoric for the aftershocks), the centroid location, time and duration are estimated from waveform records, mostly Rayleigh and Love waves, assuming a simple half sinusoidal source time function. The inversion uses a particle swarm method paired with bootstrapping to estimate non-linear uncertainties for all parameters. Each inversion fitted displacement waveforms in the time domain. All observed waveforms were visually inspected and noisy, saturated, clipped or incomplete traces were removed. Filter and taper applied within the inversion used cosine tapers in frequency and time domain. Frequency ranges given in the following confine the flat part of the cosine taper. Further information on the tapers is given in Appendix A and Tabs. Appendix A.1 and Appendix C.1.

For estimation of the MT source parameters for the two main shocks as referenced by GEOFON (referred to as CMT inversions of subevents A and D), bandpass-filtered (0.01–0.03 Hz) teleseismic records (2500 - 10000 km epicentral distance) at 64 stations with good coverage in azimuth and distance were fitted on the vertical and transverse component.

In addition, we carried out a very low frequency inversion of the W-phase signals (referred to as CMT inverson of subevent B) from 0.001–0.01 Hz on the vertical and radial component with the aim to constrain the total magnitude of the event (following Kanamori & Rivera, 2008; Duputel et al., 2012). Due to the very long period nature of the W-phase, we expect to characterize the whole complex earthquake. A second full-waveform low frequency (0.001–0.01 Hz) inversion considering longer time windows (referred to as CMT inversion of subevent C) was performed to capture all characteristics of the rupture. For all inversions the AK135 Earth model from Kennett et al. (1995) was assumed.

The same inversion method was applied to 88 out of the 202 globally recorded aftershocks with $M_w \geq 5.0$, but with different parameters. Here waveforms from 200–2500 km epicentral distance were used to ensure good signal-to-noise ratios and exclude saturated data. For the 114 excluded events high seismic noise levels or waveform overlap with stronger events prevented robust moment tensor inversion. Bandpass-filtered (0.02–0.04 Hz for best signal-to-noise ratios) full waveforms were fitted on the vertical, transverse and radial component. The obtained MT solutions and those for five additional earthquakes from the GEOFON MT catalog were clustered (Cesca, 2020) based on the similarity of their focal mechanisms, using the Kagan angle (Kagan, 1991) as metric. Clusters are recognized if there are at least 2 other earthquakes with mutual Kagan angles $\leq 30°$. Further details and waveform fits can be found in Appendix A and Appendix B.

Finite fault dynamics from self-similar dynamic extended rupture model

The self-similar dynamic rupture model (or pseudo dynamic rupture model - PDR) utilizes a flexible 3D boundary element method to invert for the instantaneous slip caused by a prescribed stress drop on each activated patch of an extended rupture, defined by the area behind the rupture front (Metz, 2019; Dahm et al., 2021). As a first order approximation, the rupture speed scales linearly with the S-wave velocity extracted from the layered AK135 Earth model (Kennett et al., 1995). With a prescribed rupture speed model, the rupture front at each time step is approximated using the 2D Eikonal equation.

We integrated the PDR into the Bayesian inversion scheme of Grond (Heimann et al., 2018) as a source option. In our realisation the PDR assumes a planar fault, a constant stress drop and constant rake along the whole plane, which reduces the number of free parameters within the inversion significantly compared to individual rakes and stress drops on each sub fault. Due to this simplified scheme we expect the PDR inversions to focus on the major slip patches.

We do not fix the orientation of the fault, the slip direction (governed by the rake) nor centroid and origin location prior to the inversion, but leave them as parameters in the inversion. Thereby, 13 free parameters are estimated: length, width, strike and dip of the fault plane; origin time and location, both absolute and relative to the fault plane; and rake angle, stress drop, and the scaling coefficient v_r/v_s between the rupture speed v_r and the S-wave velocity v_s. Any deviation between the S-wave velocity of the used Ground model and the true shear wave velocity will also result in a change of the scaling coefficient. Slower S-wave velocities as often observed in megathrusts (e.g. Miller et al., 2021) will cause a decrease of the scaling coefficient. Hence, any interpretation will be done on the absolute rupture velocity instead of the scaling coefficient. Note that the seismic moment is calculated using the inverted slip, area of the rupture plane and the mean shear modulus of the depth section covered by the PDR rupture plane.

We decided not to preconstrain the location of the rupture using a known slab geometry. That allows to access also the location uncertainty in a fully Bayesian manner. In a first approach, we apply the PDR inversion independently to subevents A and D by a careful selection of time windows (example in Fig. 4), considering that between 4000 - 10000 km epicentral distances the high frequency P-waves of subevent D arrive significantly earlier than the high frequency S-waves of event A, thus avoiding wave interference. We use displacement seismograms on vertical and transverse components, bandpass filtered between 0.01–0.05 Hz.

Although such a time separation approach is possible for the smaller subevents A and D, it is suboptimal to analyse the slow rupture processes of subevents B and C in between, because a constructive and destructive superposition of radiated low frequency waves cannot be considered. Therefore, the PDR inversion of subevents B and C was formulated as a joint inversion. Very low frequency vertical and radial displacement records ($0.001 - 0.01$ Hz) were used including the W-phase signal as well as the S-wave and surface waves. The two PDR models have independent parameters allowing also independent fault plane orientations and subevent magnitudes. The new simultaneous Bayesian inversion scheme for source doublets parametrizes the time, distance and azimuth between the two subevents and is described in more detail in Carrillo Ponce et al. (2021). Detailed inversion reports and waveform fits can be found in Appendix C.

Teleseismic back-projection

We used a multi-array back-projection method (Vera et al., 2021) of vertical very short-period P-waves (0.5–2.0 Hz) recorded at several arrays in Chile, the Caribbean, Australia, and South Africa. Each array was weighted individually based on its azimuthal distribution, i.e., proportionally to the sum of the two half-angles measured between the azimuths of target and neighboring arrays (see example in Fig. Appendix D.2a). Combining semblance and energy radiated maps, we are able to characterize the spatial and temporal rupture evolution with associated relative strength of each short-period energy emission above 0.5 Hz.

P-waves were extracted using arrival times from the IASP91 velocity model (Kennett & Engdahl, 1991). Theoretical arrival times have been additionally calibrated using static station corrections following the aftershock calibration method (Palo et al., 2014) to correct for earth heterogeneities and their effect on the arrival times (e.g., Ishii et al., 2007; Palo et al., 2014; Meng et al., 2016). Station corrections are derived as the average residuals of eight aftershocks with thrust mechanisms assumed to rupture the same fault as the mainshocks (Tab. Appendix D.1). Compared to the standard practice of calibrating station corrections based on the catalog hypocentre, this makes the absolute positioning of the rupture track less susceptible to mislocation of any single event.

More details on the teleseismic back-projection are presented in Appendix D.

Tsunami simulation

The South Sandwich rupture has triggered a tsunami that was recorded at a number of tide gauge stations located at various azimuths and distances around the epicenter.

We employ these observations to provide an independent first-order check for our source model. In particular, we would like to check if tsunami arrival times and amplitudes (which are essentially far-field proxis for the position, orientation, and average magnitude of the tsunamigenic slip) are roughly consistent with tide gauge observations. We cannot expect perfect match because of the limitations due to the numerical model and accuracy of the bathymetry (see also comprehensive discussion in Romano et al. (2016)).

We do this first-order validation by simulating tsunami propagation in long wave approximation using the in-house code easyWave, which implements the leap-frog finite difference numerical scheme at a staggered grid according to the TSUNAMI-F1 algorithm by Goto et al. (1997). The initial conditions are set according to the vertical seafloor displacement. This offset was calculated over a 600x600 km grid centered at the joint centroid location of the PDR results of the subevents B and C (Fig. 6), using the PsGrn/PsCmp code by R. Wang et al. (2006), the flat earth approximation and assuming elastic structure as in the AK135 Earth model (Kennett et al., 1995). The tsunami source trigger is assumed to be instantaneous. Despite the relatively long rupture time of ≈220 s, this assumption is still valid since the rupture velocity is at least 5-6 times faster than the tsunami propagation in the source area. Given these initial conditions, tsunami propagation was simulated on a SRTM30 Plus (Becker et al., 2009) bathymetric grid downsampled to a 1 arc minute resolution. As this resolution is too coarse to simulate wave evolution in the vicinity of coastal tide gauges, we used the commonly accepted technique, and recorded simulated waveforms at offshore positions in deep water (at least 50 meters depth) with the subsequent tsunami height projection onto the nearest coast estimated with the coastal amplification factor (Kamigaichi, 2015; Glimsdal et al., 2019). In particular, for tide gauges located at coasts with shallowing bathymetry – stations 'imbt' and 'stan' – we used Green's law (Kamigaichi, 2015), whereas for the stations located in wall-like conditions – 'kepo1', 'mais', and 'prat3' – we used factor 2 which corresponds to the perfect reflection at a vertical wall as derived from linear wave theory. Off-shore waveforms were additionally time-shifted according to the calculated offshore-to-onshore tsunami propagation time assuming linear near-shore bathymetry shallowing (Romano et al., 2016).

Results and Discussion

The 2021 South Sandwich earthquake is characterized by complex rupture processes on the central and southern segments of the South Sandwich subduction zone. The earthquake is bounded by two M_w 7.5–7.6 thrust subevents (A and D) in the north and south of a shallow rupture plane (Tab. 2 and Fig. 3). Both subevents A and D radiated seismic energy in frequencies as expected from standard scaling relations (e.g. Brune, 1970) and are characterized by mean rupture velocities of 1.5–2.1 km/s scaling linearly with the S-wave velocity by a factor of 0.40–0.49. Both A and D occurred as thrust events at the plate boundary of SW and SA plate on trench parallel striking rupture planes with respective centroid depths of 18±5 or 31±4 km. In between both high-frequency subevents, a very shallow segment (top edge depth of 10±4 km) of the plate boundary ruptured over a length of > 450 km with a curved plane striking sub-parallel to the curvature of the plate boundary (subevents B and C) as retrieved from inversion of very low frequency seismograms. A maximum shear slip of 5.8±2.2 m, a total moment release of $2.24 \cdot 10^{21}$ Nm, and v_r/v_s ratios of 0.33 and 0.37 (for both subevents B and C respectively) were obtained, implying a mean rupture velocity in the range of 1.2–1.5 km/s. Both shallow depth and significant co-seismic slip indicate tsunamigenic potential of this phase of the rupture. We will now describe the results of the various inversions in more detail. Probability density functions and complete lists of parameter uncertainties derived from the Bayesian inversions are provided in the Appendix.

The individual PDR inversions of the two high-frequency subevents A and D yield two thrust events (dip 20°) with strikes parallel to the plate boundary. Subevent D occurred 240 km SSW of subevent A about 200 s later, corresponding to a gap of ≈100 s between the end of rupture A and onset of rupture D. (Tab. 2, Appendix C.2 and Fig. 3). The first subevent A is shallower compared to D with top edge depths of 10 km vs. 23 km and has a larger along-strike extent of 150 km vs. 58 km but a smaller maximum slip of 2.3 m vs. 3.1 m. The moderately lower slip and shallower rupture in less rigid material finally makes the moment magnitude of A, M_w 7.57, a little smaller than that of D, M_w 7.61, in spite of the much larger rupture area of the former event. The origin of A at the northern segment of its fault plane leads to bilateral rupture with higher moment release for a duration of 60 s prior to pure unilateral propagation towards south (Fig.3a,c,d). The later subevent D lasted only 24 s and is characterized by mostly down dip and southward rupture propagation. Our inferred rupture propagation of A and D fits well with the results from back-projection of high frequency body waves (Fig. 3c,d), which also indicate southward rupture propagation. The location and timing of subevent D fits well with the area outlined by the largest high-frequency energy emissions, although back projection results indicate a larger extent of this zone. They do also show later emissions than the PDR results would suggest and could image the stopping of the rupture characterized by strong rupture velocity decrease (Madariaga, 1977; Tilmann et al., 2016). A small patch of emitters at 58°S is co-located with the southern termination of the subevent A plane. CMT inversions (Appendix A) also confirm most of the PDR inversion results. Magnitudes are smaller, though, with M_w 7.31 and 7.40 for A and D, respectively and a shorter duration of 21 s estimated for A. The centroid depth extracted from the CMT inversion for A fitting first arriving P and S wave signals only is significantly deeper than obtained using the PDR with 40±6 km compared to 18±5 km. The PDR inversion fitted signals succeeding the first arrivals of P and S wave. These signals are likely emmited by the shallower segment of the megathrust, which ruptured simultaneously with the subevent A (Fig. 3d). Mechanisms, locations and times of A and D are consistent with subevents E1, E2, E4 and E5 by Jia et al. (2022). Our inversion of subevent A as an extended rupture reproduces E1 and E2 with similar location, slightly longer duration and also larger magnitude (M_w 7.6 compared to cumulative M_w 7.4), as it fits a longer part of the first rupture signal. Whilst E4 and E5 match in time, mechanism and location of our subevent D, they show a larger moment release (cumulative M_w 7.9 vs 7.6).

The static and kinematic parameters of the shallow and slow rupturing subevent B were derived from a CMT inversion of the W-phase at 0.001-0.01 Hz, and for subevent C from full waveform CMT (i.e., including surface waves) and PDR (using a joint inversion of two rupture planes), using the same frequency range. The individual CMT point source inversions yield similar thrust mechanisms striking 196–199°and dipping ≈45°, but with an increased oblique component for subevent C compared to B (CMT inversions of subevent B and C in Tab. 2, Fig. 3). The CMT moment magnitude M_w of C, which predominantly fitted the surface waves (Figs. 4, Appendix A.11, Appendix A.12) is estimated with 7.91±0.03 compared to 8.14±0.05 for subevent B. C ruptured later and with a shorter duration (123±4 s vs. 385±21 s for C and B, respectively). Both centroids are located close to the trench with C 216 km further south and significantly shallower (16±6 km) compared to B (32±19 km depth).

The centroid locations of each plane retrieved from joint inversion of two extended PDR planes fit well with the CMT solutions but with a shallower depth for subevent B of 18±4 km indicating robust spatial resolution. Each plane strikes sub-parallel to the plate boundary with respective dips of 30–40° for B and C. Rakes of 96±16 and 111±13° indicate pure thrust for B and oblique thrust for C. Maximum slip of 5.8±2.2 or 5.0±1.7 m with subevent moment magnitudes M_w of 8.02 and 7.98 (cumulative M_w 8.2) were obtained for B and C, respectively. B and C jointly ruptured a 450 km long and 34–49±14 km wide shallow segment of the plate boundary. The rupture started on the northern segment close to the origin of subevent A in time (18:32:44±19 s for B compared to 18:32:54±2 s for A) and space (uncertainties in Figs. Appendix C.1, Appendix C.2). The rupture propagated first bi- and later unilaterally towards the south with slow mean rupture velocities of initially 1.2 km/s during event B, and then 1.5 km/s during event C (Fig. 3c). Rupture velocities at the top edges of the rupture were close to 1.1/1.3 km/s for B and C respectively. The higher speed of C leads to a shorter duration (78 s vs. 163 s) and a higher peak moment rate compared to B (Fig. 3d).

Both CMT and PDR estimate a similar cumulative M_w 8.2–8.25 with a long duration of at least 225 s, covering the central and southern shallow segment of the plate boundary with a joint centroid location close to the GCMT solution and with similar mechanism and magnitude (Tab. 1 and Appendix C.3). As fitting only the very long period W-phase, the CMT inversion of subevent B is unable to capture the nucleation phase accurately but instead characterizes the whole complex rupture process. That is indicated by the negative start of the CMT B source time function as well as by its long duration covering the whole rupture process (Fig. 3d). The rotated focal mechanism of the W-phase based CMT solution, which has a significant NE-striking component, compared to the PDR B solution supports this interpretation (Fig. 3b,d). The joint PDR inversion aims to fit the superposition of both W-phases and surface wave waveforms (Figs. 4 and Appendix C.10–Appendix C.13). In the full waveform inversion we inevitably also fit signals emitted from subevents A and D. That leads to a partial overlap in time with subevents A and D and space with the subevent A (Fig. 3). The spatial gap between the derived best rupture planes of C and D could be caused by the focus on major slip patches of our PDR inversion setup. As shown in Fig. Appendix C.3 we also obtain a larger location uncertainty for rupture plane C. The increased uncertainties in azimuth and distance between B and C might also have caused the unexpected location of the best rupture plane for C partially to the East of the SST. Nevertheless, Thomas et al. (2003) states, that also the location of the SST (as mapped by Pelayo & Wiens, 1989; Bird, 2003) and the uppermost plate interface is not well resolved in this segment of the subduction zone.

We find a strong agreement with the results of Jia et al. (2022) from both their W-Phase and multi-event inversions. The CMT W-phase inversion (subevent B) yields a comparable cumulative duration, magnitude, thrust mechanism and centroid location, but with a steeper dip of the preferred nodal plane (43±16 vs 14°), which could be caused by larger time windows and a broader frequency band used in our case. The PDR mechanisms, magnitudes and centroid locations of B and C coincide well with the subevents E3, E4 and E5. Again our preferred results show larger dips (30–45°), but with large uncertainties of 9–16°(Tabs. Appendix A.2, Appendix C.2 and Appendix C.3). They could be an effect of the curved path of the rupture along the slab, as a strong trade-off between the orientations of nodal planes of the CMT solutions suggest.

Back projected high frequency seismic energy emitters are located mainly to the West and hence down dip of the shallow high slip patch as defined by rupture plane C. This has been observed at different megathrust earthquakes as the 2010 Maule (e.g. Koper et al., 2012; Kiser & Ishii, 2012), 2011 Tohoku (e.g. Lee et al., 2011; Ide et al., 2011; Suzuki et al., 2011; Simons et al., 2011; D. Wang & Mori, 2011; Duan, 2012; Lay, 2018) or 2015 Illapel earthquake (e.g. Tilmann et al., 2016). This characteristic of megathrust events is assumed to be associated with both longer rupture duration in shallow depth and heterogeneous friction or structural features on the shallow plate interface causing only moderate energy emissions along the shallow rupture (Bilek et al., 2004; Lay et al., 2012). We recognize these moderate to low energy emissions co-located with the inverted rupture planes of the subevents A, B and partially C. Their emission times and the retrieved rupture velocity (1.2 km/s) fits well the inverted rupture propagations and velocities of A, B and C (Fig. 3c). With back projection, such slow rupturing stages ($1.0\ km/s \leq v_{rup} \leq 1.5\ km/s$) have been observed in the case of the 2011 Tohoku earthquake (e.g. Meng et al., 2011; D. Wang & Mori, 2011). The strong spatial and temporal coherency between the obtained rupture front propagation from low frequent finite fault inversions and the high frequent back-projection has been observed in lab experiments by Marty et al. (2019).

The spatial extent of the aftershocks from 56–60.5°S confirms the inferred rupture length from the PDR inversions (Fig. 5). Locations are rather diverse with accumulations down dip from the inferred shallow high slip rupture planes of subevents B and C. These aftershocks are co-located with the major back projected high frequency energy emitters, as also observed e.g. at the 2010 Maule earthquake (Palo et al., 2014).

The aftershocks show heterogeneous focal mechanisms; we find 8 clusters consisting of 61 events in total, with 31 unclustered events. The largest cluster 0 indicates oblique thrust faulting with moderate dips, and additionally a number of unclustered events show thrust mechanisms. The location of most of these events is close to the plate interface, and strikes are broadly sub-parallel to the strike directions of the closest trench segments, but dips are mostly too steep to be consistent with a plate interface origin (profiles A-A', B-B', C-C'). Only very few events have both hypocentres and focal mechanism dips consistent with a plate interface origin, and they tend to be the deepest, westernmost thrust events in the aftershock sequence, e.g., the two large unclustered events in the NW of profile C (profile distance $\sim$40 km), and maybe the deep cluster 0 event in profile B. However, the dips of subevents B and C of the main shock also are steeper than the expected inter-plate dip, such that events of cluster 0 and some of the unclustered thrust events can probably be considered to have occurred on the same fault as the main shock.

Multiple clusters with predominant normal faulting are found (1, 3, 5 and 7), which occur in very different tectonic settings: Along the SSR (cluster 1 with large strike slip component), along the SW-SA plate boundary and within the subducted SA plate (profiles A-A', B-B', C-C'). A few of these events occur on the outer rise, especially in the south (cluster 7 in C-C' and also cluster 4 in B-B', which is oblique between strike-slip and normal-faulting). Strong normal faulting events in the outerrise are often observed after large shallow subduction zone ruptures (Bilek & Lay, 2018). The occurrence of this type of events adjacent to subevents B and C along the plate boundary thus lends support to their interpretation as slip along the very shallow megathrust.

Strike slip clusters are found with the events mostly elongated along a SW-striking lineament of events in the downgoing plate (clusters 2 and 6). Multiple clusters with diverse dominant mechanisms near the adjacent plate boundaries (SSR) indicate complex reactivation of secondary faults. The complex patterns in the central segment (profile B-B') are already evident on events recorded prior to the 2021 main shock (Fig. 5b) indicating diverse faulting on unknown faults.

We compared our focal mechanisms to available solutions from GCMT for 16 aftershocks giving a median Kagan angle of $\approx 38°$(see also Fig. Appendix B.1). 11 of the compared events have an acceptable Kagan angle below 45°. Locations changed by 32±6 km with an average depth difference of -10±11 km. Deviations in location and focal mechanism might be caused by our choice of an oceanic ground model and also different station setups used within our inversions compared to GCMT.

The tsunami forward modelling results confirm the tsunamigenic character of the subevents B and C: Simulated tsunami wave heights at tide gauge positions at different azimuths and distances around the epicentre are generally consistent with observations (Fig. 6) with poorer fit for the Stanley tide gauge in the Falklands (station 'stan'). We note that the tsunami observations were not used for the source inversion, i.e., tsunami simulations present a fully independent check of our best source model (here the joint PDR models of subevents B and C).

The polarities of the first onset and the shapes and amplitudes of the first oscillation of modelled and observed tsunami waves show good agreement. The increasing differences at later times are expected and arise due to the simplifying assumptions in the forward modeling as these are strongly affected by local resonances and reflections. Resolving these effects would require high-resolution coastal bathymetry and thus cannot be reproduced with the global bathymetry dataset used in our modelling.

The geographical pattern of wave propagation (Fig. 6a) shows the largest wave heights to the East and West of the SST, as expected from the rupture geometry and mechanism, with maximum wave heights up to > 1 m along the South Sandwich Islands and South Georgia. It is in good agreement with findings reported by Roger et al. (2022) which also show the wave guiding effect of the shallower rift systems of the SA-AN and Africa-AN plates with enhanced wave heights there. Less significant local highs in wave heights are predicted in further directions, e.g., along a South East striking trajectory as a result of the complex ground displacement pattern.

Slowing down of rupture velocities in the shallower parts of the plate boundary have been observed worldwide e.g. the 2010 Maule, Chile earthquake (e.g. Koper et al., 2012; Kiser & Ishii, 2012), the 2011 Tohoku, Japan earthquake (e.g. Lee et al., 2011; Ide et al., 2011; Suzuki et al., 2011; Simons et al., 2011; D. Wang & Mori, 2011; Duan, 2012; Lay, 2018) or the 2015 Illapel, Chile earthquake (Tilmann et al., 2016), and often been associated with a combination of small shear wave velocities and enhanced fluid pore pressures (e.g., Song et al., 2009). Enhanced fluid pore pressure is also postulated to control the occurrence of slow slip events in subduction zones (e.g., Kodaira et al., 2004; Audet et al., 2009; Kato et al., 2010), as an extreme example of slow earthquake rupture.

Recent laboratory studies on frictional rupture under varying fluid overpressure support such an explanation (Passelegue et al., 2020). Experiments could reproduce the full range of observed rupture velocities on the same interfaces, only controlled by the initial effective stress which defines the available shear stress and fracture energy at the onset of slip. Large initial shear stress, meaning small fluid pore pressure, seemed to promote fast rupture velocities and fast slip rates, while high pore pressures lead to slow rupture velocities.

Conclusions

Our analysis of the 2021 South Sandwich earthquake elucidated the complex interaction of smaller subevents with a large and shallow slow rupturing subevent within one earthquake along the curved slab interface using multiple independent techniques. We could link different stages of the complex earthquake to the different results obtained by international agencies, which shows the strong method dependency of their results when applied to such a complex rupture. Finally we were able to link the recorded tsunami to the slow rupturing event. The comparison with known large tsunamigenic thrust events as the 2010 Maule, 2011

Tohoku or 2015 Illapel earthquakes revealed strong similarities in the static and dynamic rupture properties as well as in distribution of back-projected energy and aftershocks.

This earthquake highlights the necessity of a more comprehensive analysis of seismic signals for tsunami early warning, especially where no near field GNSS stations are available to constrain the rupture.

Data and Resources

Seismic broadband recordings for the main shock and the aftershocks were downloaded from the Incorporated Research Institutions for Seismology (IRIS) Data Management Center (`https://ds.iris.edu/wilbert3/find_event`, last accessed November 2021) and the GEOFON program of the GFZ German Research Centre for Geosciences using data from the GEVN partner networks (last accessed November 2021). A detailed overview on the used networks is given in the supplement. Event information was downloaded from Global CMT (Dziewoński et al., 1981; Ekström et al., 2012), USGS (U.S. Geological Survey (USGS), 2020) and the GEOFON program of the GFZ German Research Centre for Geosciences using data from the GEVN partner networks. Tide gauge data was provided by Flanders Marine Institute (VLIZ), Intergovernmental Oceanographic Commission (IOC) (2021). Bathymetric data from NOAA National Geophysical Data Center (2009) was used for the plots.

The used software included Pyrocko (Heimann et al., 2019), Grond (Heimann et al., 2018), GMT 5.4 (Wessel et al., 2013) and Seiscloud (Cesca, 2020) for the seismological studies and plots. Green's Functions used within Grond were calculated using QSSP, PsGrn, PsCmp and Pyrocko (R. Wang et al., 2006, 2017; Heimann et al., 2017). Tsunami modelling was done using easyWave (`https://www.gfz-potsdam.de/en/software/tsunami-wave-propagations-easywave`).

Table 2. Major results for the individual subevents and from different approaches

Subevent	A	B		C		D	all
Method	PDR	CMT	PDR	CMT	PDR	PDR	BP†
Period range [s]	100–20	1000–100		1000–100		100–20	2–0.5
Geometry							
length [km]	150±32	-	270±56	-	178±48	58±11	462
width [km]	42±7	-	34±10	-	49±14	48±8	-
strike	147°±16°	199°±23°	172°±8°	196°±21°	218°±9°	219°±9°	-
dip	21°±5°	43°±16°	29°±13°	45°±10°	39°±9°	20°±2°	-
rake	80°±11°	86°±34°	96°±16°	64°±36°	111°±13°	128°±8°	-
*distance [km]	243 (A–D)	216 (C–B)	202±71 (C–B)	-	-	-	-
*azimuth	199° (A–D)	183° (C–B)	184°±14° (C–B)	-	-	-	-
centroid depth [km]	18±5	32±19	18±4	16±6	25±4	31±4	-
Kinematics							
origin time	18:32:54±2 s		18:32:44±19 s		18:35:15±13 s	18:36:01±2 s	-
centroid time	18:33:35	18:35:09±12 s	18:33:55	18:36:09±2 s	18:35:53	18:36:17	-
v_{rup} [km/s]	1.5		1.2		1.5	2.1	1.2
duration [s]	81	385±21	163	123±4	78	24	300
Magnitude							
max. slip [m]	2.3±0.5	-	5.8±2.2	-	5.0±1.7	3.1±0.5	-
M_w	7.57	8.14±0.05	8.02	7.91±0.03	7.98	7.61	-
$\sum M_w$	7.79 (A+D)	8.25 (B+C)	8.20 (B+C)	-	-	-	-

† Back-projection

* given with respect to centroid location

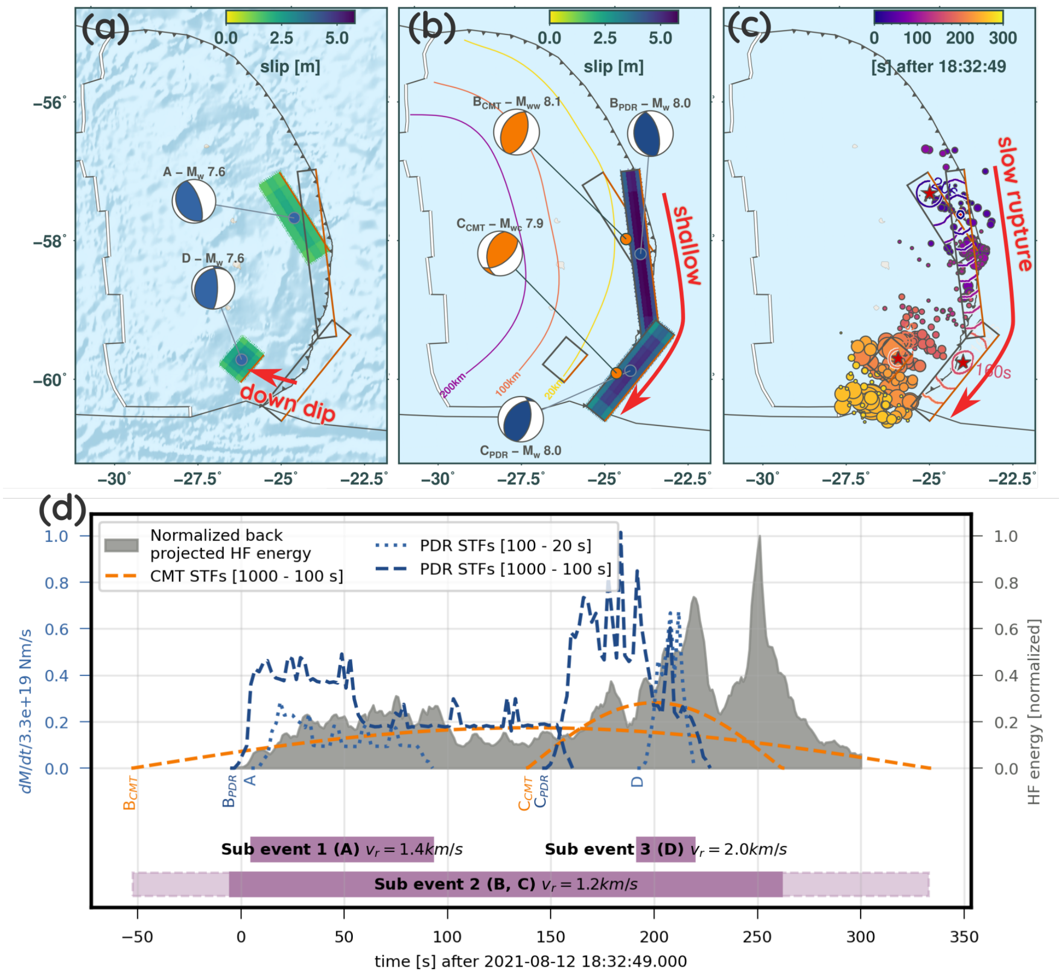

Figure 3. Results of the multi-frequency analysis including key interpretations (red arrows). (a) Final static slip maps and associated centroid MTs retrieved from the body wave inversions (0.01–0.05 Hz) for subevents A and D using the PDR. (b) shows the results for the very low frequency CMT and PDR inversions of subevents B and C. Rectangular outlines in (a), (b) show the location of the PDR solutions for subevents B, C or A, D, respectively (visualises spatial relationships between the overlapping rupture planes). (c) shows the kinematics of the rupture. Contours indicated rupture propagation derived from PDR with respective subevent origins as red stars. Dots show high frequency energy emitters (0.5-2 Hz, size scales with energy release) from backprojection. (d) Comparison of the normalized, radiated high-frequency energy backprojected to the moment rate source time functions (STF) retrieved from waveform inversions in different frequency ranges and with different approaches. The time reference is the origin time of the first

subevent in the GEOFON catalogue.

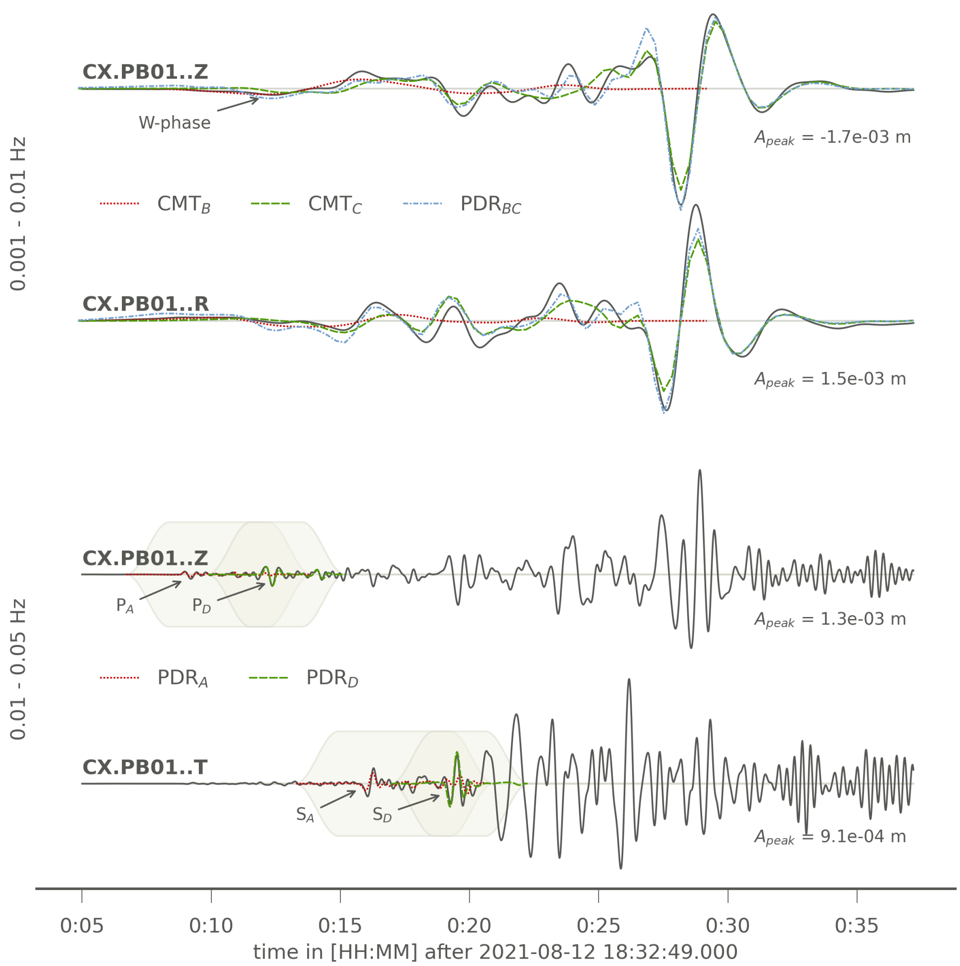

Figure 4. Waveform fits of the vertical and horizontal components for the seismic station CX.PB01.00 (distance: ≈ 5500 km, azimuth: ≈300°. Fits for the PDR and CMT inversions of subevents B and C are shown in the top rows, for the high frequent (0.01–0.05 Hz) PDR inversions of subevent A and D in the bottom rows (Tab. 2). Dark lines show the filtered, observed displacement traces, colored lines the filtered and tapered synthetic signals of the best model within each inversion given in the legend. Synthetic traces are only drawn for the time windows defined within each inversion. Peak amplitudes of each observed, filtered trace are used for normalization and are given as A_{peak}. Major phases (P, S and W-phase) are annotated. Exemplary shape and position of the applied cosine tapers are shown as shaded areas indicating the chosen time windows within the inversion for fits of subevents A and D.

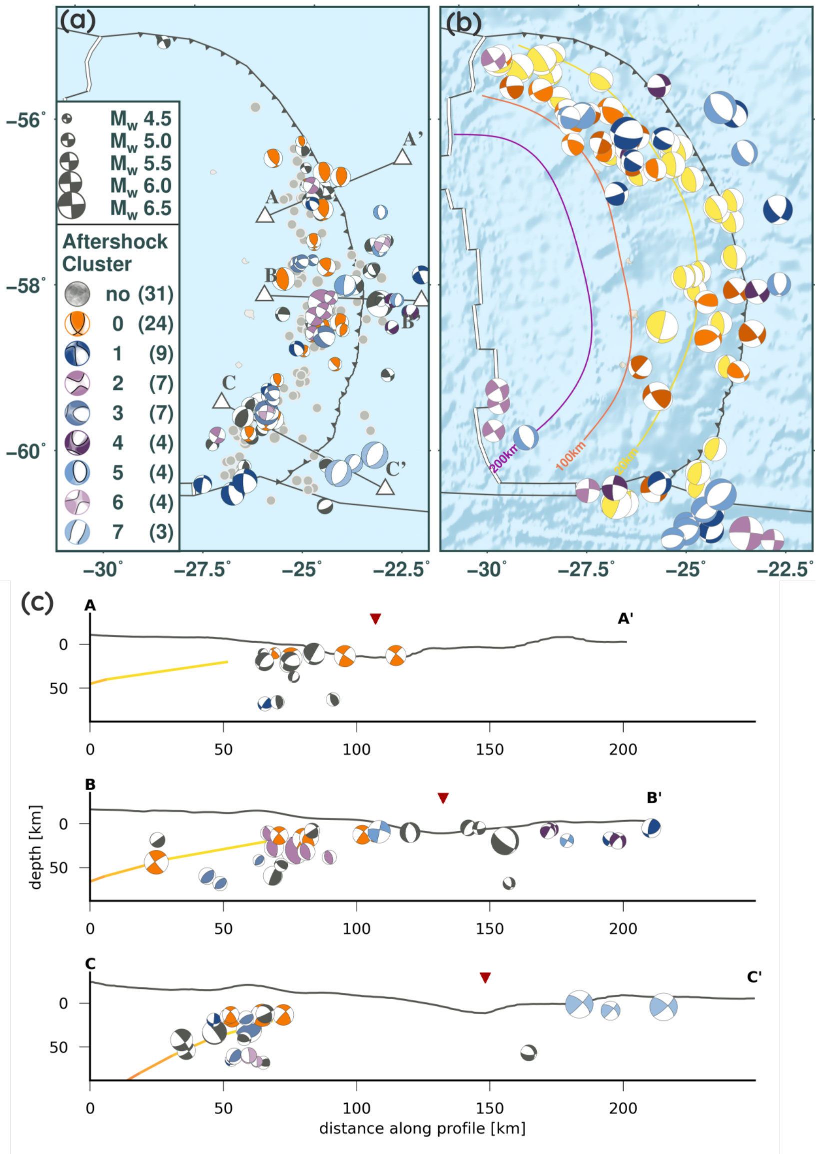

Figure 5. Aftershock centroid locations and mechanisms are shown as map (a) and cross sectional view along three profiles $A-A'$, $B-B'$ and $C-C'$ (c). (b) gives pre-event source mechanisms of GCMT solutions ($M_w > 6$ - locations of all $M_w > 5$ events are shown in Fig. 1). Focal mechanisms are scaled with magnitude. Their colors indicate cluster families (see legend in (a), where fuzzy moment tensors of each cluster are shown, with the representative nodal plane indicated by dark line). Grey dots in (a) show aftershocks from August 12, 2021 until August 31, 2021 taken from a joint USGS and GCMT catalog. The SLAB2.0 slab interface (Hayes et al., 2018) is indicated by iso-depth lines in (b) and is shown as a colored line along each profile in (c). Grey lines show the bathymetry (ETOPO1 with vertical exaggeration factor of 6). The red triangle indicates the position of the trench defined by bathymetry.

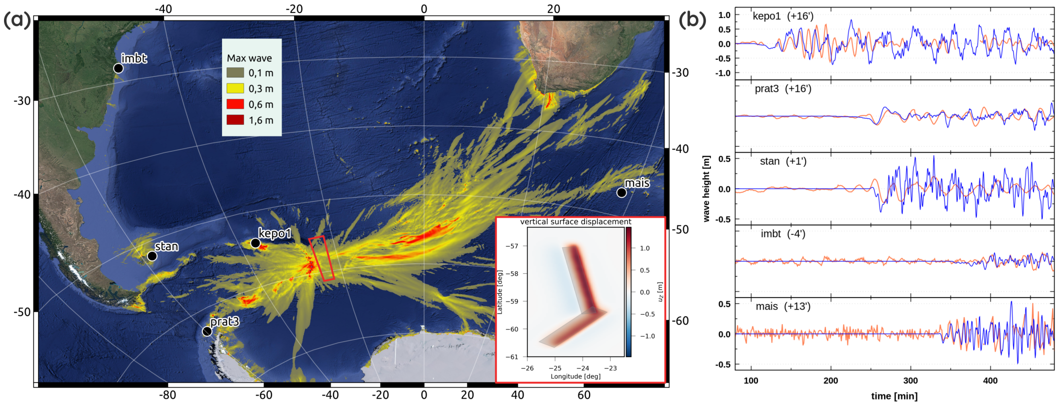

Figure 6. Forward tsunami modeling with initial conditions corresponding to the vertical seafloor displacement as predicted by the PDR model results for subevents B and C. Tsunami triggering is assumed as instantaneous vertical displacement of the seafloor at the joint centroid time of 18:34:46. (a) Maximum tsunami wave heights (values < 0.1 m clipped). Also shown are positions of tide gauges. The insert indicates initial conditions for tsunami modeling located within the red box on the map. (b) Modeled (blue) vs observed (red) mareograms at the tide gauges sorted by distance to the epicentre. Values in brackets indicate additional time shifts in [min] applied for the optimal fit (see Romano et al., 2016). Note, that all data except 'kepo1' are plotted in the same scale.

Data Availability Statement and Declaration

All data used in this study are openly available from the sources listed in Data and Resources.

Contributions of the authors

CMT inversions of the main shocks have been contributed by ACP and MM. The aftershock analysis was done by SC. FV performed the back-projection. MM implemented the PDR inversion approach into Grond and applied the PDR inversion using the double PDR technique jointly developed by ACP and MM. AB conducted the tsunami study. MM, FV, ACP, SC and AB have been responsible for the writing. MM prepared the figures of the main text. FT and TD have contributed to the text and guided the studies. JS provided GEOFON data and feedback and suggestions through the course of the study.

Declaration of Competing Interests

The authors declare no competing interests.

Acknowledgments

Malte Metz is supported by BMBF project EWRICA (03G0891B), Angela Carrillo Ponce and Felipe Vera received funds by the National Agency for Research and Development (ANID)/Scholarship Program: Doctorado BECAS CHILE 2019-72200544 (ACP) and 2017-72180166 (FV).

Appendix A Main shock moment tensor inversion

Moment tensors are the mathematical representation of a seismic source based on generalized force couples, and the centroid moment tensor method relates those force couples with the ground motion generated by them as long as a point-source characterization is well suited for the evaluated problem. The centroid moment tensor inversion returns the centroid location and time, duration, and the six independent moment tensor components of the source, which encode the scalar moment and focal mechanism of the event.

A1 Centroid and W-phase moment tensor inversion of the doublet

In order to characterize the South Sandwich August 12, 2021 earthquake , we apply a centroid moment tensor inversion for each subevent individually by inverting them using different distance-dependent time windows (Tab. Appendix A.1). We use the signals of 64 broadband stations spatially well distributed and located at teleseismic distances (4000-10000 km), filtered in the frequency band of 0.01-0.03 Hz to fit bodywaves in the vertical (for P phases) and transverse (for the S phases) components in the time domain and equally weighted. A separate inversion was performed using the W-phase of the main shock in the frequency range of 0.001-0.01 Hz (Kanamori & Rivera, 2008; Duputel et al., 2012) to cover lower frequencies and validate the magnitude estimate. Figures Appendix A.2, Appendix A.7, Appendix A.10 and Appendix A.13 show the azimuthal distributions used for the different subevents.

The filtering of all waveforms was carried out in frequency domain using a cosine taper. With a given frequency range the cosine taper is characterized as: $f_{min}/1.5$ - start of fading in, f_{min} - end of fading in, f_{max} - start of fading out, $f_{max} \cdot 1.5$ - end of fading out, so the plateau of the taper is between f_{min} and f_{max}.

The inversions are performed with Grond (Heimann et al., 2018), an open source software tool for robust characterization of earthquake sources included in the Pyrocko environment (Heimann et al., 2017). The synthetic seismograms in these inversions are rapidly computed using a global precalculated Green's functions store with a sampling rate of 0.5 Hz. The Green's functions were calculated with the QSSP code developed by R. Wang et al. (2017). The partical swarm optimizations for CMT inversion of subevent A and D took 70000 iterations each while inversion of subevents B and C converged after 50000 iterations. The uncertainties for every resolved parameter were determined by bootstrapping the data considering 100 different configurations. We consider the mean moment tensor solutions.

Uncertainties in determined parameters for all events are shown in Figure Appendix A.1 and Table Appendix A.2, waveform fits and the azimuthal station distribution and weighting in Figures Appendix A.5–Appendix A.15).

According to our results, subevents A and D are separated by 182 s in time and 285 km in distance and their magnitudes are M_w 7.3 and M_w 7.4 respectively. This doublet is composed of two predominantly thrust events with dip angles that fit well with the assumption that they occur on the plate interface (Table Appendix A.2).

Table Appendix A.1. Choosen dynamic time windows for the inversions. Corner times of the used cosine taper are defined as $t_{min}, t_{min} + t_{taper}, t_{max} - t_{taper}, t_{max}$ with respect to the inverted event centroid time*

Inversion	A_{CMT}	B_{CMT}	C_{CMT}	D_{CMT}
P-wave time window relative to t_P				
t_{min} [s]	-220 (100)	-	-	-130 (100)
t_{max} [s]	+70 (100)	-	-	+160 (100)
S-wave time window relative to t_S				
t_{min} [s]	-220 (100)	-	-	-130 (100)
t_{max} [s]	+70 (100)	-	-	+160 (100)
W-Phase time window relative to t_P				
t_{min} [s]	-	-1000 (1000)	-	-
t_{max} [s]	-	+1100 (1000)	-	-
Full waveform inversion time window relative to t_S				
t_{min} [s]	-	-	-1000 (1000)	-
t_{max} [s]	-	-	$v_{surf}(2.0)^{\dagger}$ + 1000 (1000)	-

t_P - P wave arrival time using AK135

t_S - S wave arrival time using AK135

* - Format: <time> (taper)

† - $v_{surf}(XX)$ Indicating surface wave arrival with velocity of XX km/s

Table Appendix A.2. MT inversion results for the given subevents

Event	A	B	C	D
Latitude [°±km]	-57.407±8	-58.036±120	-59.977±27	-59.864±13
Longitude [°±km]	-24.943±12	-24.554±35	-24.720±9	-26.276±12
Centroid time [s]	18:33:13±0	18:35:09±12	18:36:10±2	18:36:15±1
M_w	7.31±0.05	8.14±0.05	7.91±0.03	7.40±0.03
Depth [km]	40±6	32±19	16±6	29±6
Strike [°]	127±12	199±23	196±21	237±7
Dip [°]	19±2	43±16	45±10	29±3
Rake [°]	62±9	86±34	64±36	133±5
Duration [s]	21±6	385±21	123±4	18±6

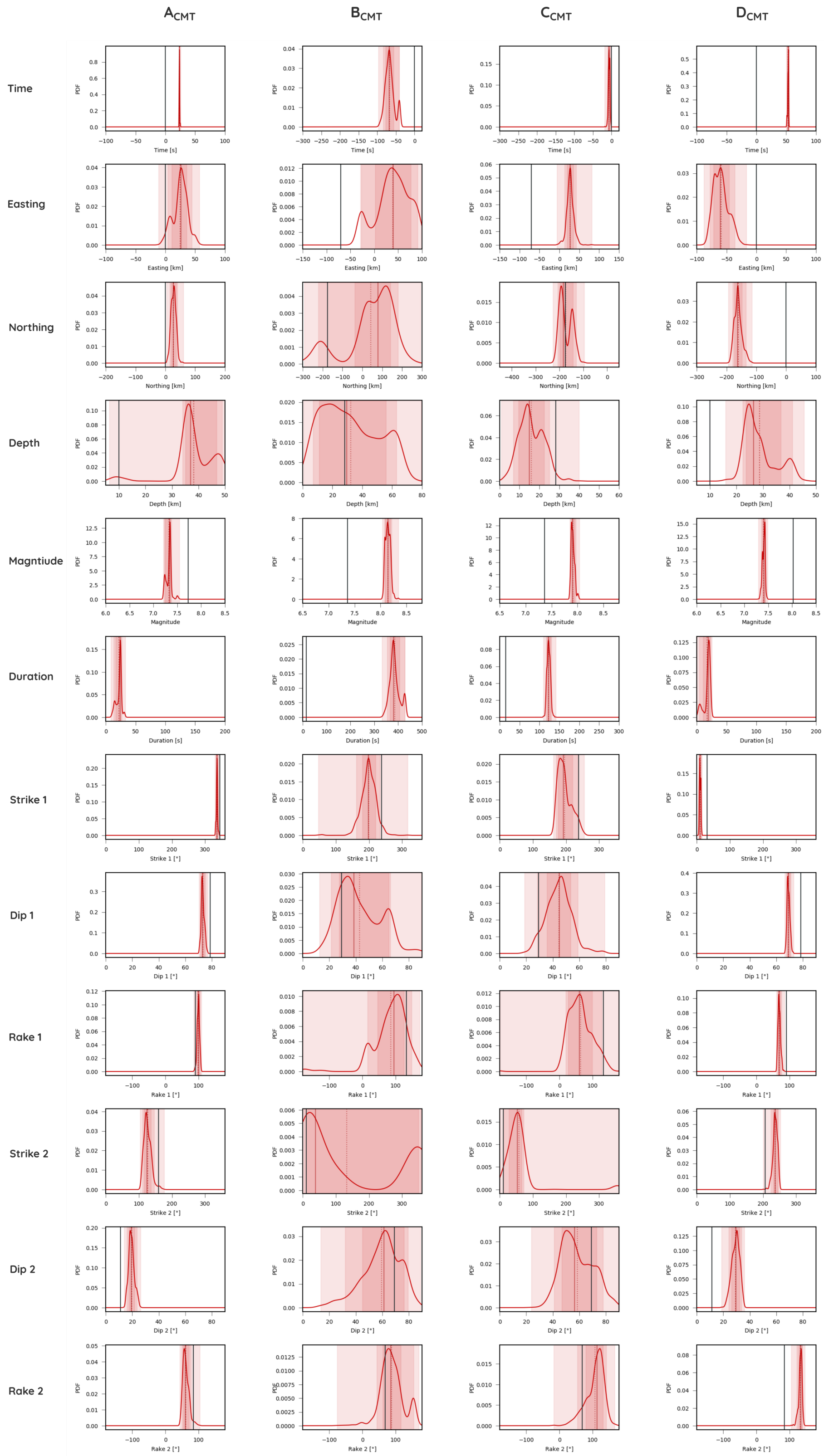

Figure Appendix A.1. Parameter distribution of the tested models for all CMT inversions.

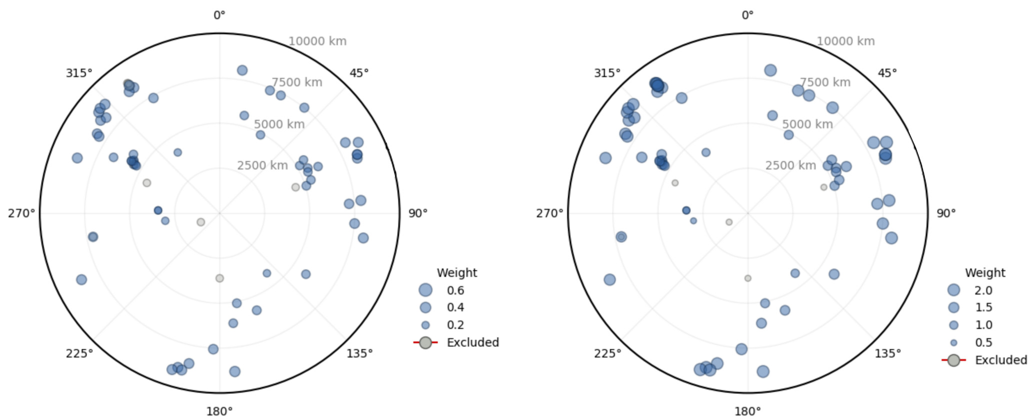

Figure Appendix A.2. CMT for event A - azimuthal distribution and weights for the transverse component (left) and the vertical components (right).

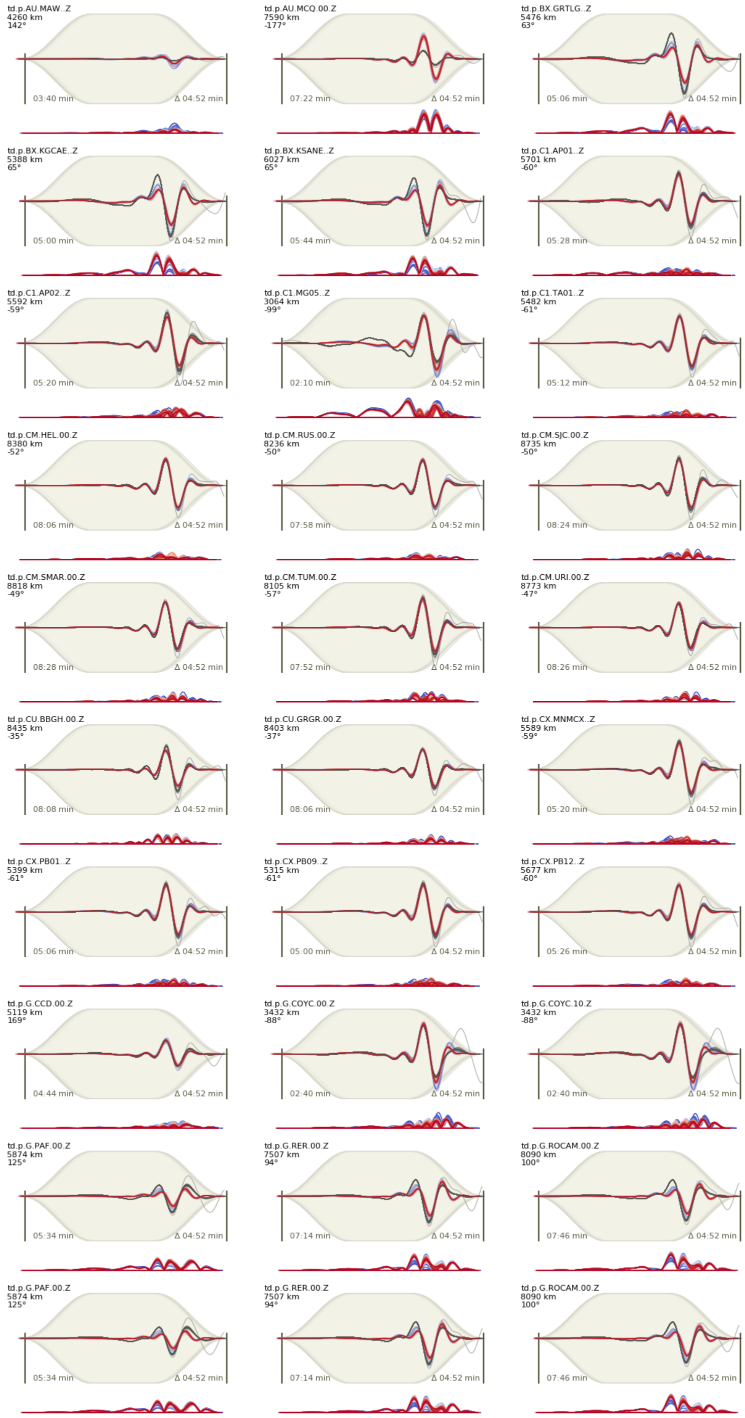

Figure Appendix A.3. Waveform fits of the vertical component retrieved from the CMT inversion for subevent A (part 1), bandpass filtered (0.01–0.03 Hz). Observed traces are black, modelled colored with red indicating smaller misfits vs blue color indicating higher model misfits. Times are given relative to 2021-08-12 18:33:13.

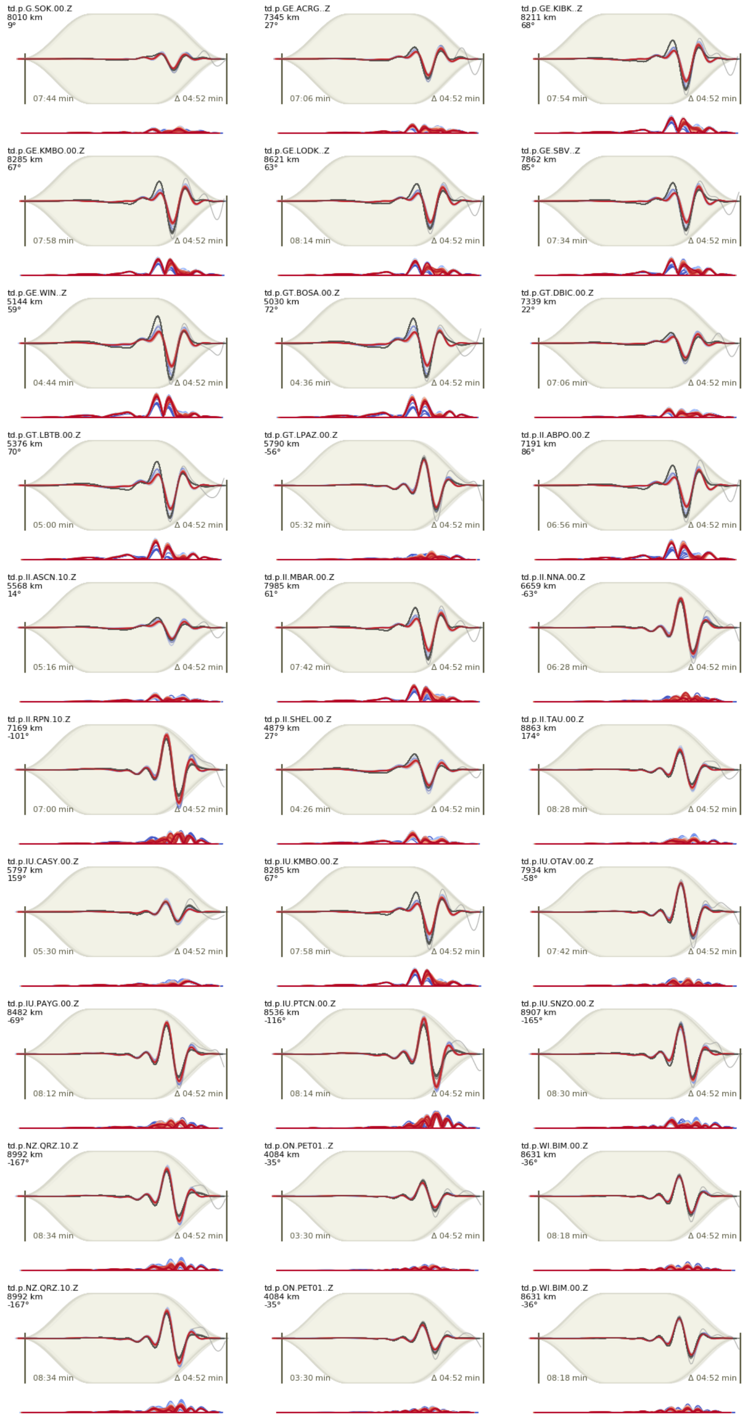

Figure Appendix A.4. Waveform fits of the vertical component retrieved from the CMT inversion for subevent A (part 2), bandpass filtered (0.01–0.03 Hz). Observed traces are black, modelled colored with red indicating smaller misfits vs blue color indicating higher model misfits. Times are given relative to 2021-08-12 18:33:13.

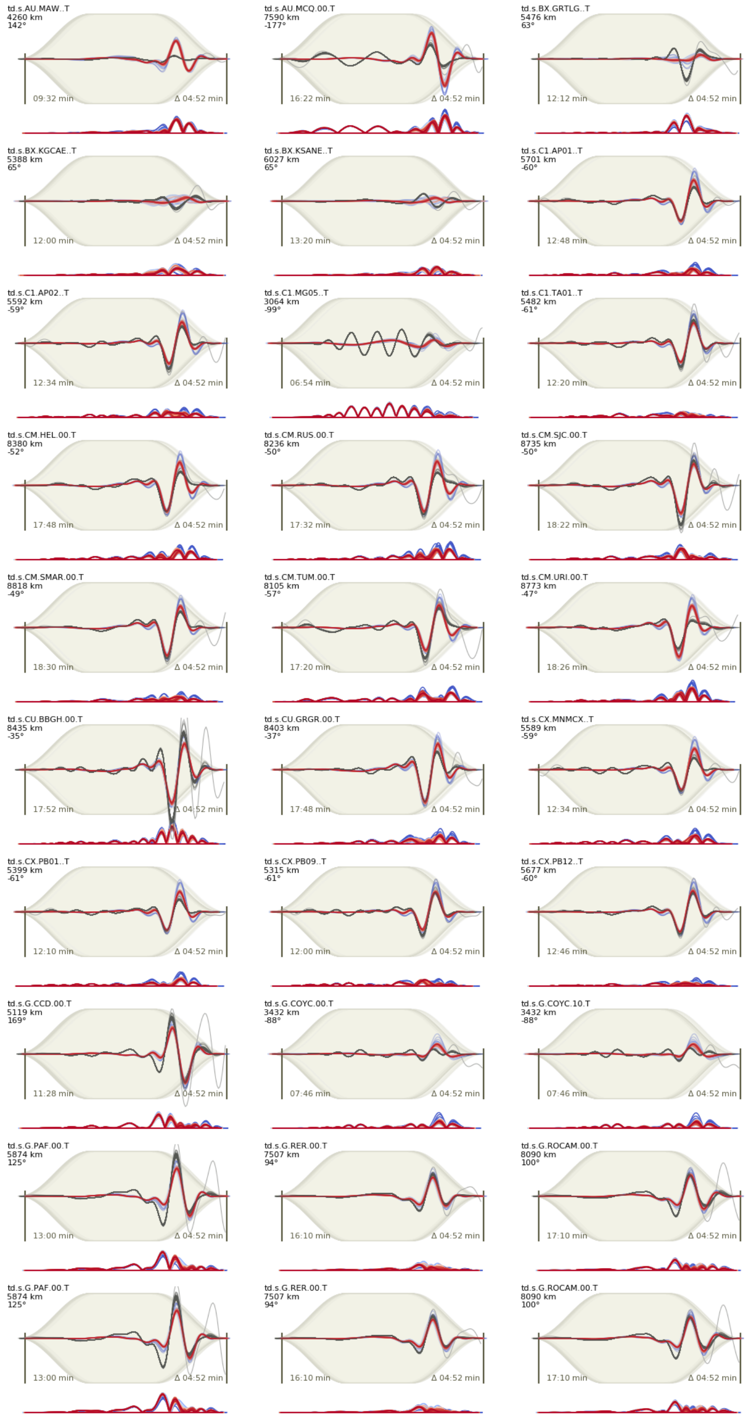

Figure Appendix A.5. Waveform fits of the transverse component retrieved from the CMT inversion for subevent A (part 1), bandpass filtered (0.01–0.03 Hz). Observed traces are black, modelled colored with red indicating smaller misfits vs blue color indicating higher model misfits. Times are given relative to 2021-08-12 18:33:13.

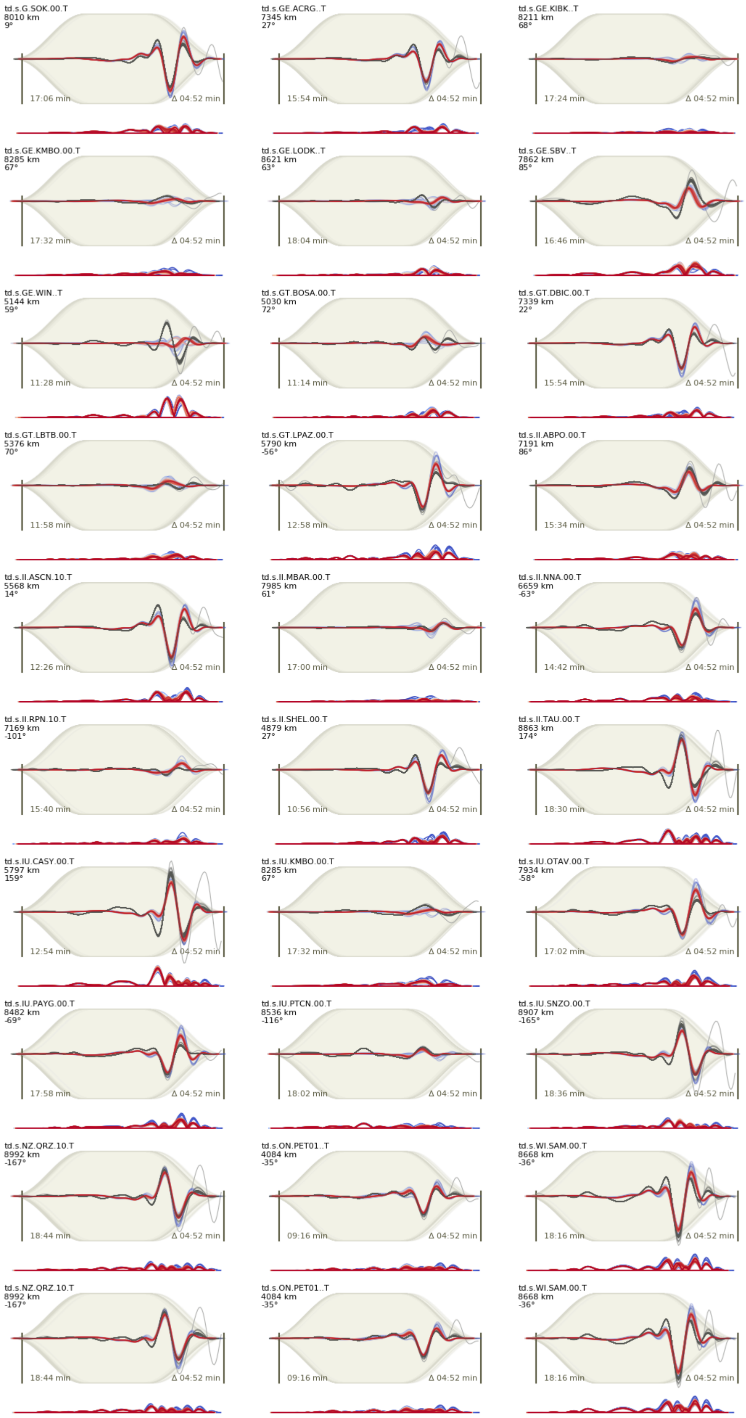

Figure Appendix A.6. Waveform fits of the transverse component retrieved from the CMT inversion for subevent A (part 2), bandpass filtered (0.01–0.03 Hz). Observed traces are black, modelled colored with red indicating smaller misfits vs blue color indicating higher model misfits. Times are given relative to 2021-08-12 18:33:13.

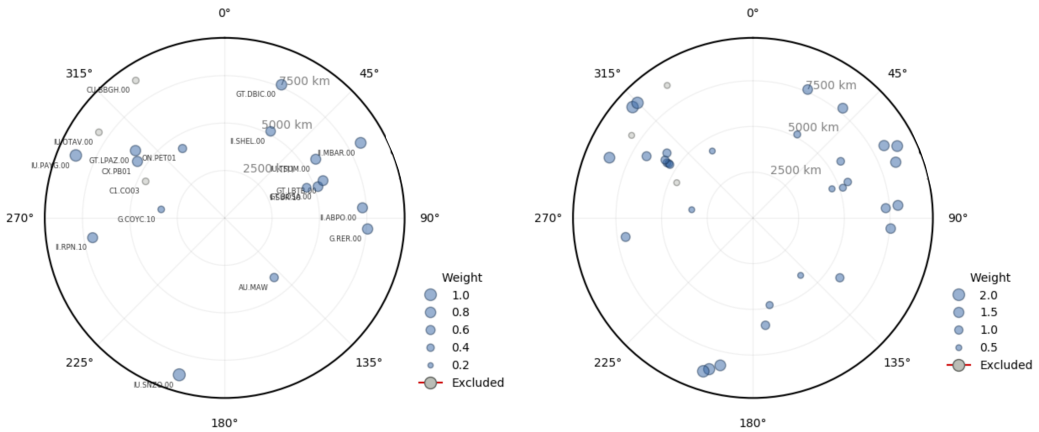

Figure Appendix A.7. CMT for event B - azimuthal distribution and weights for the radial component (left) and the vertical components (right).

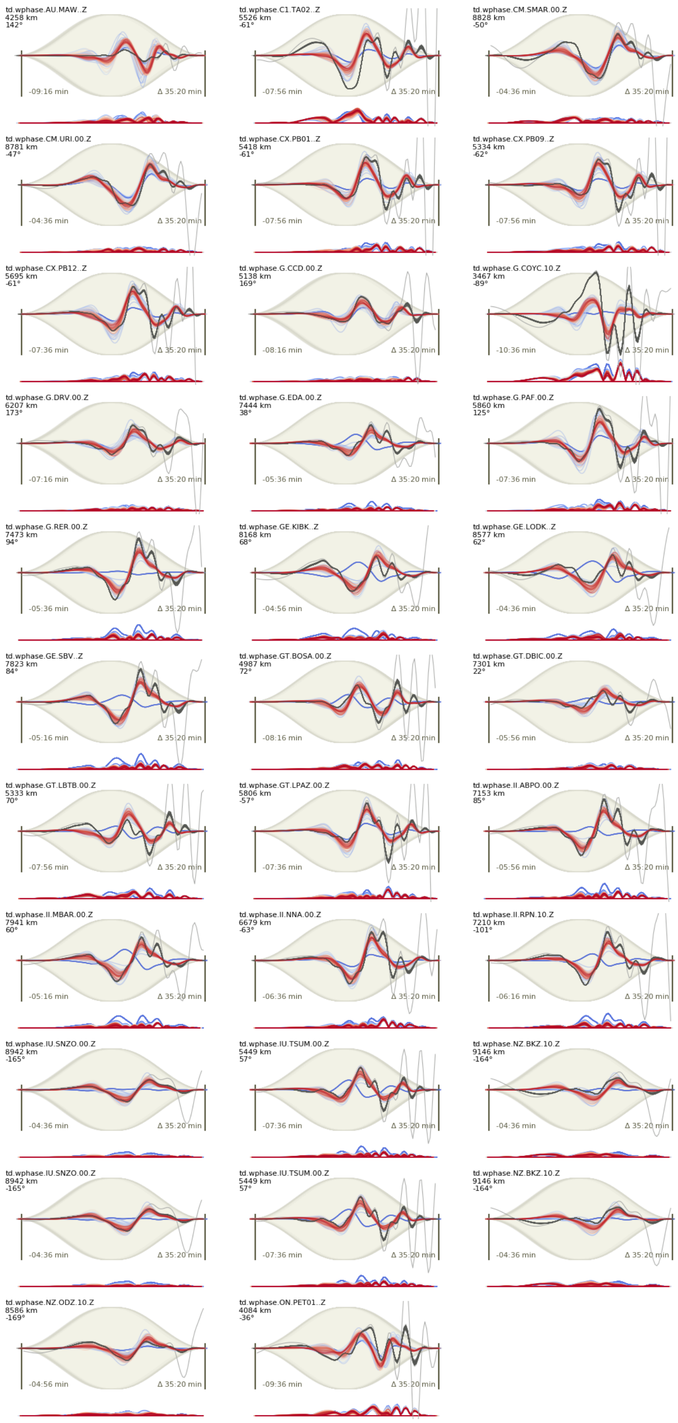

Figure Appendix A.8. Waveform fits of the vertical component retrieved from the CMT inversion for subevent B, bandpass filtered (0.001–0.01 Hz). Observed traces are black, modelled colored with red indicating smaller misfits vs blue color indicating higher model misfits. Times are given relative to 2021-08-12 18:35:05.

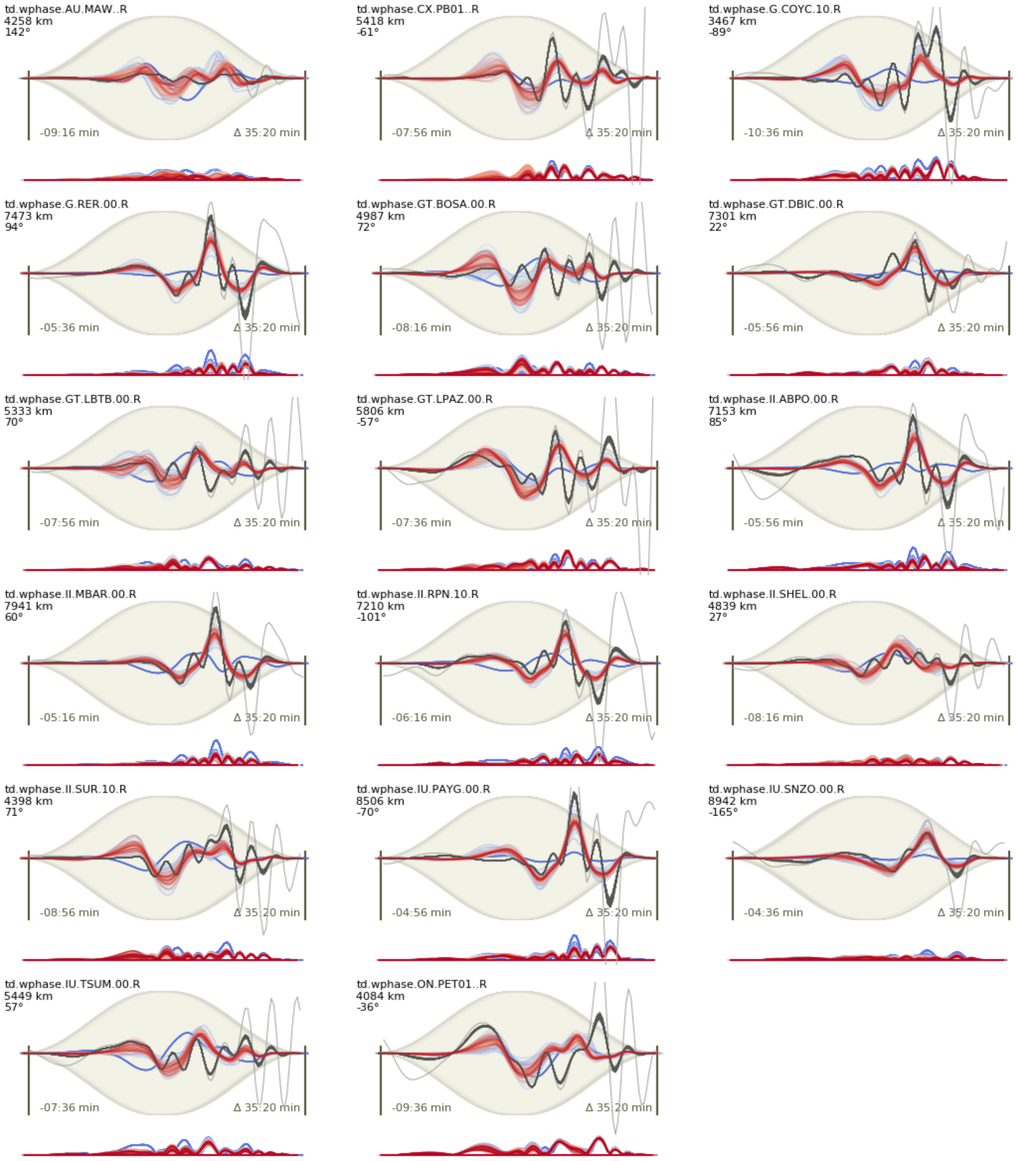

Figure Appendix A.9. Waveform fits of the radial component retrieved from the CMT inversion for subevent B, bandpass filtered (0.001–0.01 Hz). Observed traces are black, modelled colored with red indicating smaller misfits vs blue color indicating higher model misfits. Times are given relative to 2021-08-12 18:35:05.

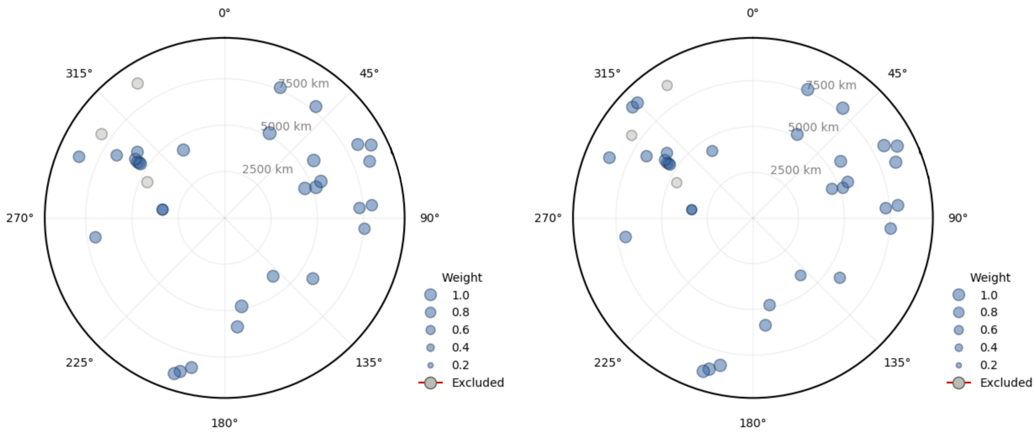

Figure Appendix A.10. CMT for event C - azimuthal distribution and weights for the radial component (left) and the vertical components (right).

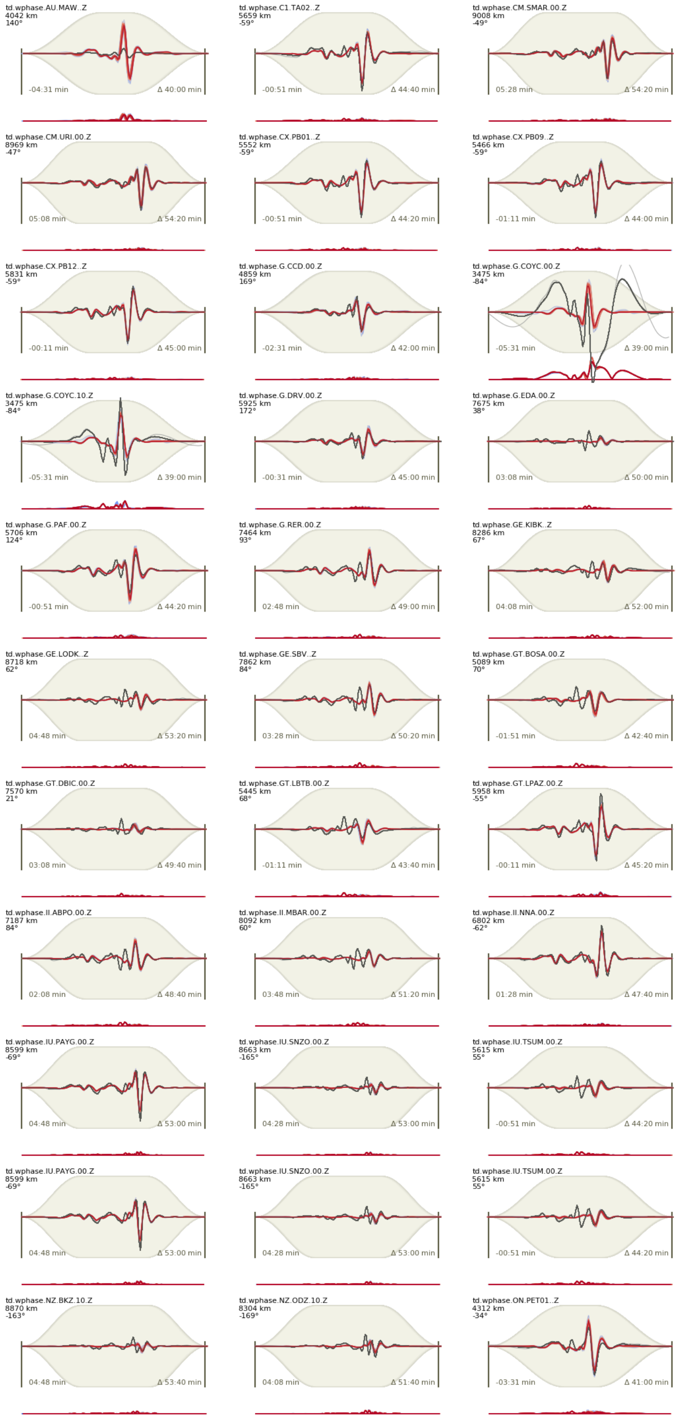

Figure Appendix A.11. Waveform fits of the vertical component retrieved from the CMT inversion for subevent C, bandpass filtered (0.001–0.01 Hz). Observed traces are black, modelled colored with red indicating smaller misfits vs blue color indicating higher model misfits. Times are given relative to 2021-08-12 18:36:09.

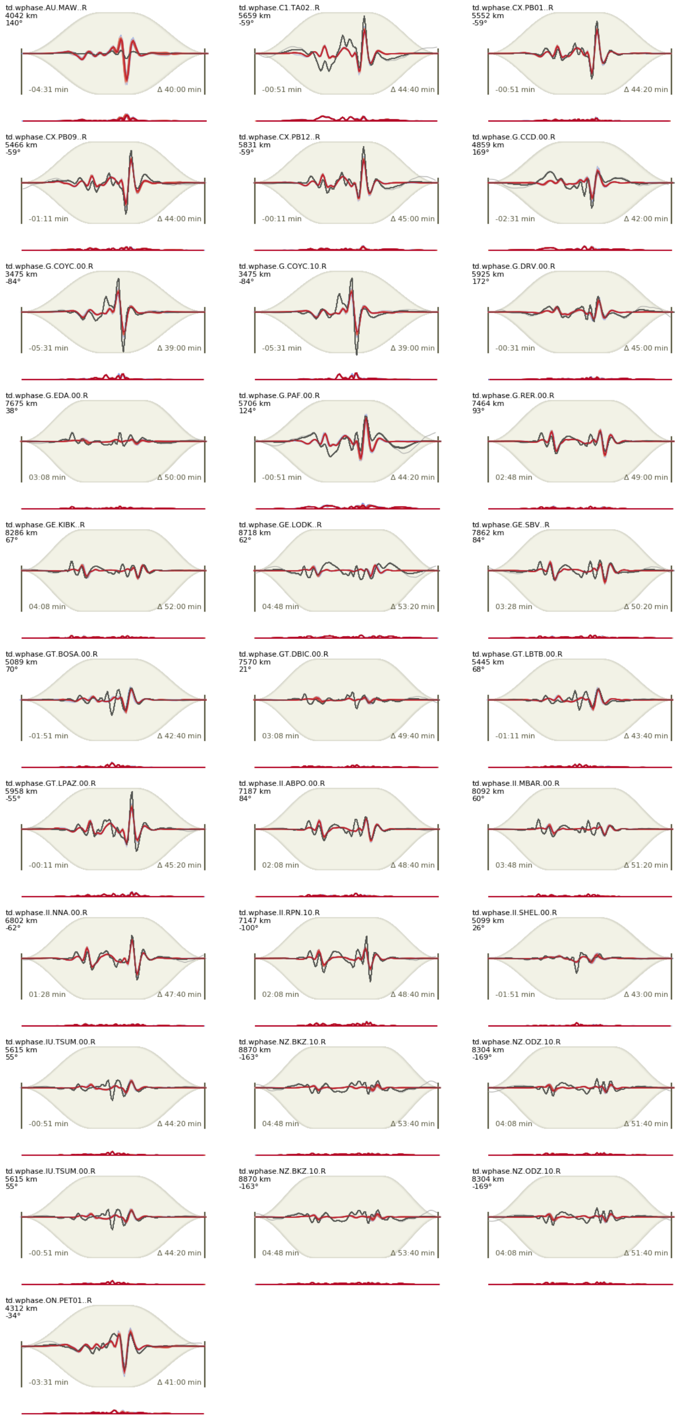

Figure Appendix A.12. Waveform fits of the radial component retrieved from the CMT inversion for subevent C, bandpass filtered (0.001–0.01 Hz). Observed traces are black, modelled colored with red indicating smaller misfits vs blue color indicating higher model misfits. Times are given relative to 2021-08-12 18:36:09

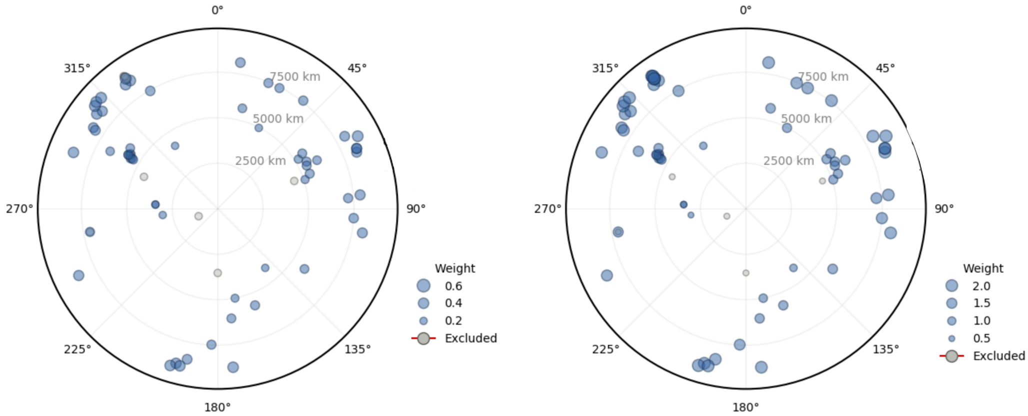

Figure Appendix A.13. CMT for event D - azimuthal distribution and weights for the transverse component (left) and the vertical components (right).

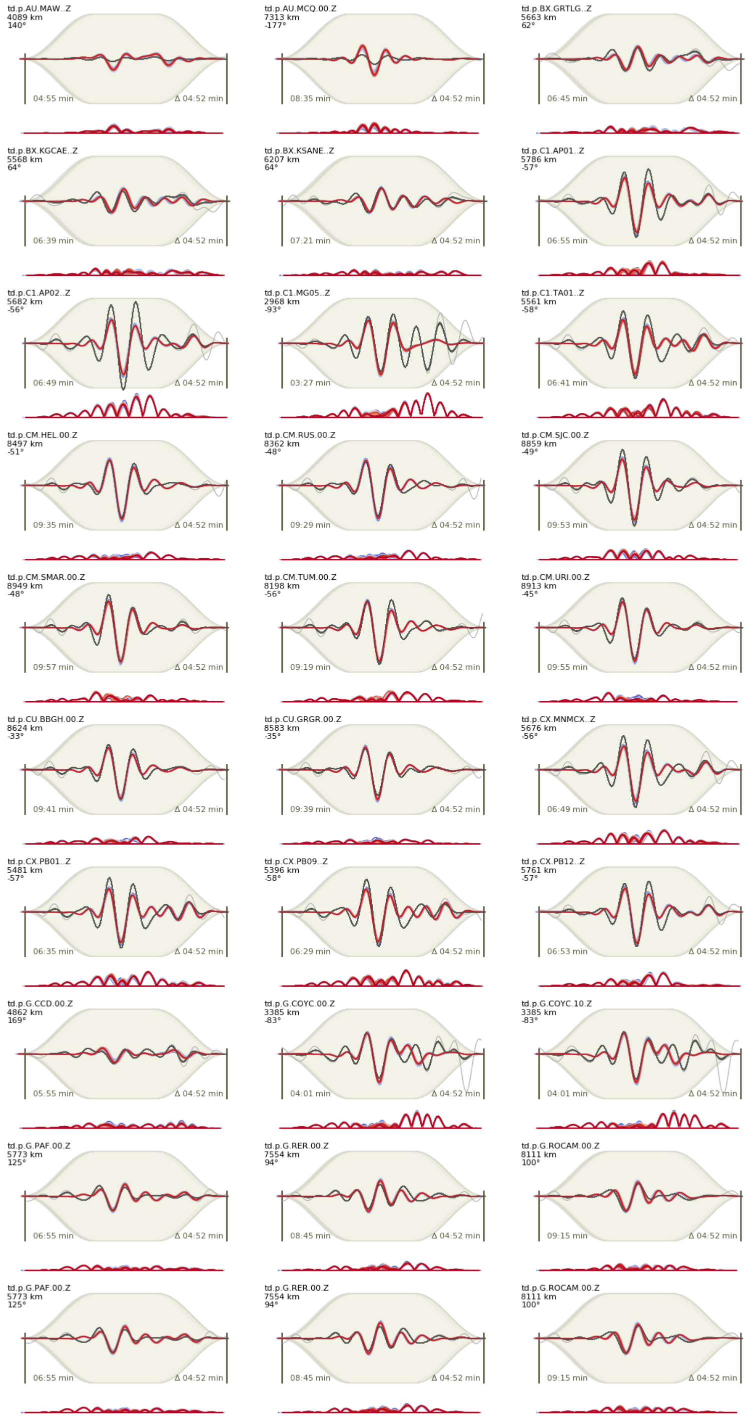

Figure Appendix A.14. Waveform fits of the vertical component retrieved from the CMT inversion for subevent D (part 1), bandpass filtered (0.01–0.03 Hz). Observed traces are black, modelled colored with red indicating smaller misfits vs blue color indicating higher model misfits. Times are given relative to 2021-08-12 18:36:16.

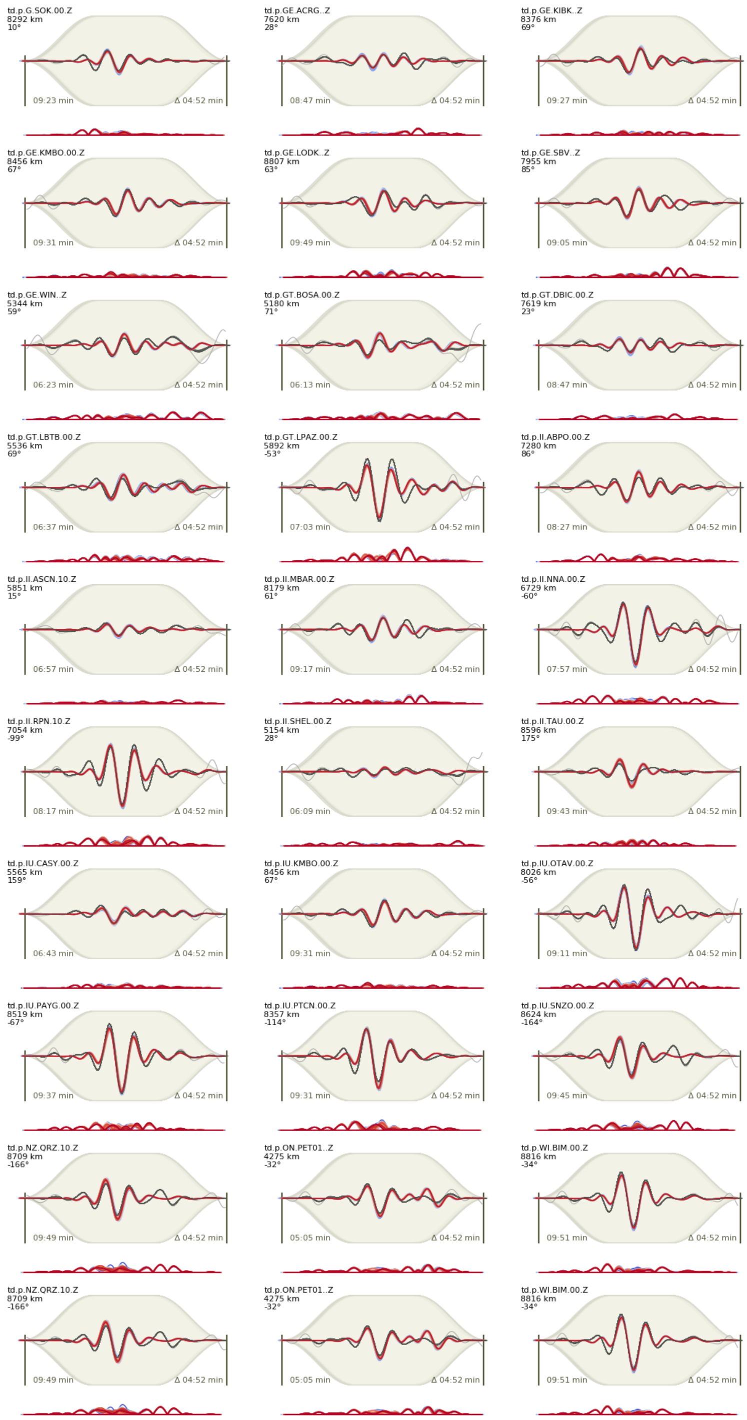

Figure Appendix A.15. Waveform fits of the vertical component retrieved from the CMT inversion for subevent D (part 2), bandpass filtered (0.01–0.03 Hz). Observed traces are black, modelled colored with red indicating smaller misfits vs blue color indicating higher model misfits. Times are given relative to 2021-08-12 18:36:16.

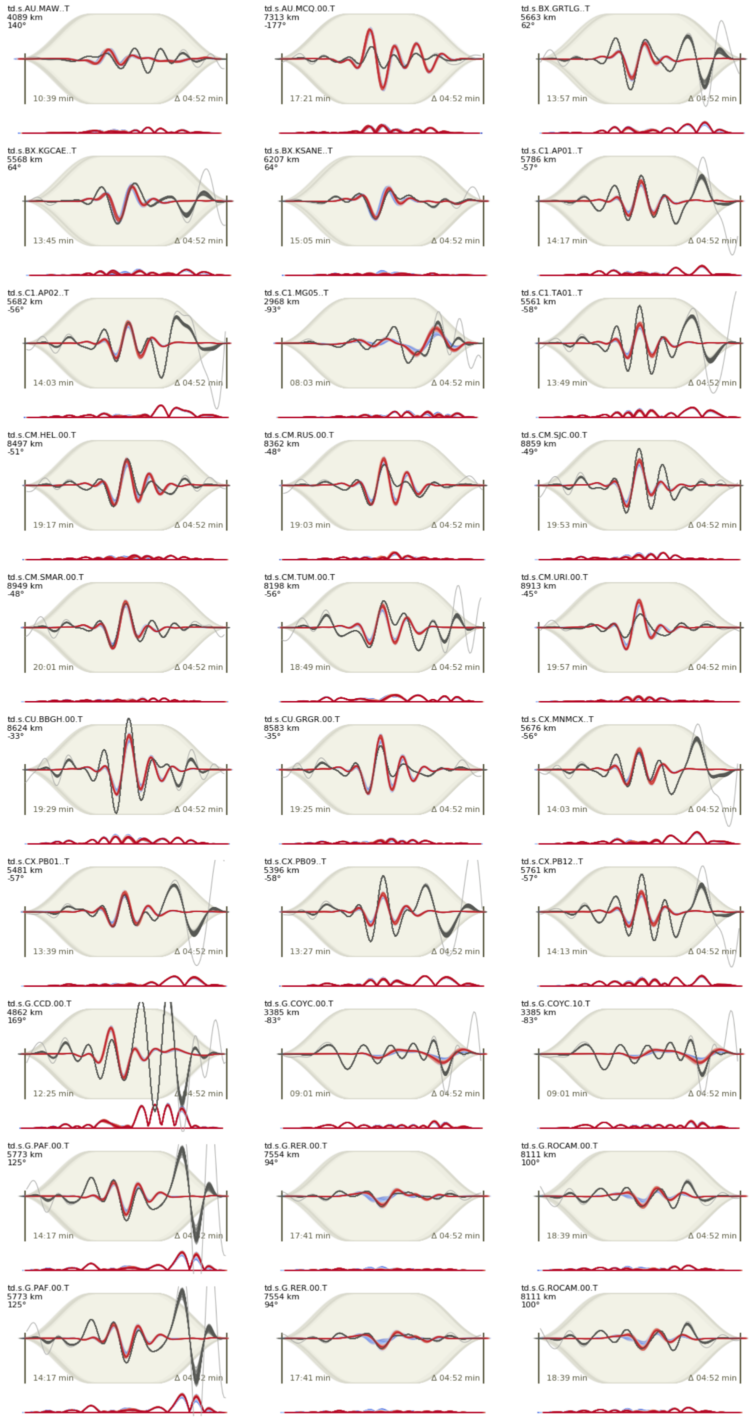

Figure Appendix A.16. Waveform fits of the transverse component retrieved from the CMT inversion for subevent D (part 1), bandpass filtered (0.01–0.03 Hz). Observed traces are black, modelled colored with red indicating smaller misfits vs blue color indicating higher model misfits. Times are given relative to 2021-08-12 18:36:16.

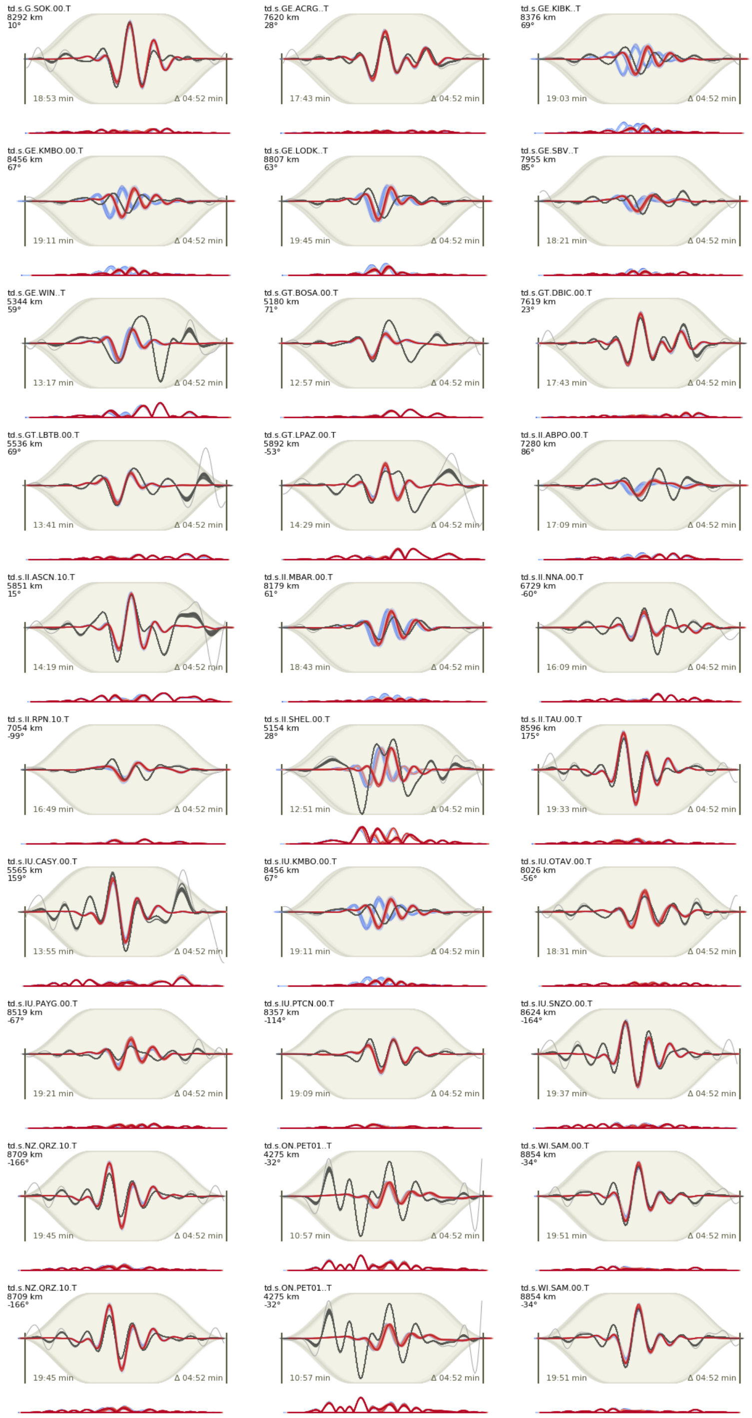

Figure Appendix A.17. Waveform fits of the transverse component retrieved from the CMT inversion for subevent D (part 2), bandpass filtered (0.01–0.03 Hz). Observed traces are black, modelled colored with red indicating smaller misfits vs blue color indicating higher model misfits. Times are given relative to 2021-08-12 18:36:16.

Appendix B Centroid moment tensor inversion and classification for the aftershock sequence

The centroid deviatoric moment tensor (MT) inversions for 88 out of 202 earthquakes with $M_w \geq 5.0$ are performed with Grond (Heimann et al., 2018) (check Appendix A for details on Grond) using specific distance-dependent time windows starting before the theoretical P-wave arrival covering the whole waveform (body and surface waves) on all components. Details on the shape of the time taper windwos are given in Appendix A. The optimizations include seismic data from AI, AW, C1, GE, II, and IU networks. An amplitude correction factor for station ORCD (Cesca et al., 2022) was applied. Synthetic waveforms are computed using a oceanic crust model (Cesca et al., 2022), which is predominant over the considered distance range (200–2500 km). Data is bandpass filtered between 0.02–0.04 Hz yielding highest Signal-to-Noise ratios and fitted over 55,000 iterations. Source parameter uncertainties and confidence intervals are estimated by bootstrapping over data (Heimann et al., 2018), considering 100 different data configurations.

The earthquake classification is performed on the base of the MT catalog, using the seiscloud clustering software (Cesca, 2020). Earthquakes are clustered based on the similarity of their focal mechanisms, using the Kagan angle (Kagan, 1991) as metric. We select the clustering parameters $N_{min} = 2$ and $\epsilon = 0.25$, so that a cluster is formed whenever for a given earthquake there are at least 2 other earthquakes, with a Kagan angle equal or smaller than 30°.

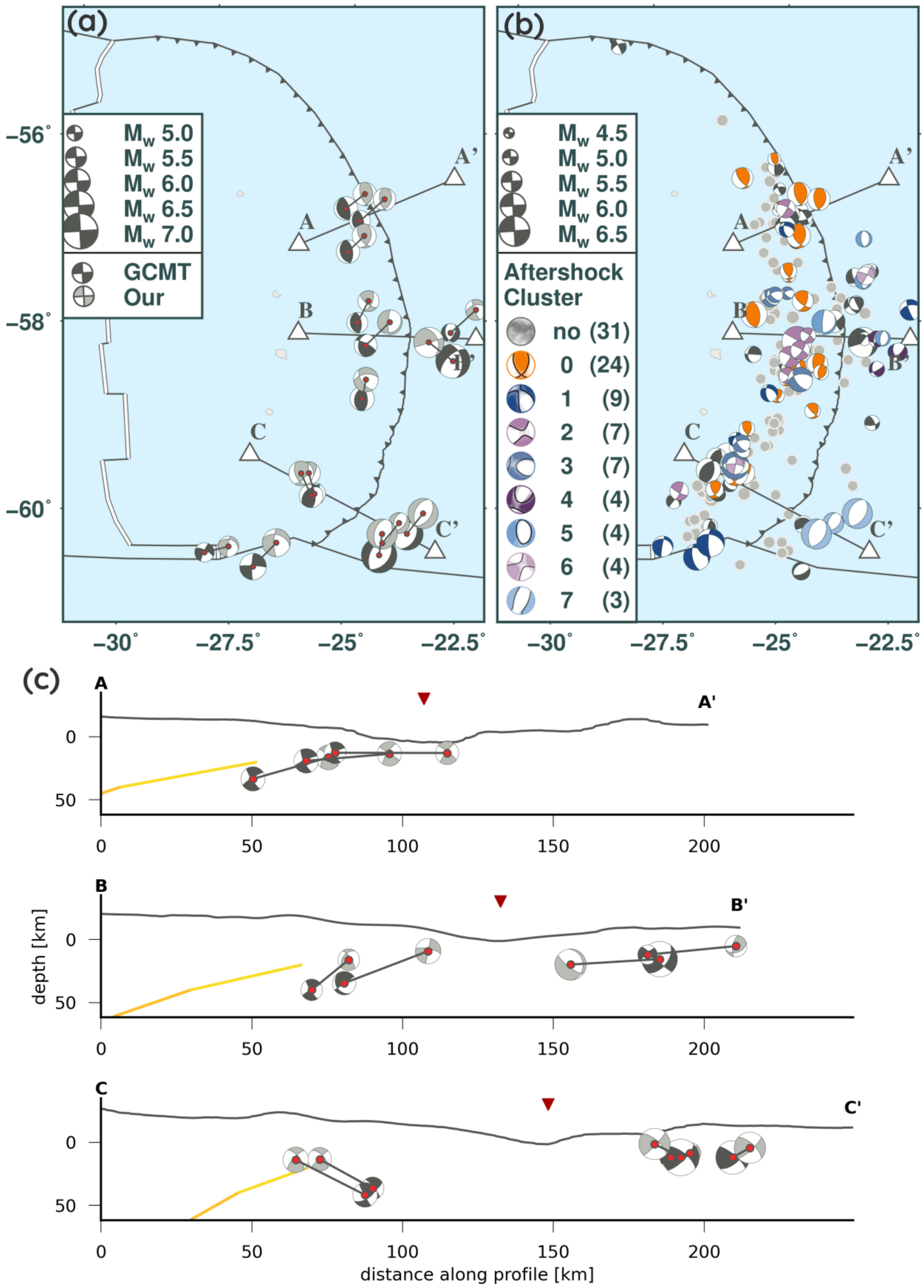

Figure Appendix B.1. Aftershock centroid locations and mechanisms of the aftershocks derived from GCMT (dark grey) compared to our solutions (light grey) as map (a) and cross sectional view (c). Corresponding mechanisms are connected via lines with red dots indicating the shift in location. (b) shows all aftershocks analysed as in Fig. 5a for comparability.

Appendix C Finite fault dynamics from self-similar dynamic extended rupture model

Tabs. Appendix C.2 and Appendix C.3 show all parameters extracted from the PDR inversions. Below waveform fits of the ensemble of solutions are shown as well as histograms for each parameter.

The inversions are also performed with Grond (Heimann et al., 2018) (check Appendix A for details on Grond) using specific distance-dependent time windows. Details on their shape and the settings are given in Appendix A and Appendix C.1. The PDR optimizations for subevents A and D include 63,000 iterations while the joint B and C inversion includes 93,000 due to the larger parameter space. The uncertainties for every resolved parameter are delivered by bootstrapping the data considering 20 different configurations. We consider the mean model.

Table Appendix C.1. Choosen dynamic time windows for the PDR inversions. Corner times of the used cosine taper are defined as $t_{min}, t_{min} + t_{taper}, t_{max} - t_{taper}, t_{max}$ with respect to the inverted event origin time*

Inversion	A_{PDR}	B_{PDR}+C_{PDR}	D_{PDR}
P-wave/W-Phase time window relative to t_P			
t_{min} [s]	-130 (100)	-	-130 (100)
t_{max} [s]	+300 (100)	-	+160 (100)
S-wave time window relative to t_S			
t_{min}	-160 (100)	-	-130 (100)
t_{max}	+300 (100)	-	+160 (100)
Full waveform time window relative to t_P			
t_{min}	-	-1000 (1000)	-
t_{max}	-	$v_{surf}(3.5)^{\dagger}$ + 1000 (1000)	-

t_P - P wave arrival time using AK135

t_S - S wave arrival time using AK135

* - Format: <time> (taper)

† - $v_{surf}(XX)$ Indicating surface wave arrival with velocity of XX km/s

Table Appendix C.2. PDR mean inversion results for the subevents A and D

Event	A	D
Latitude [°±km]	-57.637±18	-59.92±17
Longitude [°±km]	-24.527±18	-25.898±20
Origin time [s]	18:32:54±2	18:36:01±2
Depth [km]	10±5	23±4
Length [km]	149±32	58±11
Width [km]	42±7	48±8
Strike [°]	147±16	219±9
Dip [°]	21±5	20±2
Rake [°]	80±11	128±8
v_r/v_s	0.40±0.08	0.49±0.08
Max. slip [m]	2.3±0.5	3.1±0.5
Nucleation x	-0.6±0.3	-0.3±0.2
Nucleation y	-0.2±0.4	-0.4±0.4

Coordinates refer to the top edge center. Nucleation point coordinates are given in relative coordinates ranging from -1 (left/top edge) to 1 (right/bottom edge) for x (along strike) and y (down dip).

Table Appendix C.3. PDR mean results of the joint inversion for the subevents B and C

Event	B	C
Centroid (relative to subfault top edges)		
Latitude [°±km]	-59.288±53	
Longitude [°±km]	-23.987±28	
Time [s]	18:34:12±19	
Depth [km]	10±4	
Relative fault parameter		
Δ time [s]†	151±13	
Δ depth [km]†	0±3	
Azimuth [°]†	184±14	
Distance [km]†	202±71	
$M_{0,subevent}/\sum M_0$	0.59±0.13	0.41±0.13
Fault plane		
Length [km]	270±56	178±48
Width [km]	34±10	49±14
Strike [°]	172±8	218±9
Dip [°]	29±13	39±9
Rake [°]	96±16	111±13
v_r/v_s	0.33±0.08	0.37±0.08
Max. slip [m]	5.8±2.2	5.0±1.7
Nucleation x*	-0.5±0.4	-0.2±0.5
Nucleation y*	-0.1±0.6	-0.1±0.6

† - From subevent B to C

* - Explanation of coordinates given in Tab. Appendix C.2

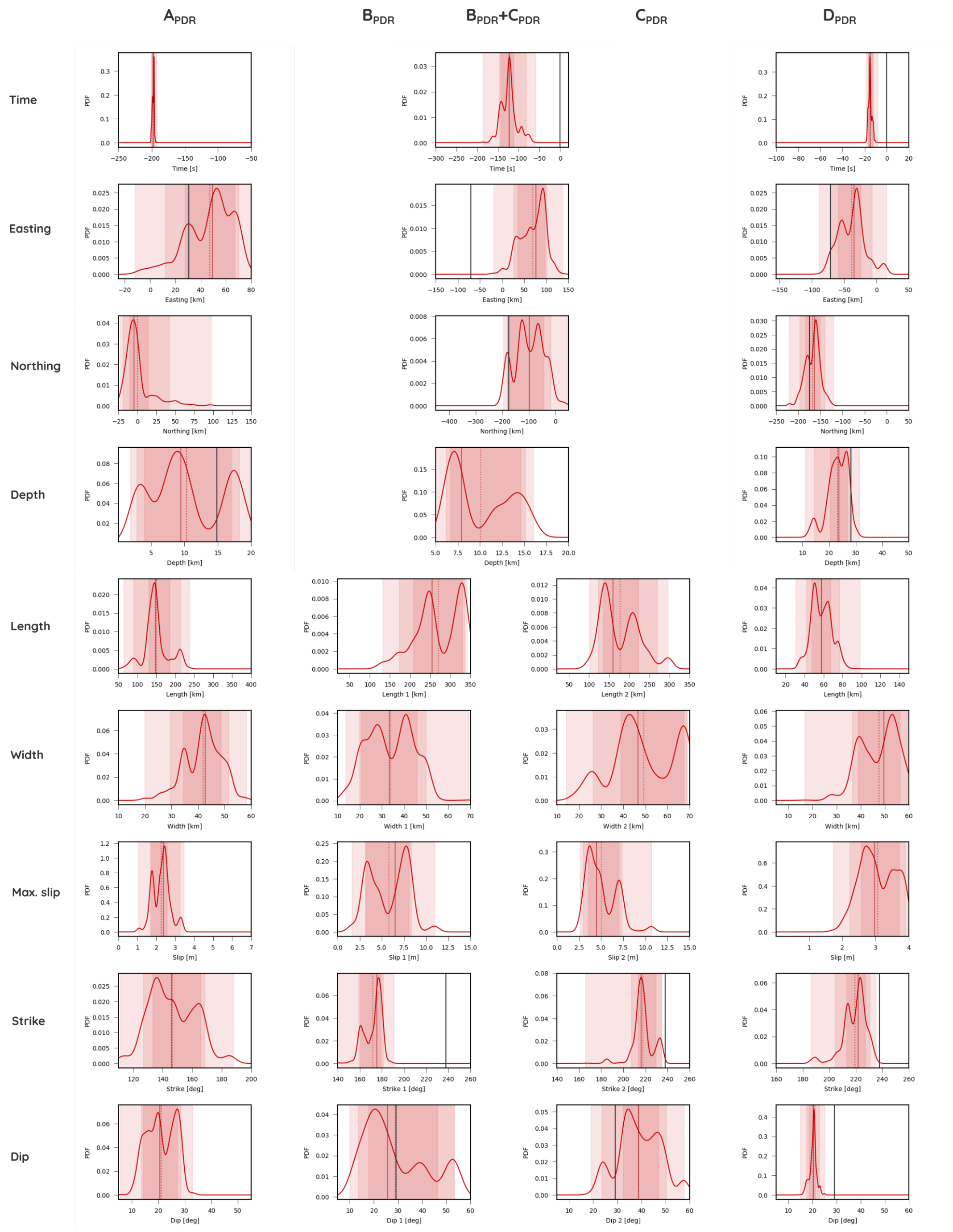

Figure Appendix C.1. Parameter distribution of the tested models for all PDR inversions (part 1). Parameters time, easting, northing and depth in column $B_{PDR} + C_{PDR}$ indicate the uncertainties on the location and time of the joint centroid of B and C.

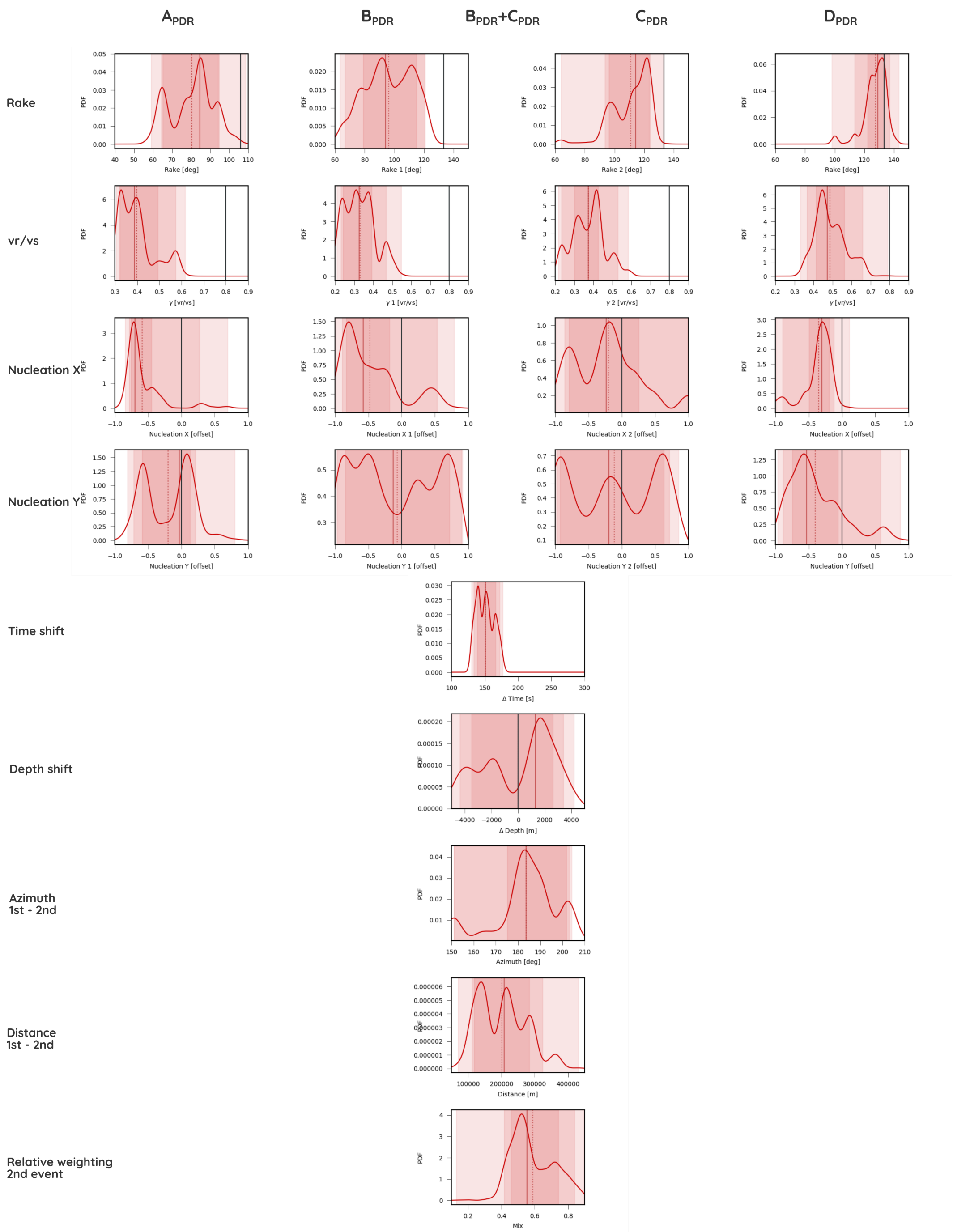

Figure Appendix C.2. Parameter distribution of the tested models for all PDR inversions (part 2). The parameters time shift, depth shift, azimuth, distance and relative weighting in column $B_{PDR} + C_{PDR}$ indicate the uncertainties on the relative fault location and time of B and C with respect to their joint centroid location.

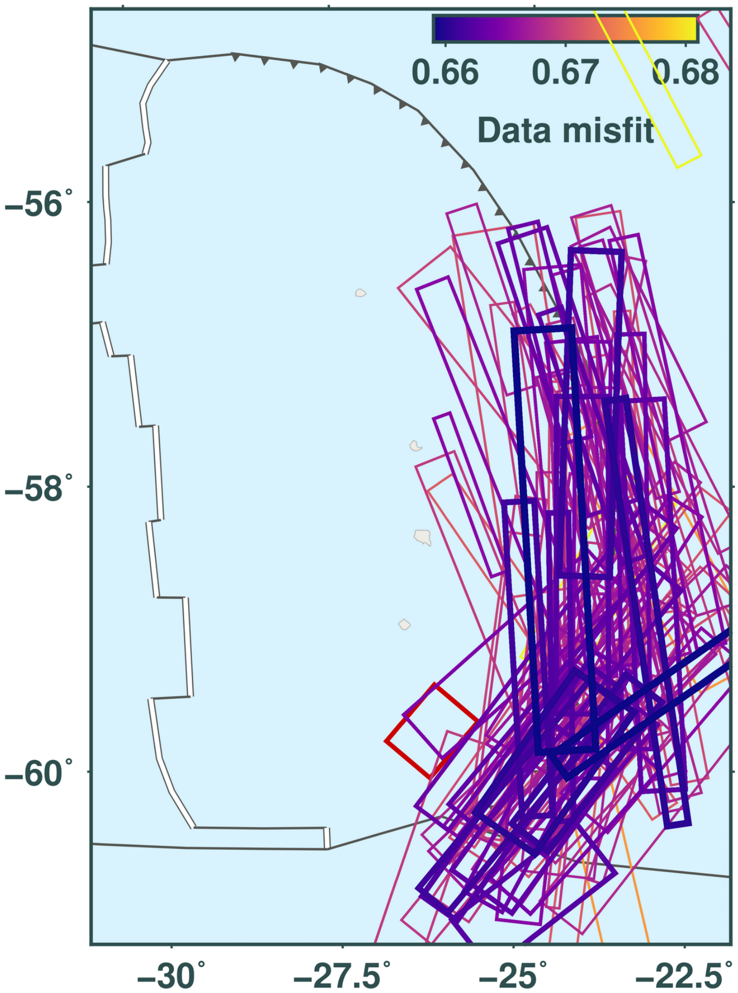

Figure Appendix C.3. Location of the PDR rupture planes of subevents B and C derived from the 1,000 best models of inversion compared to the location of the PDR rupture plane of subevent D (red). Both color and line width scale with the associated misfit of each model.

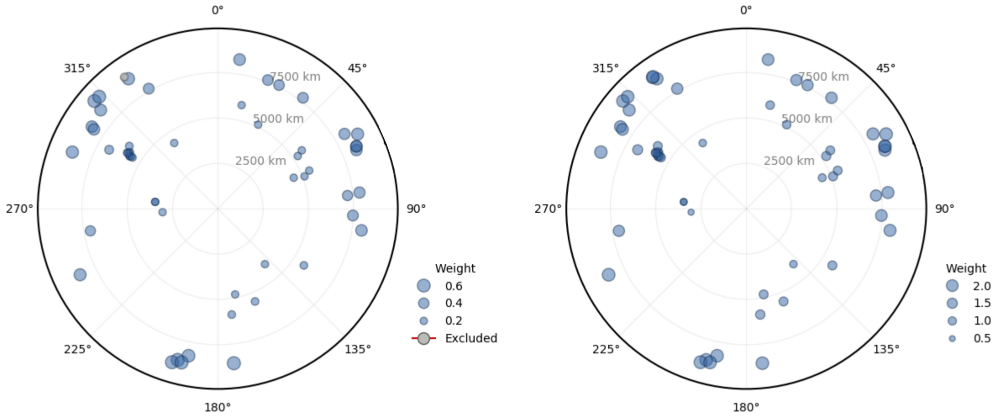

Figure Appendix C.4. PDR for event A - azimuthal distribution and weights for the transverse component (left) and the vertical components (right).

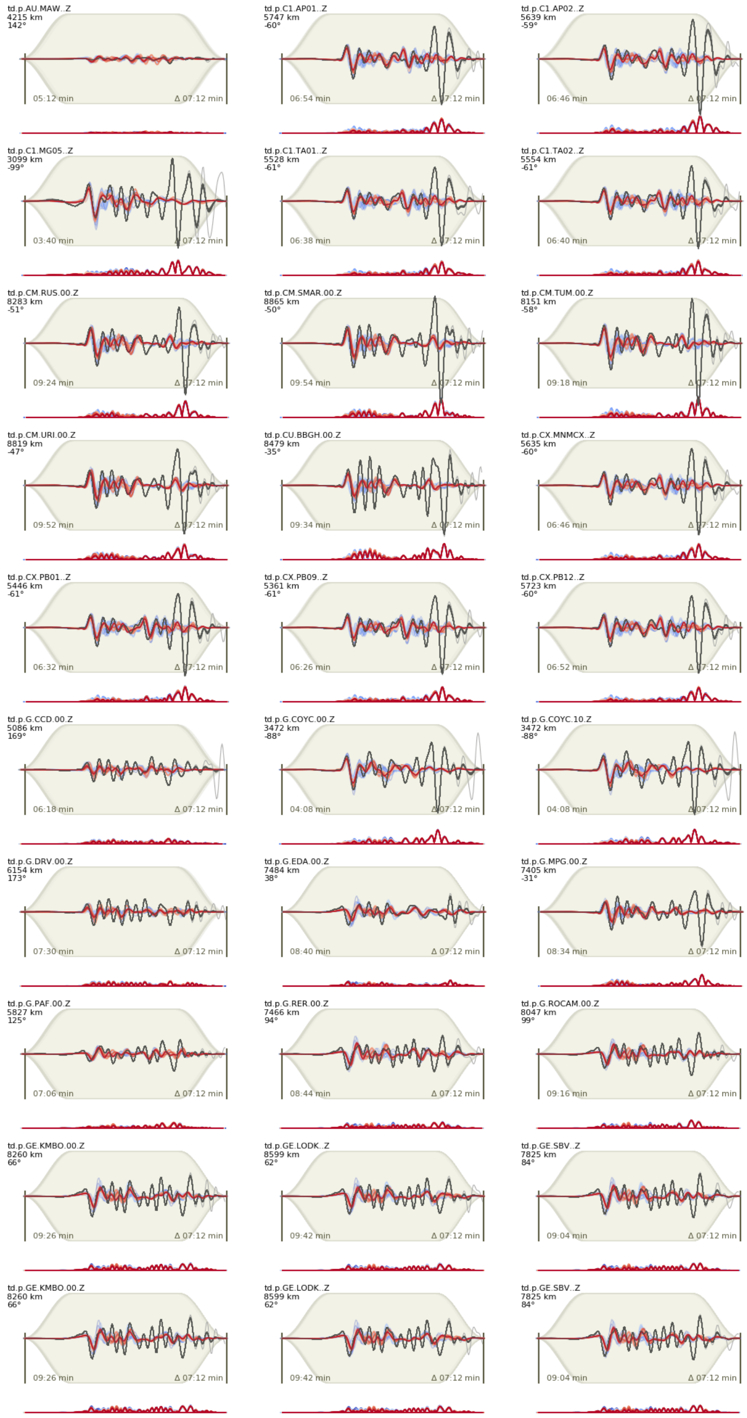

Figure Appendix C.5. Waveform fits of the vertical component retrieved from the PDR inversion for subevent A (part 1), bandpass filtered (0.01–0.05 Hz). Observed traces are black, modelled colored with red indicating smaller misfits vs blue color indicating higher model misfits. Times are given relative to 2021-08-12 18:32:54.

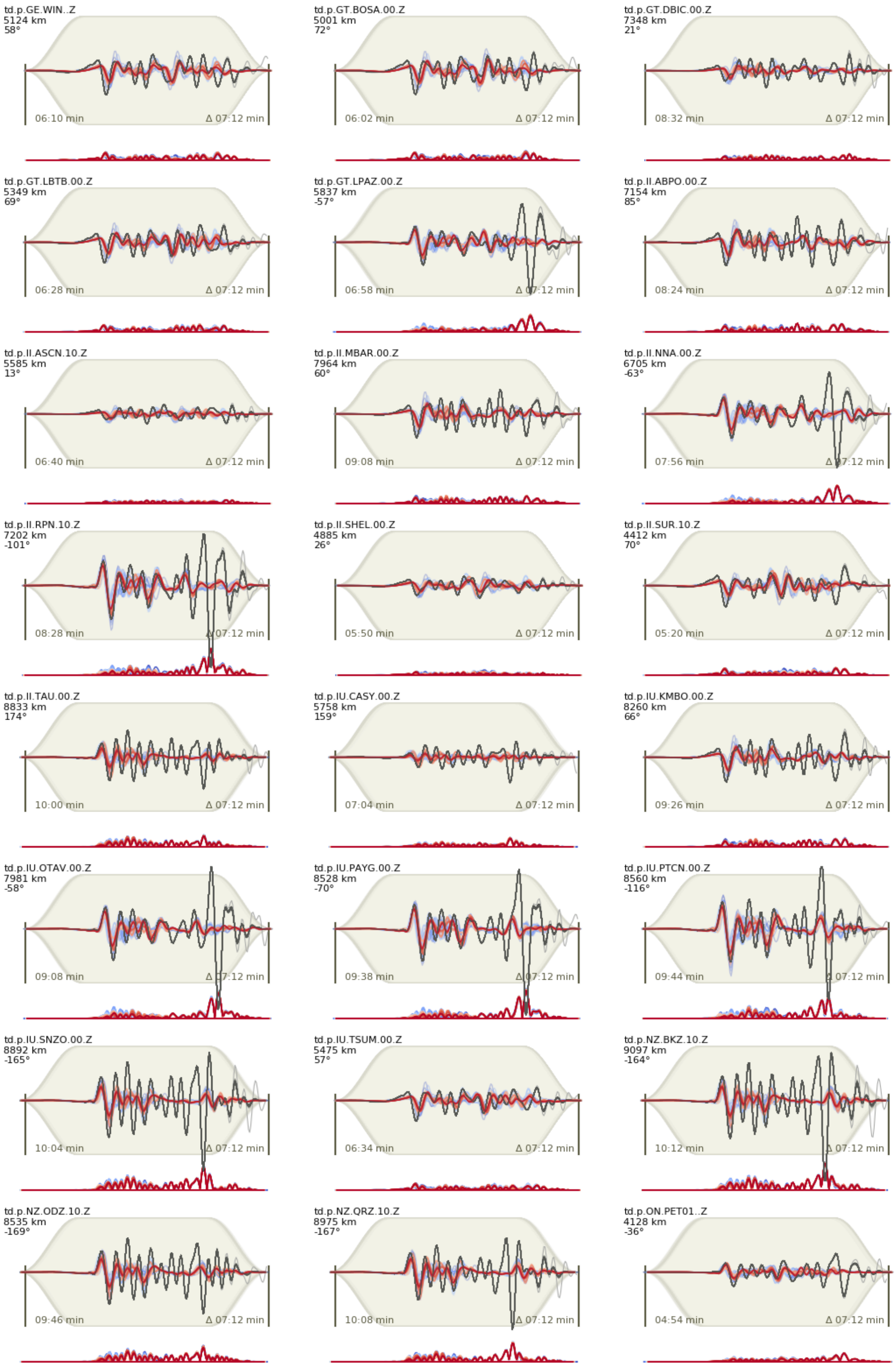

Figure Appendix C.6. Waveform fits of the vertical component retrieved from the PDR inversion for subevent A (part 2), bandpass filtered (0.01–0.05 Hz). Observed traces are black, modelled colored with red indicating smaller misfits vs blue color indicating higher model misfits. Times are given relative to 2021-08-12 18:32:54.

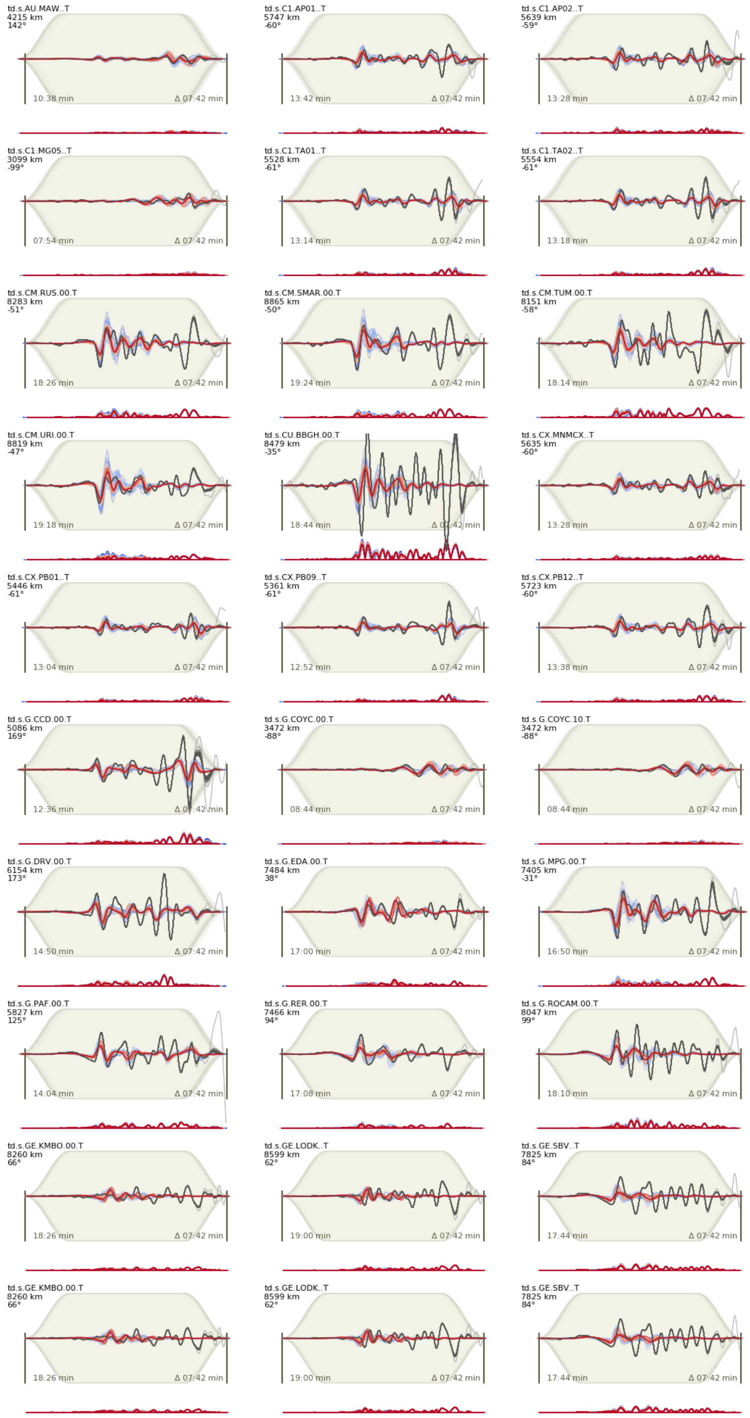

Figure Appendix C.7. Waveform fits of the transverse component retrieved from the PDR inversion for subevent A (part 1), bandpass filtered (0.01–0.05 Hz). Observed traces are black, modelled colored with red indicating smaller misfits vs blue color indicating higher model misfits. Times are given relative to 2021-08-12 18:32:54.

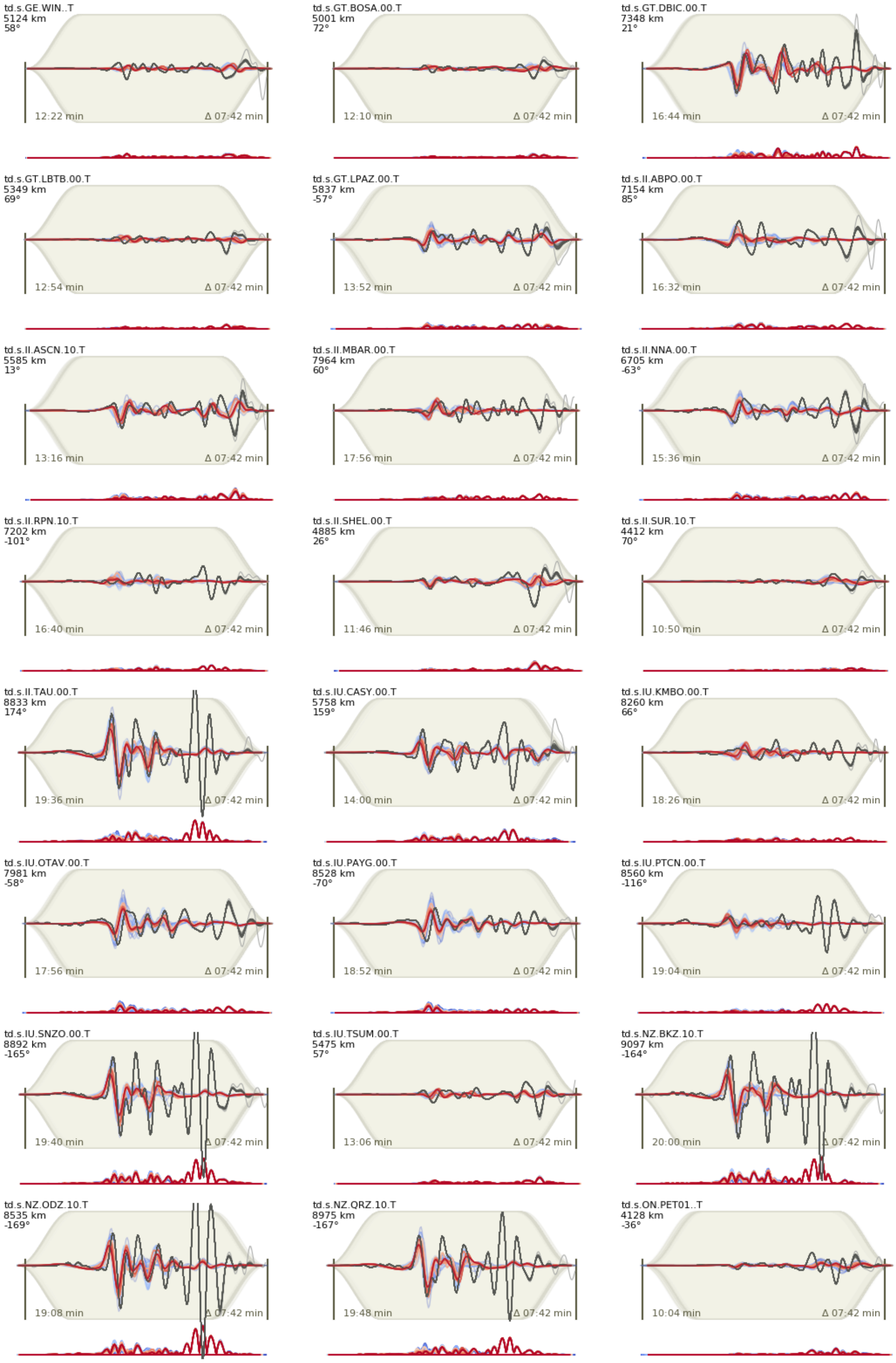

Figure Appendix C.8. Waveform fits of the transverse component retrieved from the PDR inversion for subevent A (part 2), bandpass filtered (0.01–0.05 Hz). Observed traces are black, modelled colored with red indicating smaller misfits vs blue color indicating higher model misfits. Times are given relative to 2021-08-12 18:32:54.

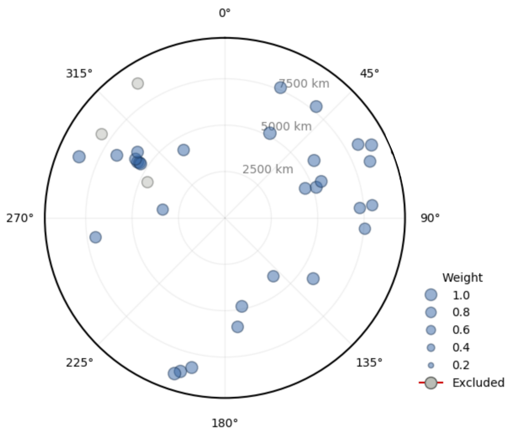

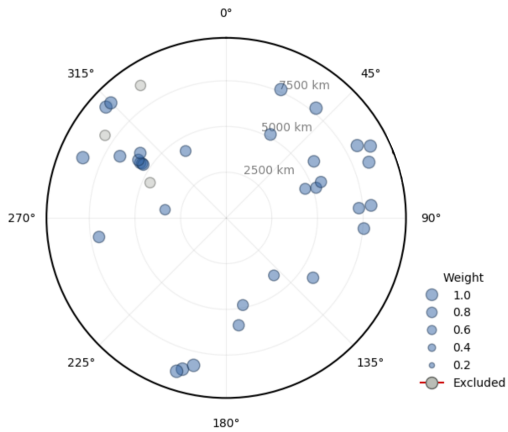

Figure Appendix C.9. PDR for event B and C - azimuthal distribution and weights for the radial component (left) and the vertical components (right).

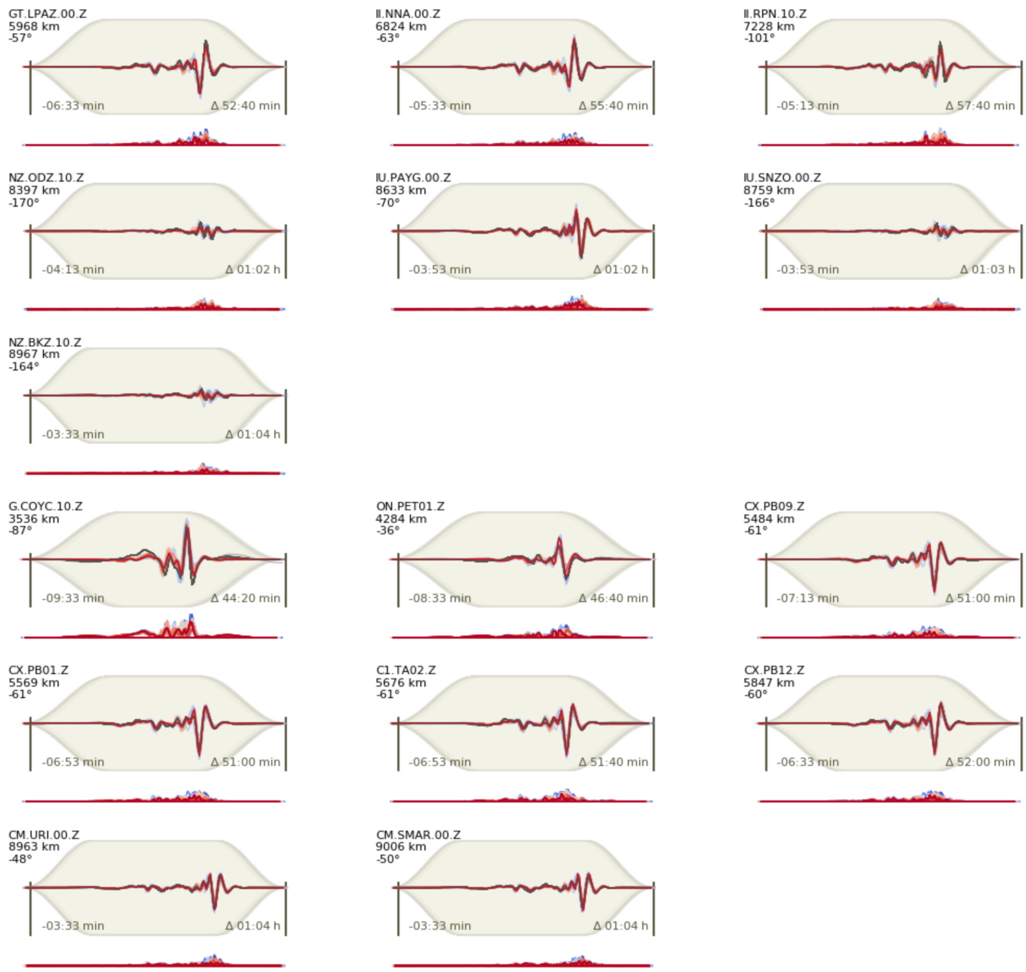

Figure Appendix C.10. Waveform fits of the vertical component retrieved from the PDR inversion for subevent B and C (part 1), bandpass filtered (0.001–0.01 Hz). Observed traces are black, modelled colored with red indicating smaller misfits vs blue color indicating higher model misfits. Times are given relative to 2021-08-12 18:34:12.

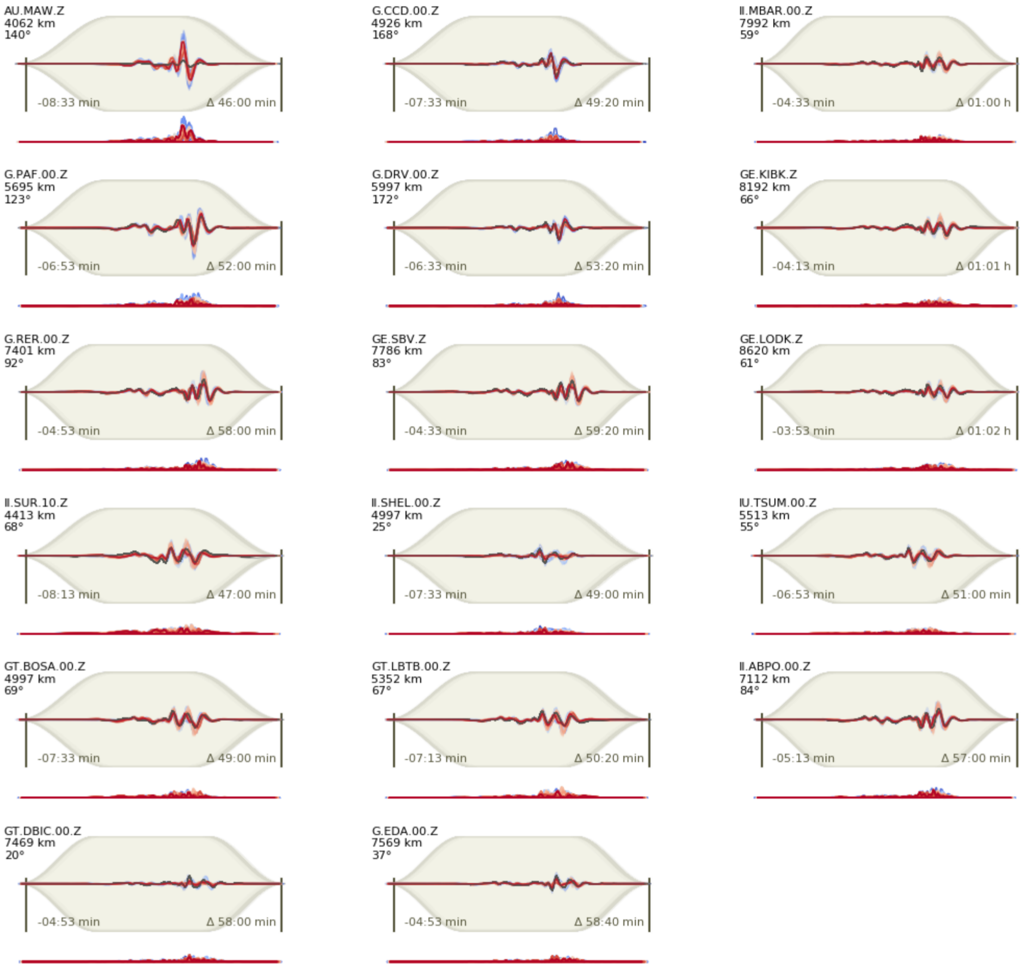

Figure Appendix C.11. Waveform fits of the vertical component retrieved from the PDR inversion for subevent B and C (part 2), bandpass filtered (0.001–0.01 Hz). Observed traces are black, modelled colored with red indicating smaller misfits vs blue color indicating higher model misfits. Times are given relative to 2021-08-12 18:34:12.

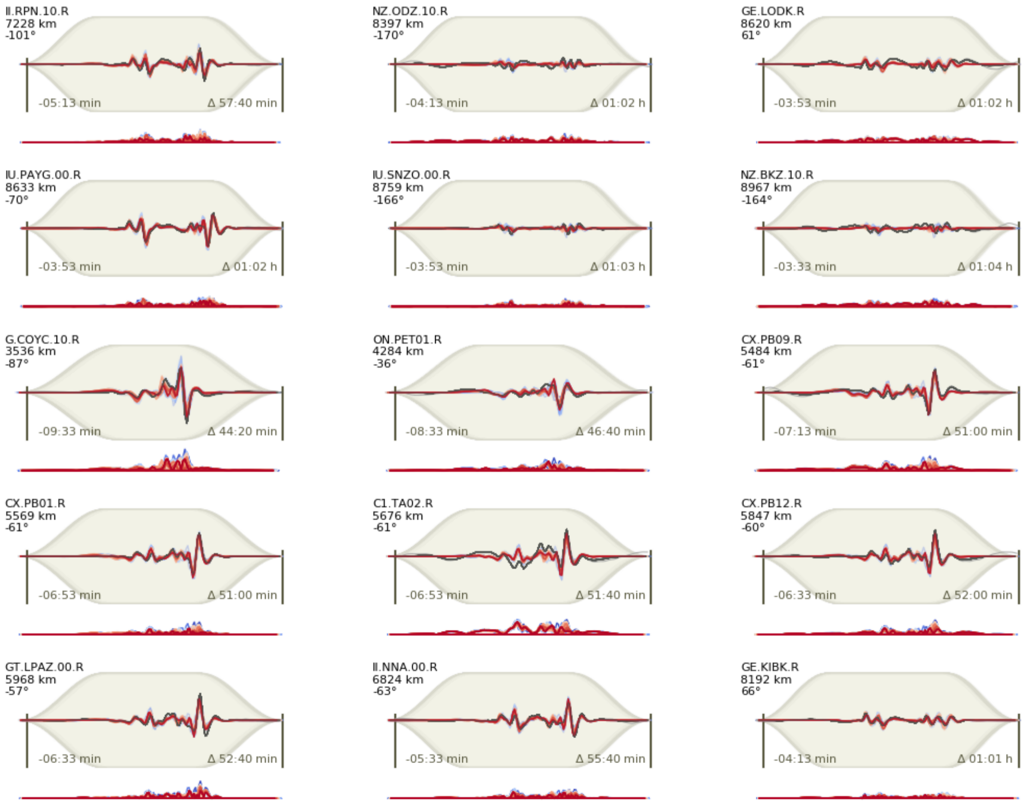

Figure Appendix C.12. Waveform fits of the radial component retrieved from the PDR inversion for subevent B and C (part 1), bandpass filtered (0.001–0.01 Hz). Observed traces are black, modelled colored with red indicating smaller misfits vs blue color indicating higher model misfits. Times are given relative to 2021-08-12 18:34:12.

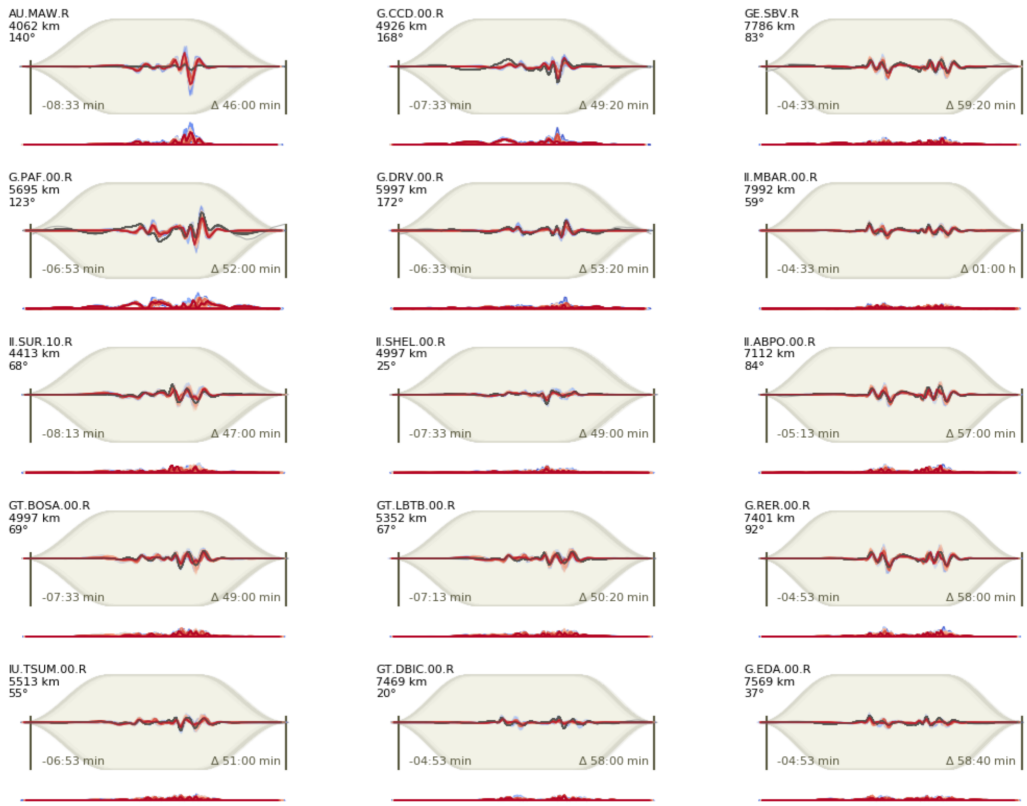

Figure Appendix C.13. Waveform fits of the radial component retrieved from the PDR inversion for subevent B and C (part 2), bandpass filtered (0.001–0.01 Hz). Observed traces are black, modelled colored with red indicating smaller misfits vs blue color indicating higher model misfits. Times are given relative to 2021-08-12 18:34:12.

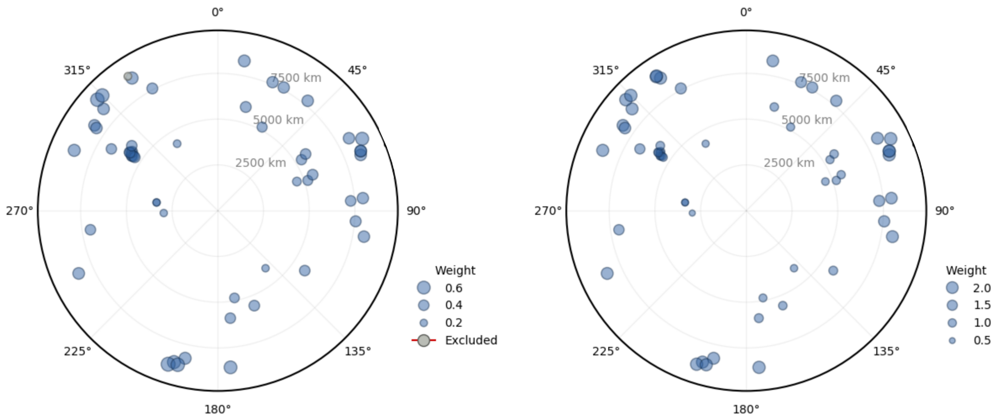

Figure Appendix C.14. PDR for event D - azimuthal distribution and weights for the transverse component (left) and the vertical components (right).

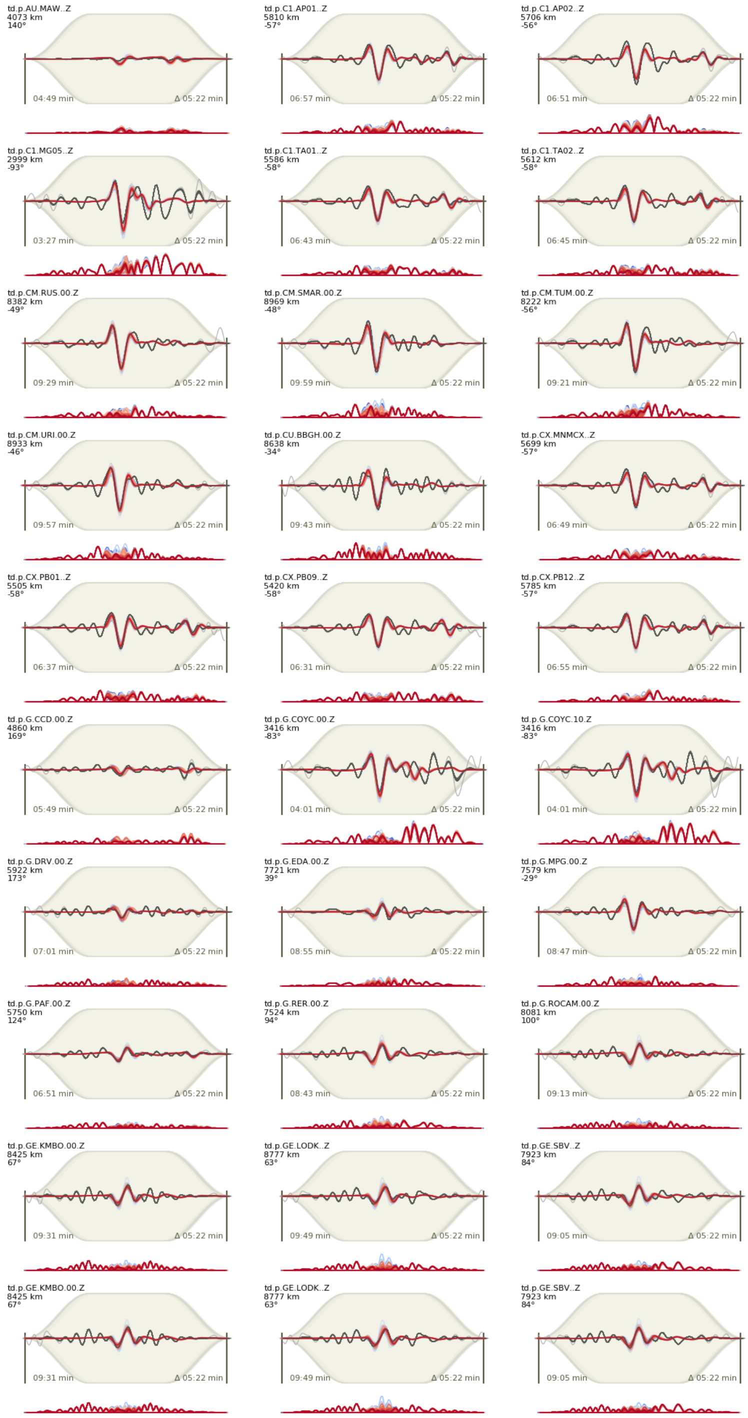

Figure Appendix C.15. Waveform fits of the vertical component retrieved from the PDR inversion for subevent D (part 1), bandpass filtered (0.01–0.05 Hz). Observed traces are black, modelled colored with red indicating smaller misfits vs blue color indicating higher model misfits. Times are given relative to 2021-08-12 18:36:01.

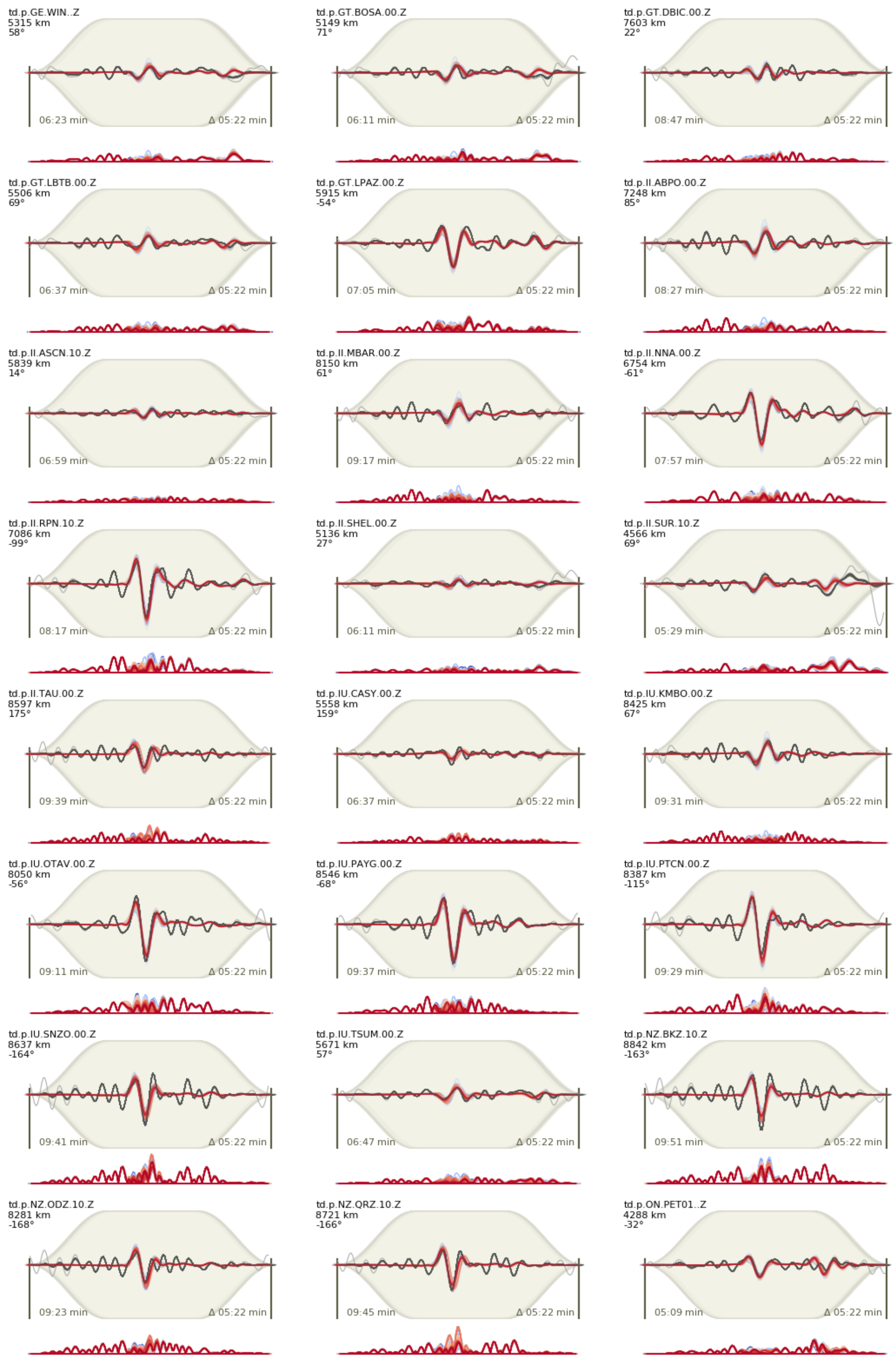

Figure Appendix C.16. Waveform fits of the vertical component retrieved from the PDR inversion for subevent D (part 2), bandpass filtered (0.01–0.05 Hz). Observed traces are black, modelled colored with red indicating smaller misfits vs blue color indicating higher model misfits. Times are given relative to 2021-08-12 18:36:01.

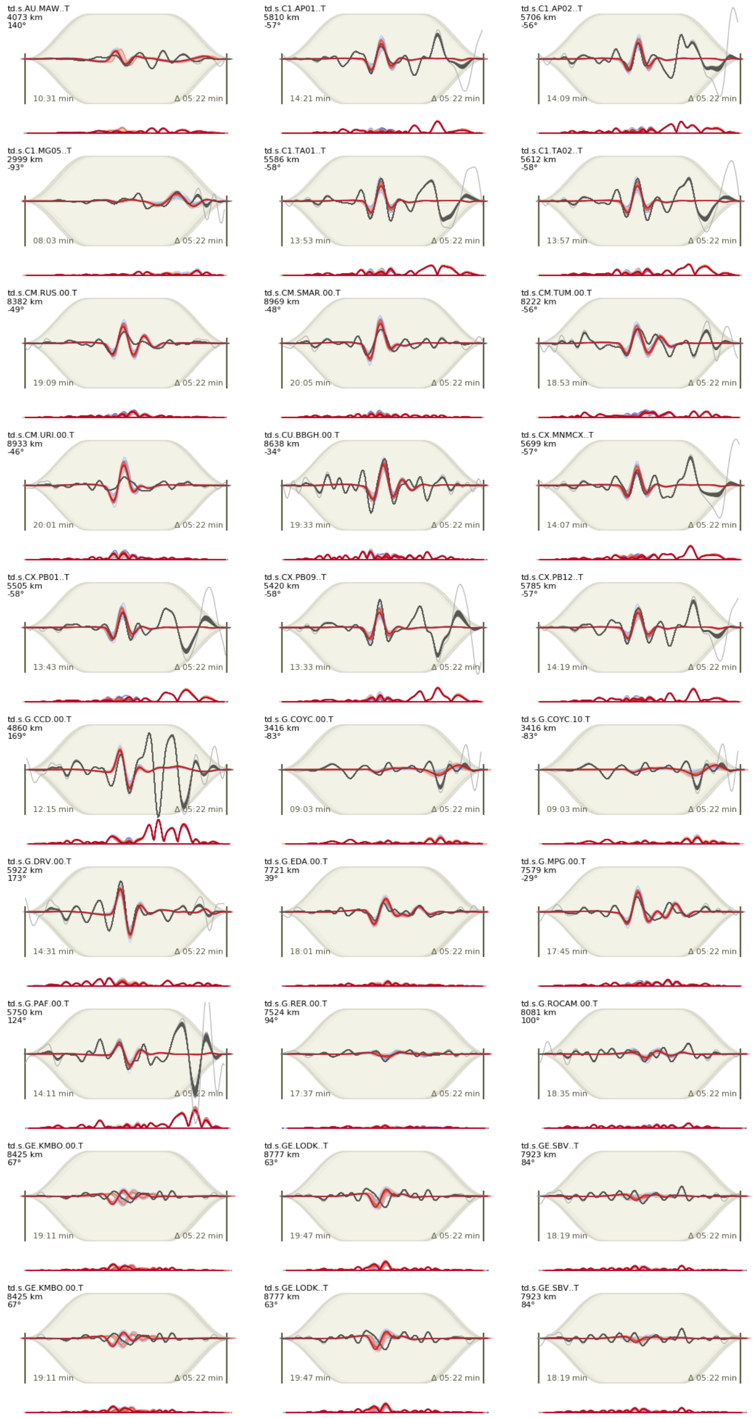

Figure Appendix C.17. Waveform fits of the transverse component retrieved from the PDR inversion for subevent D (part 1), bandpass filtered (0.01–0.05 Hz). Observed traces are black, modelled colored with red indicating smaller misfits vs blue color indicating higher model misfits. Times are given relative to 2021-08-12 18:36:01.

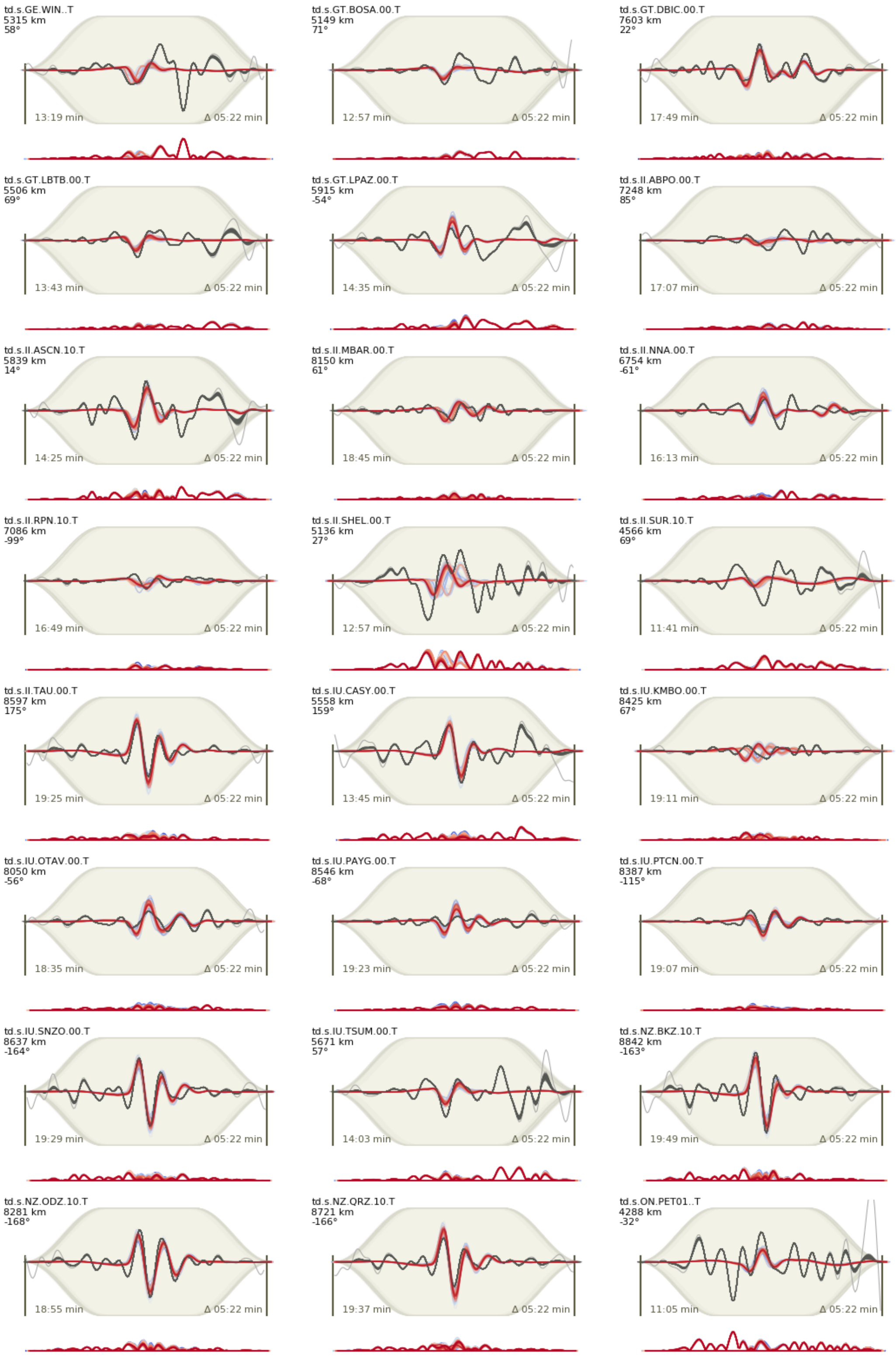

Figure Appendix C.18. Waveform fits of the transverse component retrieved from the PDR inversion for subevent D (part 2), bandpass filtered (0.01–0.05 Hz). Observed traces are black, modelled colored with red indicating smaller misfits vs blue color indicating higher model misfits. Times are given relative to 2021-08-12 18:36:01.

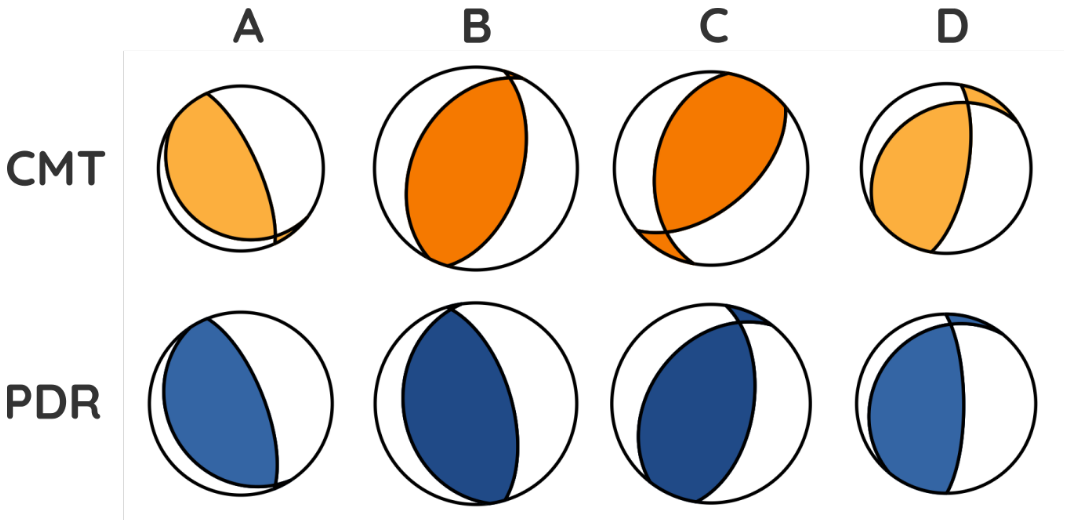

Figure Appendix C.19. Comparison of focal mechanisms derived from CMT inversions (top row) and PDR inversions (bottom row) for the given subevents A (left) to D (right). Size scales with magnitude. Colors are the same as in Fig. 3.

Appendix D Teleseismic Back-projection

We image the 2021 South Sandwich earthquake rupture from the back-projection of short-period P waves (0.5-2.0 Hz). We used the multi-array back-projection method of Vera et al. (2021), which includes semi-automatic estimates of earthquake rupture parameters, i.e., length, directivity, speed, and aspect ratio. The method combines semblance and beam energy maps from several ad-hoc seismic arrays, which are automatically weighted based on their azimuthal distribution. Semblance measures the coherence of waveforms. Semblance maxima of each analyzed short time window over time track the rupture front, while the time evolution of the energy maxima characterizes the relative strength of short-period energy emissions, providing a proxy for a band-limited source time function (e.g., Neidell & Taner, 1971; Rössler et al., 2010; Palo et al., 2014). We back-projected vertical broad band P waveform vertical component seismograms bandpass filtered at 0.5–2.0 Hz, analyzed with overlapping 6 s time windows in steps of 1 s. We processed data from four regions (Chile, Caribbean, Australia, and Southern Africa). The IASP91 velocity model of Kennett and Engdahl (1991) was used to predict P-wave arrival times. We additionally corrected theoretical arrival times with receiver-dependent time shifts derived from the aftershock-based calibration method of Palo et al. (2014). The calibration reduces the effect of 3D Earth heterogeneities on arrival times, especially for back-projection of large earthquake ruptures (e.g., Ishii et al., 2007; Palo et al., 2014; Meng et al., 2016). Here, eight events (Table Appendix D.1) with thrust focal mechanisms spanned the rupture extent and provided the time shifts. Fig. Appendix D.1b shows the azimuthal distribution of the arrays used and the first 10 s of the waveform coherence after calibration (first 300 s in Fig. Appendix D.2). The effectiveness of the calibration is presented in Fig. Appendix D.3. The back-projection showed location errors of ∼30 km on average. The location error at two sides of the megathrust showed to be reasonably resolved, i.e., up to ∼23 km on average, except in the central part where the second calibration event induced an abrupt SE offset of ∼72 km (event-2; Fig. Appendix D.3). The location errors were found to be suitably scaled by the large rupture of the Sandwich Island earthquake, making the back-projection also appropriate for imaging the short-period earthquake rupture propagation. The P waves were back-projected into a horizontal grid with points spaced 5 km apart at a constant depth of 13 km. We utilized a constant depth grid rather than following the slab because we considered the possibility of activation of the transform fault of the rupture. As only minor travel time differences arise for P waves for the likely depth variation and move-outs are nearly identical, the only difference with respect to a back-projection using a grid following a dipping slab could be a wrong timing of semblance maxima by at most 2-3 s, insignificant for the overall evolution of the rupture.

Table Appendix D.1. Earthquake source parameters for events used in the back-projection calibration. Aftershock parameters were obtained from the GEOFON Moment tensor solution catalog.

N°	Time (UTC)	Mw	Lon (deg)	Lat (deg)	Depth (km)	Strike	Dip	Rake
1	2021-08-12 18:32:49.38	7.7	-25.33	-57.62	13	159°	11°	84°
2	2021-08-12 18:35:22.30	8.0	-25.21	-58.42	11	207°	11°	86°
3	2021-08-13 11:45:35.19	5.8	-25.62	-57.24	25	161°	22°	89°
4	2021-08-16 05:46:18.76	5.8	-25.73	-56.88	19	162°	20°	94°
5	2021-08-17 17:53:29.27	6.1	-25.57	-58.00	35	166°	36°	85°
6	2021-08-18 02:48:53.78	5.8	-26.36	-59.73	40	193°	47°	80°
7	2021-08-18 21:49:53.96	5.9	-26.40	-59.71	43	225°	44°	117°
8	2021-09-06 08:19:43.94	5.9	-25.33	-58.87	29	182°	30°	88°

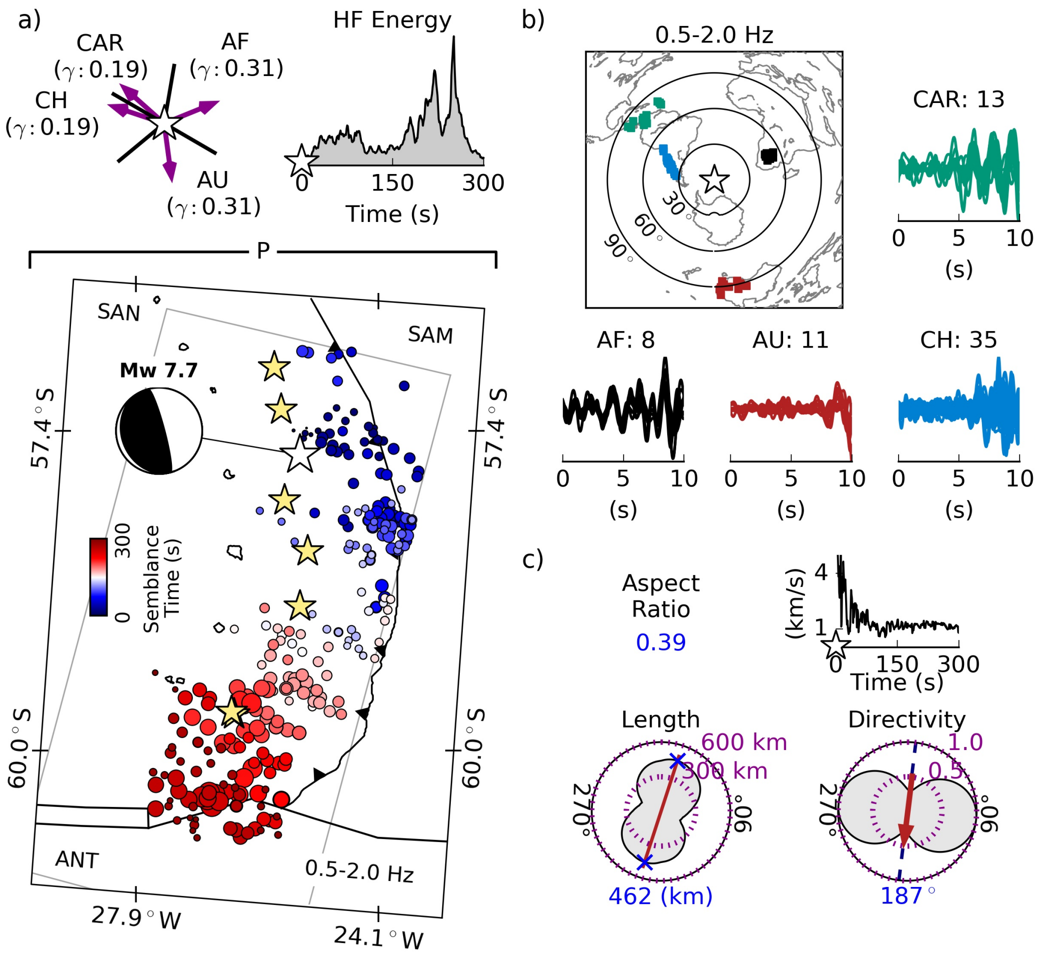

Figure Appendix D.1. The 2021 South of Sandwich Islands earthquake back-projection (0.5–2.0 Hz). a) Back-projected earthquake rupture. Blue-red dots show the rupture propagation based on semblance maxima scaled by energy radiated. The yellow stars indicate the events used in the aftershock-based calibration method, including the first Mw 7.7 event (white star). Tectonic setting: South American (SAM), Sandwich (SAN), and Antarctic (ANT) plates. Inset: Array weights and short-period energy radiated source time function. b) Multi-array configuration and calibrated P waveforms. c) Rupture parameter derived from the multi-array back-projection method. Rupture directivity, length, aspect ratio, and velocity from the spatiotemporal evolution of short-period emission points relative to the epicenter. For estimating rupture length, the emission points are projected on lines passing through the epicenter for all azimuths; the maximization provides the rupture length. The aspect ratio is defined by the quotient between the minimum and maximum length estimates. For the rupture directivity, minimizing the sum of the squares of the perpendicular distances of all emission points to the azimuths control the estimation. The rupture speed time series depends on the distance and time of the emission points relative to the event epicenter. See details for rupture parameter estimates in Vera et al. (2021).

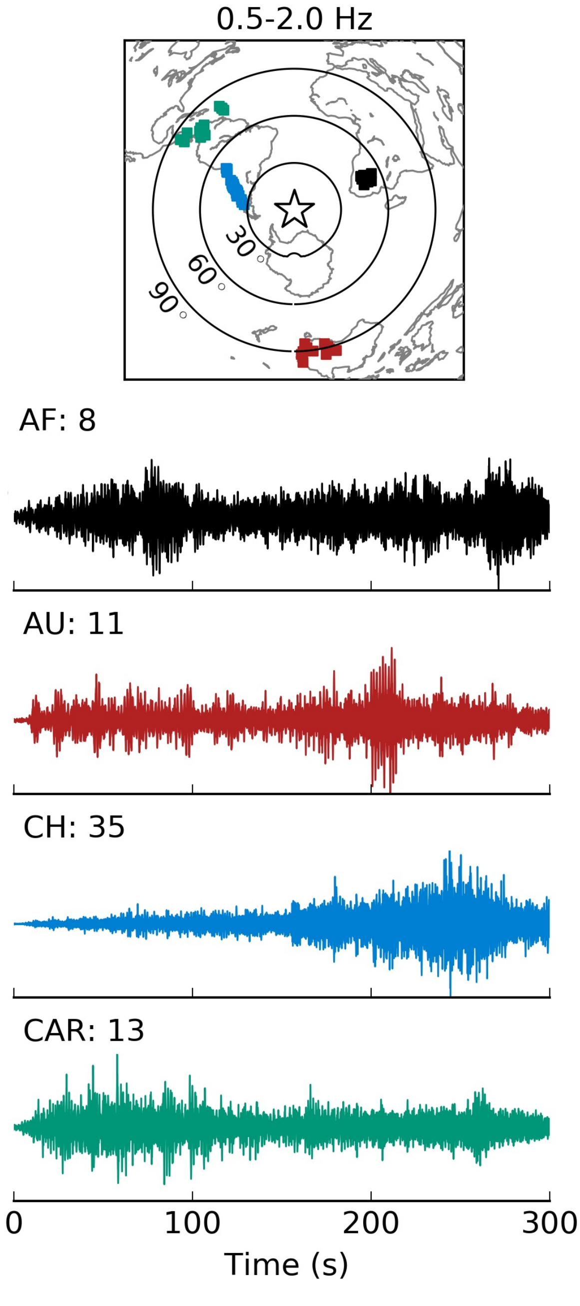

Figure Appendix D.2. High-frequency waveforms (0.5–2.0 Hz) from back-projected seismic arrays: AF, AU, CH, and CAR. Time (s) relative to theoretical P-wave arrivals from the mainshock hypocenter.

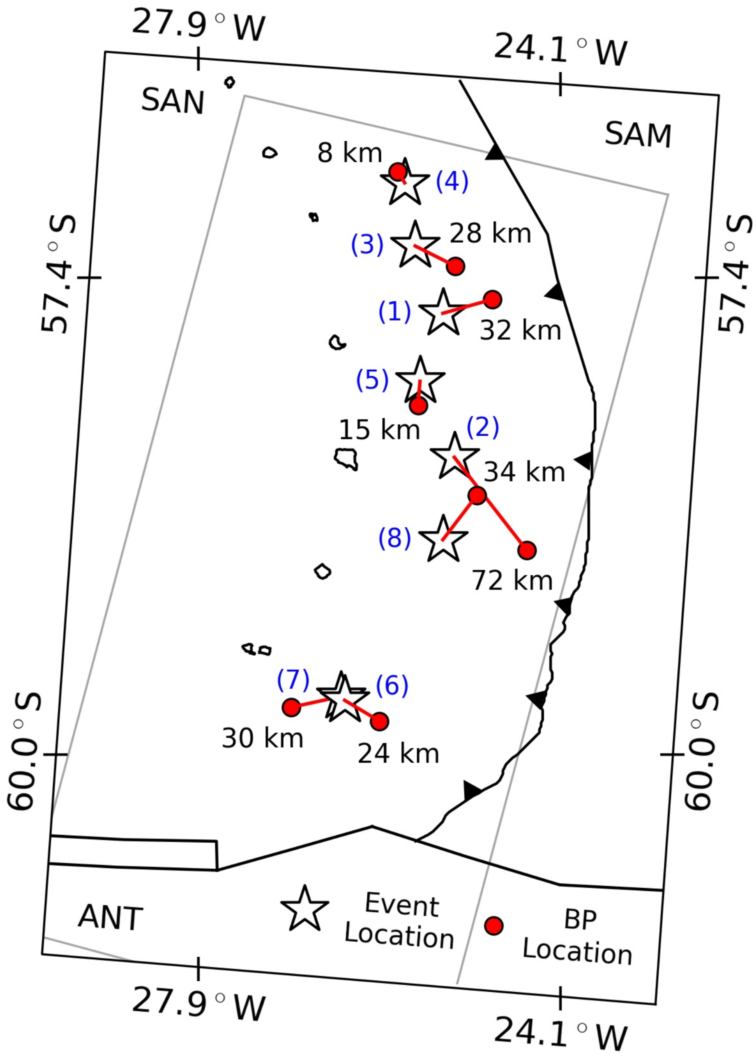

Figure Appendix D.3. Events included in the back-projection calibration (white stars) and recovered locations (red circles). Location errors are expressed in km and labeled next to each event. The numbers labeled in blue designate the events ID presented in Table Appendix D.1. Tectonic setting: South American (SAM), Sandwich (SAN), and Antarctic (ANT) plates.

Appendix E Data and Resources

We used waveform data from the following seismic networks: AF (Penn State University, 2004), AI (Istituto Nazionale di Oceanografia e di Geofisica Sperimentale, 1992), AU (Geoscience Australia (GA), 1994), AW (Alfred Wegener Institute For Polar And Marine Research (AWI), 1993), BL (Universidade de Sao Paulo (USP), 1988), BV (Observatorio San Calixto (OSC Bolivia), 1913), BX (Department of Geological Survey of Botswana, 2001), C (Universidad de Chile, Dept de Geofisica (DGF UChile Chile), 1991), C1 (Universidad de Chile, 2012), CM (INGEOMINAS - Servicio Geologico Colombiano (SGC Colombia), 1993), CU (Albuquerque Seismological Laboratory (ASL)/USGS, 2006), CX (GFZ German Research Centre For Geosciences & Institut Des Sciences De L'Univers-Centre National De La Recherche CNRS-INSU, 2006), DK (GEUS Geological Survey of Denmark and Greenland, 1976), EC (Instituto Geofisico Escuela Politecnica Nacional (IG-EPN Ecuador), 2002), G (Institut de physique du globe de Paris (IPGP) & École et Observatoire des Sciences de la Terre de Strasbourg (EOST), 1982), GE (GEOFON Data Centre, 1993), GT (Albuquerque Seismological Laboratory (ASL)/USGS, 1993), II (Scripps Institution of Oceanography, 1986), IM (, 1965), IU (Albuquerque Seismological Laboratory (ASL)/USGS, 1988), NU (Instituto Nicaraguense de Estudios Territoriales (INETER), 1975), NZ (Institute of Geological and Nuclear Sciences Ltd (GNS New Zealand), 1988), OC (CONICET (OSCO), 2017), ON (Observatório Nacional, Rio de Janeiro, 2011), S1 (Australian National University (ANU, Australia), 2011), WA (Universidad Nacional de San Juan (UNSJ, Argentina), 1958), WI (Institut de physique du globe de Paris (IPGP), 2008) and YW (Glanville, 2021).

References

. (1965). *International Miscellaneous Stations (IMS).*

Abe, K. (1972). Focal Process of the South Sandwich Islands Earthquake of May 26, 1964. *Physics of the Earth and Planetary Interiors*, *5*, 110–122.

Abe, K. (1981). Magnitudes of large shallow earthquakes from 1904 to 1980. *Physics of the Earth and Planetary Interiors*, *27*(1), 72–92. doi: 10.1016/0031-9201(81)90088-1

Abe, K. (1982). Magnitude, Seismic Moment and Apparent Stress for Major Deep Earthquakes. *J. Phys. Earth*, *30*, 321–330.

Albuquerque Seismological Laboratory (ASL)/USGS. (1988). *Global Seismograph Network - IRIS/USGS.* International Federation of Digital Seismograph Networks. doi: 10.7914/SN/IU

Albuquerque Seismological Laboratory (ASL)/USGS. (1993). *Global Telemetered Seismograph Network (USAF/USGS).* International Federation of Digital Seismograph Networks. doi: 10.7914/SN/GT

Albuquerque Seismological Laboratory (ASL)/USGS. (2006). *Caribbean USGS Network.* International Federation of Digital Seismograph Networks. doi: 10.7914/SN/CU

Alfred Wegener Institute For Polar And Marine Research (AWI). (1993). *AW – AWI Network Antarctica.* Deutsches GeoForschungsZentrum GFZ. doi: 10.14470/NJ617293

Audet, P., Bostock, M., Christensen, N., & Peacock, S. (2009). Seismic evidence for overpressured subducted oceanic crust and megathrust fault sealing. *Nature*, *457*. doi: 10.1038/nature07650

Australian National University (ANU, Australia). (2011). *Australian Seismometers in Schools.* International Federation of Digital Seismograph Networks. doi: 10.7914/SN/S1

Becker, J. J., Sandwell, D. T., Smith, W. H. F., Braud, J., Binder, B., Depner, J., . . . Weatherall, P. (2009). Global bathymetry and elevation data at 30 arc seconds resolution: Srtm30_plus. *Marine Geodesy*, *32*, 355–371.

Beniest, A., & Schellart, W. P. (2020). A geological map of the Scotia Sea area constrained by bathymetry, geological data, geophysical data and seismic tomography models from the deep mantle. *Earth-Science Reviews*, *210*(April), 103391. Retrieved from https://doi.org/10.1016/j.earscirev.2020.103391 doi: 10.1016/j.earscirev.2020.103391

Bilek, S. L., & Lay, T. (2018). Subduction zone megathrust earthquakes. *Geosphere*, *14*(4), 1468–1500. doi: 10.1130/GES01608.1

Bilek, S. L., Lay, T., & Ruff, L. J. (2004). Radiated seismic energy and earthquake source duration variations from teleseismic source time functions for shallow subduction zone thrust earthquakes. *Journal of Geophysical Research: Solid Earth*, *109*(9), 1–14. doi: 10.1029/2004JB003039

Bird, P. (2003). An updated digital model of plate boundaries. *Geochemistry, Geophysics, Geosystems*, *4*(3). doi: 10.1029/2001GC000252

Bondár, I., Engdahl, E. R., Villaseñor, A., Harris, J., & Storchak, D. (2015). ISC-GEM: Global Instrumental Earthquake Catalogue (1900-2009), II. Location and seismicity patterns. *Physics of the Earth and Planetary Interiors*, *239*, 2–13. doi: 10.1016/j.pepi.2014.06.002

Brune, J. N. (1970). Tectonic Stress and the Spectra, of Seismic Shear Waves from Earthquakes. *Journal of Geophysical Research*, *75*(26), 4997–5009. Retrieved from http://doi.wiley.com/10.1029/JB075i026p04997 doi: 10.1029/JB075i026p04997

Carrillo Ponce, A., Dahm, T., Cesca, S., Tilmann, F., Babeyko, A., & Heimann, S. (2021). Bayesian multiple rupture plane inversion to assess rupture complexity: application to the 2018 Mw 7.9 Alaska earthquake. In *Egu general assembly 2021, online, 19–30 apr 2021.* doi: 10.5194/egusphere-egu21-1583

Cesca, S. (2020). Seiscloud, a tool for density-based seismicity clustering and visualization. *Journal of Seismology*, *24*, 443–457. doi: 10.1007/s10950-020-09921-8

Cesca, S., Sugan, M., Rudzinski, L., Vajedian, S., Niemz, P., Plank, S., … Dahm, T. (2022). Massive earthquake swarm driven by magmatic intrusion at the Bransfield Strait, Antarctica. *Commun. Earth Environ.*. doi: 10.1038/s43247-022-00418-5

CONICET (OSCO). (2017). *Observatorio Sismológico CIGEOBIO CONICET (OSCO).*

Retrieved from http://sismo.conicet.gov.ar

Dahm, T., Heimann, S., Metz, M., & Isken, M. P. (2021). A self-similar dynamic rupture model based on the simplified wave-rupture analogy. *Geophysical Journal International*, *225*, 1586–1604. doi: 10.1093/gji/ggab045

Department of Geological Survey of Botswana. (2001). *Botswana Seismological Network (BSN).*

Duan, B. (2012). Dynamic rupture of the 2011 mw 9.0 tohoku-oki earthquake: Roles of a possible subducting seamount. *Journal of Geophysical Research: Solid Earth*, *117*(B5). Retrieved from https://agupubs.onlinelibrary.wiley.com/doi/abs/10.1029/2011JB009124 doi: 10.1029/2011JB009124

Duputel, Z., Rivera, L., Kanamori, H., & Hayes, G. (2012). W phase source inversion for moderate to large earthquakes (1990-2010). *Geophysical Journal International*, *189*(2), 1125–1147. doi: 10.1111/j.1365-246X.2012.05419.x

Dziewoński, A. M., Chou, T.-A., & Woodhouse, J. H. (1981). Determination of earthquake source parameters from waveform data for studies of global and regional seismicity. *Journal of Geophysical Research*, *86*(B4), 2825–2852.

Ekström, G., Nettles, M., & Dziewoński, A. M. (2012). The global CMT project 2004-2010: Centroid-moment tensors for 13,017 earthquakes. *Physics of the Earth and Planetary Interiors*, *200-201*, 1–9. doi: 10.1016/j.pepi.2012.04.002

Flanders Marine Institute (VLIZ), Intergovernmental Oceanographic Commission (IOC). (2021). *Sea level station monitoring facility.* Retrieved 2022-01-04, from http://www.ioc-sealevelmonitoring.org doi: 10.14284/482

Forsyth, D. W. (1975). Fault Plane Solutions and Tectonics of the South Atlantic and Scotia Sea. *Journal of Geophysical Research*, *80*(11), 1429 – 1443. doi: 10.1029/JB080i011p01429;doi:10.

GEOFON Data Centre. (1993). *GEOFON Seismic Network.* Deutsches GeoForschungsZentrum GFZ. Retrieved from http://geofon.gfz-potsdam.de/doi/network/GE doi: 10.14470/TR560404

Geoscience Australia (GA). (1994). *Australian national seismograph network (ansn).*

GEUS Geological Survey of Denmark and Greenland. (1976). *Danish Seismological Network.*

GFZ German Research Centre For Geosciences, & Institut Des Sciences De L'Univers-Centre National De La Recherche CNRS-INSU. (2006). *IPOC Seismic Network.* Integrated Plate boundary Observatory Chile - IPOC. Retrieved from `http://geofon.gfz-potsdam.de/doi/network/CX` doi: 10.14470/PK615318

Giner-Robles, J. L., Pérez-López, R., Rodríguez-Pascua, M. A., Martínez-Díaz, J. J., & González-Casado, J. M. (2009). Present-day strain field on the South American slab underneath the Sandwich Plate (Southern Atlantic Ocean): A kinematic model. *Geological Society Special Publication*, *328*, 155–167. doi: 10.1144/SP328.6

Glanville, H. (2021). *Muswellbrook (Mus).* Geoscience Australia (GA). doi: 10.7914/SN/YW_2021

Glimsdal, S., Løvholt, F., Harbitz, C., Romano, F., Lorito, S., Orefice, S., ... Omira, R. (2019, 07). A new approximate method for quantifying tsunami maximum inundation height probability. *Pure and Applied Geophysics*. doi: 10.1007/s00024-019-02091-w

Goto, C., Ogawa, Y., Shuto, N., & Imamura, F. (1997). *Iugg/ioc time project, numerical method of tsunami simulation with the leap-frog scheme.* IOC Manuals and Guides v. 35, Paris.

Hayes, G. P., Moore, G. L., Portner, D. E., Hearne, M., Flamme, H., Furtney, M., & Smoczyk, G. M. (2018). Slab2, a comprehensive subduction zone geometry model. *Science*, *362*(6410), 58–61.

Heimann, S., Isken, M., Kühn, D., Sudhaus, H., Steinberg, A., Vasyura-Bathke, H., ... Dahm, T. (2018). *Grond - A probabilistic earthquake source inversion framework.* GFZ Data Services. doi: 10.5880/GFZ.2.1.2018.003

Heimann, S., Kriegerowski, M., Isken, M., Cesca, S., Daout, S., Grigoli, F., ... Dahm, T. (2017). *Pyrocko - An open-source seismology toolbox and library.* Potsdam: GFZ Data Sevices. Retrieved from `http://dataservices.gfz-potsdam.de/panmetaworks/`

showshort.php?id=escidoc:2144891 doi: 10.5880/GFZ.2.1.2017.001

Heimann, S., Vasyura-Bathke, H., Sudhaus, H., Paul Isken, M., Kriegerowski, M., Steinberg, A., & Dahm, T. (2019). A Python framework for efficient use of pre-computed Green's functions in seismological and other physical forward and inverse source problems. *Solid Earth*, *10*(6), 1921–1935. doi: 10.5194/se-10-1921-2019

Hubbard, J. (2021). *Mixed earthquake signals in the South Sandwich Islands.* doi: 10.32858/temblor.202

Ide, S., Baltay, A., & Beroza, G. C. (2011). Shallow Dynamic Overshoot and Energetic Deep Rupture in the 2011 Mw 9.0 Tohoku-Oki Earthquake. *Science*, *332*(6036), 1426-1429. doi: 10.1126/science.1207020

INGEOMINAS - Servicio Geologico Colombiano (SGC Colombia). (1993). *Red Sismologica Nacional de Colombia.* International Federation of Digital Seismograph Networks. Retrieved from https://www.fdsn.org/networks/detail/CM/ doi: 10.7914/SN/CM

Institut de physique du globe de Paris (IPGP). (2008). *GNSS, seismic broadband and strong motion permanent networks in West Indies.* Institut de physique du globe de Paris (IPGP), Université de Paris. Retrieved from http://volobsis.ipgp.fr/networks/detail/WI/ doi: 10.18715/ANTILLES.WI

Institut de physique du globe de Paris (IPGP), & École et Observatoire des Sciences de la Terre de Strasbourg (EOST). (1982). *GEOSCOPE, French Global Network of broad band seismic stations.* Institut de physique du globe de Paris (IPGP), Université de Paris. Retrieved from http://geoscope.ipgp.fr/networks/detail/G/ doi: 10.18715/GEOSCOPE.G

Institute of Geological and Nuclear Sciences Ltd (GNS New Zealand). (1988). *New Zealand National Seismograph Network.* Retrieved from http://info.geonet.org.nz/display/equip/New+Zealand+National+Seismograph+Network

Instituto Geofisico Escuela Politecnica Nacional (IG-EPN Ecuador). (2002). *Ecuador Seismic Network.*

Instituto Nicaraguense de Estudios Territoriales (INETER). (1975). *Nicaraguan Seismic Network.* International Federation of Digital Seismograph Networks. Retrieved from `https://www.fdsn.org/networks/detail/NU/` doi: 10.7914/SN/NU

Ishii, M., Shearer, P. M., Houston, H., & Vidale, J. E. (2007). Teleseismic P wave imaging of the 26 December 2004 Sumatra-Andaman and 28 March 2005 Sumatra earthquake ruptures using the Hi-net array. *Journal of Geophysical Research: Solid Earth*, *112*(B11).

Istituto Nazionale di Oceanografia e di Geofisica Sperimentale. (1992). *Antarctic Seismographic Argentinean Italian Network - OGS.* International Federation of Digital Seismograph Network. doi: 10.7914/SN/AI

Jia, Z., Zhan, Z., & Kanamori, H. (2022). The 2021 South Sandwich Island Mw 8.2 earthquake: a slow event sandwiched between regular ruptures. *Geophys. Res. Lett.*, *49*, 1–8. doi: 10.1029/2021GL097104

Kagan, Y. Y. (1991). 3-D rotation of double-couple earthquake sources. *Geophysical Journal International*, *106*(3), 709–716. doi: 10.1111/j.1365-246X.1991.tb06343.x

Kamigaichi, O. (2015). Tsunami forecasting and warning. In R. Meyers (Ed.), *Extreme environmental events.* Springer. doi: 10.1007/978-1-4419-7695-6

Kanamori, H., & Rivera, L. (2008). Source inversion of W phase: Speeding up seismic tsunami warning. *Geophysical Journal International*, *175*(1), 222–238. doi: 10.1111/j.1365-246X.2008.03887.x

Kato, A., Iidaka, T., Ikuta, R., Yoshida, Y., Katsuma, K., Iwasaki, T., … Hirata, N. (2010). Variations of fluid pressure within the subducting oceanic crust and slow earthquakes. *Geophys. R. Lett.*, *37*. doi: 10.1029/2010GL043723

Kennett, B., & Engdahl, E. (1991). Traveltimes for global earthquake location and phase identification. *Geophysical Journal International*, *105*(2), 429–465.

Kennett, B., Engdahl, E., & Buland, R. (1995). Constraints on seismic velocities in the Earth from traveltimes. *Geophysical Journal International*, *122*(1), 108–124. doi: 10.1111/j.1365-246X.1995.tb03540.x

Kiser, E., & Ishii, M. (2012, 03). Combining seismic arrays to image the high-frequency characteristics of large earthquakes. *Geophysical Journal International*, *188*(3), 1117-1128. Retrieved from `https://doi.org/10.1111/j.1365-246X.2011.05299.x` doi: 10.1111/j.1365-246X.2011.05299.x

Kodaira, S., Iidaka, T., Kato, A., Park, J.-O., Iwasaki, T., & Kaneda, Y. (2004). High pore fljuid pressure may cause silent slip in the Nankai Trough. *Science*, *304*. doi: 10.1126/science.1096535

Koper, K. D., Hutko, A. R., Lay, T., & Sufri, O. (2012). Imaging short-period seismic radiation from the 27 february 2010 chile (mw 8.8) earthquake by back-projection of p, pp, and pkikp waves. *Journal of Geophysical Research: Solid Earth*, *117*(B2). Retrieved from `https://agupubs.onlinelibrary.wiley.com/doi/abs/10.1029/2011JB008576` doi: 10.1029/2011JB008576

Larter, R. D., Vanneste, L. E., Morris, P., & Smythe, D. K. (2003). Structure and tectonic evolution of the South Sandwich arc. *Geological Society Special Publication*, *219*, 255–284.

Lay, T. (2018). A review of the rupture characteristics of the 2011 tohoku-oki mw 9.1 earthquake. *Tectonophysics*, *733*, 4-36. Retrieved from `https://www.sciencedirect.com/science/article/pii/S0040195117303992` (Physics of Earthquake Rupture Propagation) doi: 10.1016/j.tecto.2017.09.022

Lay, T., Kanamori, H., Ammon, C. J., Koper, K. D., Hutko, A. R., Ye, L., ... Rushing, T. M. (2012). Depth-varying rupture properties of subduction zone megathrust faults. *Journal of Geophysical Research: Solid Earth*, *117*(4), 1–21. doi: 10.1029/2011JB009133

Leat, P. T., Pearce, J. A., Barker, P. F., Millar, I. L., Barry, T. L., & Larter, R. D. (2004). Magma genesis and mantle flow at a subducting slab edge: The South Sandwich arc-basin system. *Earth and Planetary Science Letters*, *227*(1-2), 17–35. doi: 10.1016/j.epsl.2004.08.016

Lee, S.-J., Huang, B.-S., Ando, M., Chiu, H.-C., & Wang, J.-H. (2011). Evidence of large scale repeating slip during the 2011 tohoku-oki earthquake. *Geophysical Research*

Letters, *38*(19). Retrieved from https://agupubs.onlinelibrary.wiley.com/doi/abs/10.1029/2011GL049580 doi: 10.1029/2011GL049580

Madariaga, R. (1977, 12). High-frequency radiation from crack (stress drop) models of earthquake faulting. *Geophysical Journal International*, *51*(3), 625-651. Retrieved from https://doi.org/10.1111/j.1365-246X.1977.tb04211.x doi: 10.1111/j.1365-246X.1977.tb04211.x

Marty, S., Passelègue, F. X., Aubry, J., Bhat, H. S., Schubnel, A., & Madariaga, R. (2019). Origin of high-frequency radiation during laboratory earthquakes. *Geophysical Research Letters*, *46*(7), 3755–3763. doi: 10.1029/2018GL080519

Meng, L., Inbal, A., & Ampuero, J. P. (2011). A window into the complexity of the dynamic rupture of the 2011 mw 9 tohoku-oki earthquake. *Geophysical Research Letters*, *38*(7). doi: 10.1029/2011GL048118

Meng, L., Zhang, A., & Yagi, Y. (2016). Improving back projection imaging with a novel physics-based aftershock calibration approach: A case study of the 2015 Gorkha earthquake. *Geophysical Research Letters*, *43*(2), 628–636.

Metz, M. (2019). *A quasi-dynamic and self-consistent rupture model to simulate earthquake ruptures* (masterthesis, Universität Potsdam). doi: 10.25932/publishup-47310

Miller, P. K., Saffer, D. M., Abers, G. A., Shillington, D. J., Bécel, A., Li, J., & Bate, C. (2021). P- and s-wave velocities of exhumed metasediments from the alaskan subduction zone: Implications for the in situ conditions along the megathrust. *Geophysical Research Letters*, *48*(20), e2021GL094511. Retrieved from https://agupubs.onlinelibrary.wiley.com/doi/abs/10.1029/2021GL094511 (e2021GL094511 2021GL094511) doi: 10.1029/2021GL094511

Neidell, N. S., & Taner, M. T. (1971). Semblance and other coherency measures for multichannel data. *Geophysics*, *36*(3), 482–497.

NOAA National Geophysical Data Center. (2009). *ETOPO1 1 Arc-Minute Global Relief Model.* NOAA National Centers for Environmental Information. doi: 10.7289/V5C8276M

Observatório Nacional, Rio de Janeiro. (2011). *Rede Sismográfica do Sul e do Sudeste.* International Federation of Digital Seismograph Networks. doi: 10.7914/SN/ON

Observatorio San Calixto (OSC Bolivia). (1913). *Bolvian Seismic Network.* International Federation of Digital Seismograph Networks. doi: 10.7914/SN/BV

Okal, E. A., & Hartnady, C. J. (2009). The South Sandwich Islands earthquake of 27 June 1929: Seismological study and inference on tsunami risk for the South Atlantic. *South African Journal of Geology*, *112*(3-4), 359–370. doi: 10.2113/gssajg.112.3-4.359

Palo, M., Tilmann, F., Krueger, F., Ehlert, L., & Lange, D. (2014). High-frequency seismic radiation from Maule earthquake (Mw 8.8, 2010 February 27) inferred from high-resolution backprojection analysis. *Geophysical Journal International*, *199*(2), 1058–1077.

Passelegue, F., Almakari, M., Dublanchet, P., Barras, F., Fortin, J., & Violay, M. (2020). Initial effective stress controls the nature of earthquakes. *Nature Communications*, *11-5132*. doi: 10.1038/s41467-020-18937-0

Pelayo, A. M., & Wiens, D. A. (1989). Seismotectonics of the Scotia Sea. *Journal of Geophysical Research*, *94*(B6), 7293–7320.

Penn State University. (2004). *AfricaArray.* International Federation of Digital Seismograph Networks. doi: 10.7914/SN/AF

Purcaru, G., & Berckhemer, H. (1982). Quantitative relations of seismic source parameters and a classification of earthquakes. *Tectonophysics*, *84*(1), 57–128. doi: 10.1016/0040-1951(82)90154-8

Roger, J., Hebert, H., Jamelot, A., Gusman, A., Power, W., & Hubbard, J. (2022). The south sandwich circum-antarctic tsunami of august 12, 2021: widespread propagation using oceanic ridges. In *Egu general assembly 2022, vienna, austria, 23–27 may 2022.* doi: 10.5194/egusphere-egu22-904

Romano, F., Piatanesi, A., Lorito, S., Tolomei, C., Atzori, S., & Murphy, S. (2016). Optimal time alignment of tide-gauge tsunami waveforms in nonlinear inversions: application to the 2015 illapel (chile) earthquake. *Geophys. Res. Lett.*, *43*, 226–311. doi: 10.1002/

2016GL071310

Rössler, D., Krueger, F., Ohrnberger, M., & Ehlert, L. (2010). Rapid characterisation of large earthquakes by multiple seismic broadband arrays. *Natural Hazards and Earth System Sciences*, *10*(4), 923–932.

Scripps Institution of Oceanography. (1986). *Global Seismograph Network - IRIS/IDA.* International Federation of Digital Seismograph Networks. doi: 10.7914/SN/II

Simons, M., Minson, S. E., Sladen, A., Ortega, F., Jiang, J., Owen, S. E., … Webb, F. H. (2011). The 2011 magnitude 9.0 tohoku-oki earthquake: Mosaicking the megathrust from seconds to centuries. *Science*, *332*(6036), 1421-1425. Retrieved from `https://www.science.org/doi/abs/10.1126/science.1206731` doi: 10.1126/science.1206731

Song, T.-R. A., Helmberger, D., Brudzinski, M., Clayton, R., Davis, P., Perez-Campos, X., & Singh, S. (2009). Subducting slab ultra-slow velocity layer coinciding with silent earthquakes in Southern Mexico. *Science*, *324*. doi: 10.1126/science.1167595

Suzuki, W., Aoi, S., Sekiguchi, H., & Kunugi, T. (2011). Rupture process of the 2011 tohoku-oki mega-thrust earthquake (m9.0) inverted from strong-motion data. *Geophysical Research Letters*, *38*(7). Retrieved from `https://agupubs.onlinelibrary.wiley.com/doi/abs/10.1029/2011GL049136` doi: 10.1029/2011GL049136

Thomas, C., Livermore, R., & Pollitz, F. (2003). Motion of the Scotia sea plates. *Geophysical Journal International*, *155*(3), 789–804. doi: 10.1111/j.1365-246X.2003.02069.x

Tilmann, F., Zhang, Y., Moreno, M., Saul, J., Eckelmann, F., Palo, M., … Dahm, T. (2016). The 2015 Illapel earthquake, central Chile, a type case for a characteristic earthquake? *Geophys. Res. Lett.*, *43*, 1–26. doi: 10.1002/2015GL066963

Universidad de Chile. (2012). *Red Sismologica Nacional.* International Federation of Digital Seismograph Networks. Retrieved from `https://www.fdsn.org/networks/detail/C1/` doi: 10.7914/SN/C1

Universidad de Chile, Dept de Geofisica (DGF UChile Chile). (1991). *Chilean National Seismic Network.*

Universidad Nacional de San Juan (UNSJ, Argentina). (1958). *West Central Argentina Network.*

Universidade de Sao Paulo (USP). (1988). *Brazilian Lithospheric Seismic Project (BLSP).*

U.S. Geological Survey (USGS). (2020). *Earthquake lists, maps, and statistics.* Retrieved 2022-01-24, from https://www.usgs.gov/natural-hazards/earthquake-hazards/lists-maps-and-statistics

Vera, F., Tilmann, F., & Saul, J. (2021). A decade of short-period earthquake rupture histories from multi-array back-projection. *Earth and Space Science Open Archive*. doi: 10.1002/essoar.10508660.1

Wang, D., & Mori, J. (2011). Rupture process of the 2011 off the pacific coast of tohoku earthquake (mw 9.0) as imaged with back-projection of teleseismic p-waves. *Earth Planet Sp*, *63*(17). doi: 10.5047/eps.2011.05.029

Wang, R., Heimann, S., Zhang, Y., Wang, H., & Dahm, T. (2017, 06). Complete synthetic seismograms based on a spherical self-gravitating Earth model with an atmosphere–ocean–mantle–core structure. *Geophysical Journal International*, *210*(3), 1739-1764. Retrieved from https://doi.org/10.1093/gji/ggx259 doi: 10.1093/gji/ggx259

Wang, R., Lorenzo-Martin, F., & Roth, F. (2006). Psgrn/pscmp - a new code for calculating co- and post-seismic deformation, geoid and gravity changes based on the viscoelastic-gravitational dislocation theory. *Computers and Geosciences*, *32*, 527–541. doi: 10.1016/j.cageo.2005.08.006

Wessel, P., Smith, W. H., Scharroo, R., Luis, J., & Wobbe, F. (2013). Generic mapping tools: Improved version released. *Eos*, *94*(45), 409–410. doi: 10.1002/2013EO450001

Wilson, J. T. (1940). The love waves of the south atlantic earthquake of August 28, 1933. *Bulletin - Seismological Society of America*, *30*(3), 273–301.